Chemical Science

ROYAL SOCIETY OF CHEMISTRY

REVIEW

View Article Online
View Journal | View Issue

Cite this: *Chem. Sci.*, 2022, **13**, 6121

Active material and interphase structures governing performance in sodium and potassium ion batteries

Eun Jeong Kim, [a] P. Ramesh Kumar,[a] Zachary T. Gossage, [a] Kei Kubota, †[ab] Tomooki Hosaka, [ab] Ryoichi Tatara [ab] and Shinichi Komaba *[ab]

Received 14th February 2022
Accepted 24th April 2022

DOI: 10.1039/d2sc00946c

rsc.li/chemical-science

Development of energy storage systems is a topic of broad societal and economic relevance, and lithium ion batteries (LIBs) are currently the most advanced electrochemical energy storage systems. However, concerns on the scarcity of lithium sources and consequently the expected price increase have driven the development of alternative energy storage systems beyond LIBs. In the search for sustainable and cost-effective technologies, sodium ion batteries (SIBs) and potassium ion batteries (PIBs) have attracted considerable attention. Here, a comprehensive review of ongoing studies on electrode materials for SIBs and PIBs is provided in comparison to those for LIBs, which include layered oxides, polyanion compounds and Prussian blue analogues for positive electrode materials, and carbon-based and alloy materials for negative electrode materials. The importance of the crystal structure for electrode materials is discussed with an emphasis placed on intrinsic and dynamic structural properties and electrochemistry associated with alkali metal ions. The key challenges for electrode materials as well as the interface/interphase between the electrolyte and electrode materials, and the corresponding strategies are also examined. The discussion and insights presented in this review can serve as a guide regarding where future investigations of SIBs and PIBs will be directed.

1. Introduction

Burgeoning environmental issues stemming from societal dependence on fossil fuels necessitate a major shift toward new energy production, storage, and utilization technologies. While energy production from solar and wind appears promising and virtually unlimited compared with fossil fuels, its implementation requires significant improvements in energy storage for proper delivery. Electrochemical energy storage systems, such as rechargeable batteries and electric double layer capacitors, have received considerable attention as a potential solution to deal with the growing energy demand without increasing our carbon footprint. Among developed energy storage systems, lithium ion batteries (LIBs) have remained at the forefront since their first commercialization in 1991, and continue to expand their applications from portable consumer electronics toward transportation and powering the grid.[1] However, applying LIBs in these more demanding sectors has increased concerns on the scarcity of lithium sources.[2] In addition, other raw materials used in LIBs, *e.g.* Co, Ni, Cu, *etc.*, face environmental and ethical challenges including their concentration within limited regions of the world.[3] Such conditions are accelerating the discovery of novel alternatives for electrochemical energy storage, including sodium ion batteries (SIBs) and potassium ion batteries (PIBs), to compete with and/or compensate for the LIB market.[4–12]

SIBs and PIBs have seen rapid development in recent years, partially drawing from their likeness to LIBs where they can show similar energy storage mechanisms and are composed of analogous cell components.[4,6,7] For example, they can be constructed using insertion materials and carbon-based materials for the positive and negative electrodes, respectively, a standard porous separator made of glassy fiber or polymer, and a fluorophosphate, carbonate ester electrolyte (Fig. 1). However, utilizing Na^+ and K^+ as ionic carriers results in distinct coordination preferences in the electrode materials, different interactions with the electrolyte, and unique properties for their solid electrolyte (SEI) and cathode electrolyte interphases (CEI).[4,13] These differences result in limitations and benefits when preparing a battery based on Li^+, Na^+ or K^+, indicating they are not directly interchangeable. Instead, their unique physical properties, as summarized in Table 1, directly impact their performance.

Based on Faraday's law, the lower mass to charge ratio delivers the higher gravimetric capacity for a cell. In this respect, electrode materials containing Na^+ and K^+ would seem to show lower capacity than Li^+ counterparts. Actually, the delivered capacity is determined by the total mass of the

[a]*Department of Applied Chemistry, Tokyo University of Science, 1-3 Kagurazaka, Shinjuku, Tokyo 162-8601, Japan. E-mail: komaba@rs.tus.ac.jp*

[b]*Elements Strategy Initiative for Catalysts and Batteries (ESICB), Kyoto University, 1-30 Goryo-Ohara, Nishikyo-ku, Kyoto 615-8245, Japan*

† Present address: Battery Materials Analysis Group, Center for Green Research on Energy and Environmental Materials (GREEN), National Institute for Materials Science (NIMS), 1-1 Namiki, Tsukuba, Ibaraki 305-0044, Japan

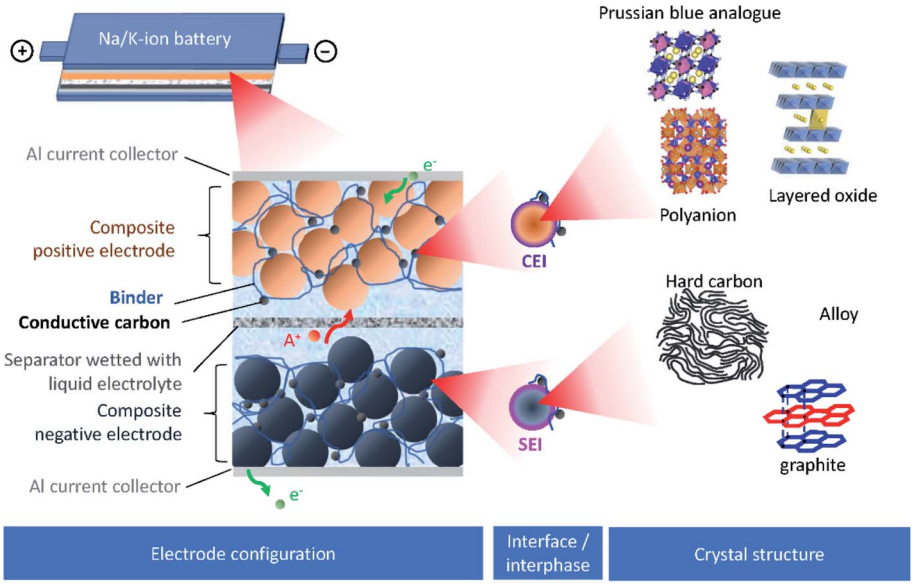

Fig. 1 Schematic presentation of SIBs or PIBs showing the electrode configuration, the interface/interphase between the electrode and electrolyte, and the crystal structure of electrode materials.

electrode material including the framework which generally governs a larger portion of the active material mass compared to the carrier ion. For example, the theoretical capacity of $KCoO_2$ is 206 mA h g^{-1}, equivalent to 75% of $LiCoO_2$ (274 mA h g^{-1}). This physical property becomes determinant only in the specific positive electrode cases, where the carrier ion makes up a large portion of the active material mass, but not the case of negative electrodes such as carbon and alloys.

Aside from adding mass, the framework further plays a key role in the stability of the electrode during operation. With reference to positive electrode materials, the amount of extractable alkali metal ions (A^+) is strongly correlated with the stability of the framework upon extraction of A^+, which often restrains upper cut-off voltage, delivering much less than the theoretical capacity. Structural integrity is also key to negative electrode materials such as common graphite and alloys, which rely on a crystalline structure to accommodate A^+ insertion. Large volume changes can result in loss of capacity and can disrupt key SEI structures. Maintaining the framework and interphase structures is an important task to provide batteries with reliable behavior and high cyclability.

Improving rate capabilities is another important target for the next generation of batteries. The smaller Stokes radii of K^+ and Na^+ compared with Li^+ (Fig. 2) result from their coordination with solvent/electrolyte species and their transfer at the SEI.[15] The large ionic radius of K^+ produces a relatively low surface charge density, namely classified as weak Lewis acid, resulting in weaker interactions between K^+ and solvent molecules. This has been demonstrated experimentally with K^+ in propylene carbonate (PC), showing the highest limiting molar ionic conductivity and implying the fastest diffusion rate.[15] Likewise, Na^+ represents a weaker Lewis acidity than Li^+, implying faster diffusion and a smaller activation energy of Na^+ transfer at the SEI formed in PC.[17] In addition, DFT calculations show that the desolvation energy of both Na^+ and K^+ is smaller than that of Li^+ in several aprotic solvents.[16] Kinetics of A^+ transfer at the interphase between the electrode and electrolyte is strongly linked to this desolvation energy as shown in

Table 1 Physical properties of Li^+, Na^+, and K^+ as charge carriers for rechargeable batteries

	Li^+	Na^+	K^+
Relative atomic mass	6.94	22.99	39.10
Mass to charge ratio	6.94	22.99	39.10
Shanon's ionic radius (Å) with six-fold coordination[14]	0.76	1.02	1.38
Stokes radius (Å) in PC[15]	4.8	4.6	3.6
Limiting molar ionic conductivity in PC (S cm^2 mol^{-1})[15]	8.3	9.1	15.2
Desolvation energy in PC (kJ mol^{-1})[16]	215.8	158.2	119.2
E° *vs.* SHE (V) in aqueous solution	−3.04	−2.71	−2.93
E° *vs.* Li/Li^+ (V) in PC	0	0.23	−0.09
Melting point of metal (°C)	180.5	97.8	63.4
Crust abundance (mass%)	0.0017	2.3	1.5

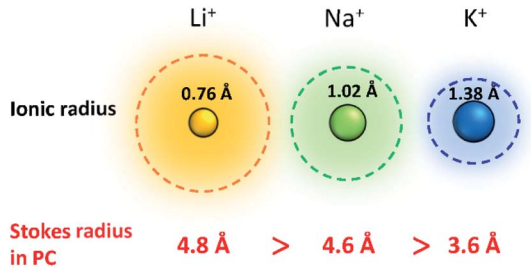

Fig. 2 Comparison of Shannon's radii and Stokes radii in PC for Li^+, Na^+ and K^+ ions. Adopted with permission from ref. 4. Copyright 2020 American Chemical Society.

LIBs.[18,19] Altogether, these results suggest promising rate performance capabilities for Na^+ and K^+ systems.

Operating voltage is a critical factor in determining the energy density of a battery, which is defined by the difference in potential between negative and positive electrodes. To achieve high energy densities, a high and low operating potential is desired for the positive and negative electrodes, respectively. When an alkali metal is used as the negative electrode, the standard electrode potential (E°) of alkali metal determines the lowest potential. In this respect, Li/Li^+ shows the lowest standard electrode potential, E°, in aqueous electrolytes. However, in PC, the E° of K/K^+ was calculated to be -0.09 V *vs.* Li/Li^+,[20] and thereafter, experimentally confirmed for multiple carbonate ester solvents by our group.[21,22] Taking this into consideration, PIBs possibly have a wide potential window which is advantageous to achieve higher energy density than LIBs under certain conditions. As seen in Fig. 3, the voltage window of a PIB widens compared to either LIBs or SIBs in PC-based electrolytes, assuming that the anodic limit of the electrolyte is consistent for all systems. It is worth noting that the operating voltage is also limited by electrolyte stability and passivation. Therefore, the formation of a reliable SEI and CEI becomes important to prevent continuous reduction and oxidation of the electrolyte by inhibiting direct electron transfer between the electrode and the electrolyte. In general, the SEI and CEI should prevent solvent breakdown and permeability

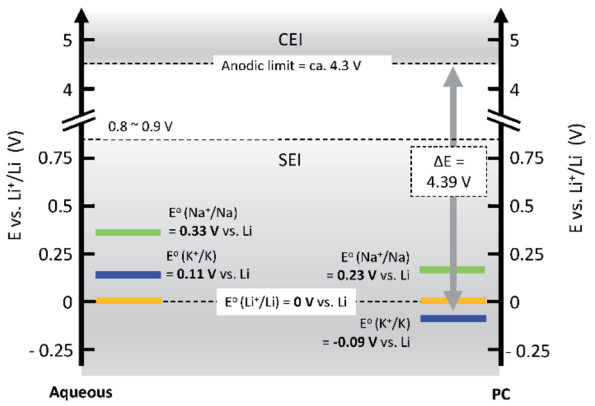

Fig. 3 Comparison of standard electrode potentials, E°, of alkali metals in aqueous (left), and PC (right) solutions.

while enabling fast ionic conductivity and mechanical stability.[13] Development of electrolytes with high oxidation and reduction resistance as well as understanding the interface between the electrode and electrolyte are indispensable to achieve high-voltage SIBs and PIBs.

Other important points in the development of high-performance SIBs and PIBs are safety and cost. Considering commercial graphite-based LIBs, the potential of graphite continuously increases upon deep discharge and reaches above 3 V (*vs.* Li/Li^+), eventually causing Cu oxidation and Cu plating onto the positive electrode.[23–25] The consequences of extreme discharge yield not only capacity fade but also severe thermal hazards. In contrast, SIBs and PIBs can use an Al current collector for the negative electrode since Al foil does not undergo alloying reactions with Na and K.[21] This bypasses such issues related to deep discharge in graphite-based LIBs and can reduce the weight and cost of the battery, permitting 0 V storage and/or transportation in the case of SIBs.[23–25] Aside from graphite, the interest for using large capacity alkali metals as negative electrode materials brings about other safety concerns. For one, these metals are highly reactive posing potential fire and explosion hazards. The metal plating reactions can lead to dendrite formation as often occurs at overcharged states, and this can lead to shorting and thermal runaway.[26–28] Furthermore, plated Na and K metals can react with the electrolyte relatively easily compared with Li metal, leading to redissolution into the electrolyte.[29,30] Significant research efforts have been exploring ways to minimize and prevent dendrite formation through electrolyte and interphase engineering.

The performance of SIBs and PIBs still needs to be enhanced for practical application beyond LIBs. Parameters including capacity, available voltage range, rate capability, cycle life, energy efficiency, and temperature range are important criteria to make SIBs and PIBs competitive. Here, we consider the strong correlations between these parameters and the impact of electrode material structure on the interaction with each A^+, the associated advantages as well as limitations, and the role of interphase structures between the electrode material and electrolyte. Of note, among the new chemistries such as Li–air, Li–S, Mg, and Ca batteries that have been considered as beyond LIB technologies, SIBs are the closest to reach the maturation stage, having given birth to companies such as Faradion in the UK, Novasis in the USA, Tiamat in France, and so on. Furthermore, systematic studies of three different A^+ ions and their electrochemistry are expected to provide synergistically deeper understanding and accelerate development of PIBs, taking advantage of low Lewis acidity and weak ionic interaction of K^+.

In this review, we will first focus on positive electrode materials for SIBs and PIBs, classified as layered oxides, polyanion materials, and Prussian blue analogues (PBAs). In the section of layered oxides, polymorphs of layered oxides and their evolution upon cycling will be explained, followed by the discussion on different electrochemical features including charge/discharge curves, capacity, working voltage, and cyclability as a function of A^+. Thereafter, we will examine binary transition metal systems which present peculiar properties including transition metal ordering and oxygen redox activity.

The benefits of binary and ternary transition metal systems for electrochemical performance derived from the reversible/stable crystal structure, fast kinetics, and stable interface will be described as well. In the following section on polyanion materials, we will discuss how the covalency of bonds between the redox active metal and ligand influences the operating potential of polyanion compounds. Important compounds are grouped based on their structure types, and their electrochemical properties are examined, highlighting the effects of different A^+. Furthermore, the influences of ligand type and symmetry for polyhedral groups are described in the sub sections. After that, material design of PBAs for SIBs and PIBs will be discussed based on their crystal and electronic structures, which are varied by transition metal species, crystal water, insertion ions, and crystal defects.

In the second half of this review, we will discuss carbon-based materials and alloy compounds as negative electrode materials, as well as the interphase that occurs at the negative electrode. In carbon-based materials, we will describe the different types of carbon electrodes and their impact on the energy storage mechanism with each of the A^+. The limitations of graphitic materials with Na^+ and K^+ ions, and methods for improving their energy storage capabilities through incorporation of more functional binders and concepts of co-solvent intercalation will be detailed. Thereafter, we will discuss efforts toward preparing hard and soft carbons for application in SIBs and PIBs. The impact of the precursor and preparation method will be described as well as the assumed mechanisms for different types of non-graphitic carbons. For alloy materials, we will briefly focus on their benefits and current challenges. Lastly, the importance of interphase studies will be reviewed, highlighting the different characteristics of interphases with each of A^+.

2. Layered oxides for positive electrode materials

Lithium layered oxides have been the most widely used class of positive electrode materials in LIBs since their commercialization in 1991 using $LiCoO_2$ as a positive electrode material. With the success of lithium layered oxides and the superior properties of layered oxides over other chemistries, *e.g.* their low formula weight, sodium and potassium analogues have been extensively investigated since the 1980s.[31]

2.1. Polymorphs of layered oxides

Classification proposed by Delmas *et al.* has been widely used to describe layered oxides with the A_xMO_2 (A = alkali metal and M = transition metal(s)) formula.[31] The layered oxides are built up of MO_2 slabs of edge-sharing MO_6 octahedra and A^+ ions occupying interlayer spaces. Depending on the various oxygen stacking sequences along the *c*-axis, they can be categorized into groups including O3, P3, P2 and O2, as illustrated in Fig. 4. The letter indicates the coordination environment of A^+ and the number corresponds to the number of transition metal layers in a hexagonal unit cell. When the hexagonal lattice is distorted, the prime symbol (′) is added between the alphabet and the number while the number of MO_2 is counted in a pseudohexagonal unit cell.

In the O3 type structure, A^+ ions occupy octahedral sites between MO_2 slabs with AB CA BC oxygen stacking and three MO_2 slabs are included in a hexagonal unit cell as seen in Fig. 4. Layered oxide materials commonly applied in commercialized LIBs such as $LiCoO_2$, $LiNi_{0.8}Co_{0.15}Al_{0.05}O_2$ and $LiNi_{1/3}Mn_{1/3}Co_{1/3}O_2$ adopt the O3 type with a space group of $R\bar{3}m$, also referred to as α-$NaFeO_2$ type. To the best of our knowledge, $LiMO_2$

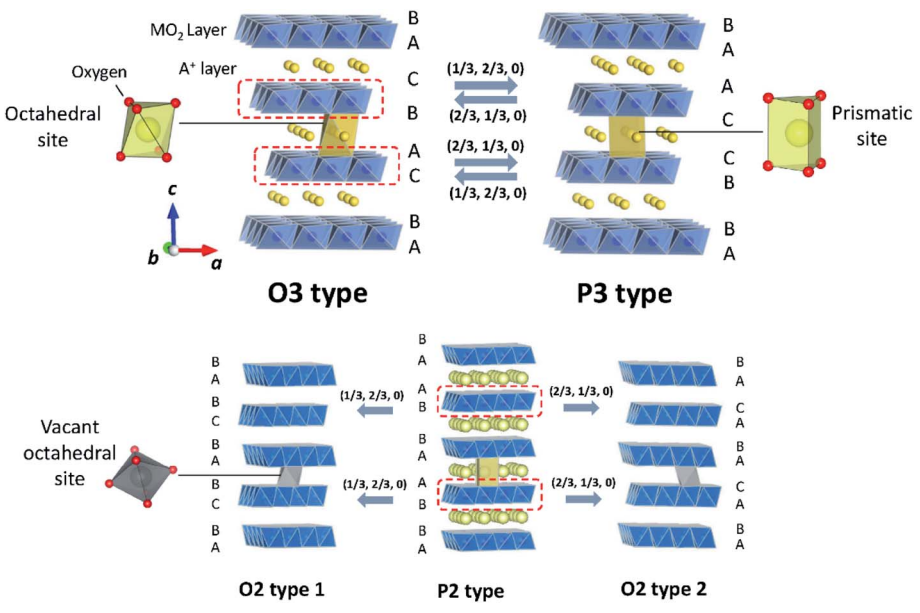

Fig. 4 Crystal diagrams of O3, P3, P2 and O2 type layered oxides. The MO_2 slabs are shown in blue. A^+ and vacancies in A^+ layers are shown in yellow and grey, respectively. Adopted with permission from ref. 8. Copyright 2014 American Chemical Society.

compounds, prepared by solid state synthesis, only crystallize in O3 type among the four groups described above because of the small ionic radius of Li^+. It is worth noting that there are other structure types such as γ-$LiFeO_2$ type, in which Li^+ and transition metal cations are ordered, and β-$NaMnO_2$ type known as a corrugated (zig-zag) layer type.[32–34] In the O3 type Li_xMO_2, cationic mixing is often observed due to the similar radius size between Li^+ and transition metal ion(s). In contrast, larger A^+ such as Na^+ and K^+ show a large variety of transition metals adopting the O3 type structure without cation mixing.[9] When Jahn–Teller active elements such as Mn^{3+} ($3d^4$ in high spin) or Ni^{3+} ($3d^7$ in low spin) consist of O3 type layered oxides, elongation or shortening of M–O bonds of MO_6 octahedra induces the cooperative Jahn–Teller effect. The macroscopic distortion of hexagonal symmetry results in the compounds adopting a monoclinic lattice with the *C*2/*m* space group in the O′3 type structure, which is observed for $NaMnO_2$ (ref. 35) and $NaNiO_2$.[36] Note that Na_xCoO_2 also crystallizes in the O′3 structure with a slightly deficient Na content.[37]

In the P3 type structure, the number of MO_2 slabs in a hexagonal unit cell with the *R*3*m* space group is three and A^+ ions occupy trigonal prismatic sites between MO_2 slabs with the AB BC CA array of oxygen packing along the *c*-axis. In contrast to $LiMO_2$, Na_xMO_2 and K_xMO_2 can crystallize in P3 or P′3 type structures in as-synthesized materials due to their larger ionic radii. In the case of Na_xMO_2, P3 type is preferred when $x < 0.5$. Removal of alkali metal ions from the O3 type structure in general induces a structural change to the P3 structure through gliding of MO_2 slabs without breaking of M–O bonds (Fig. 4). OP2 type is also reported as an intergrowth structure between O3 and P3 types upon charge/discharge. In an ideal OP2 structure, two types of A^+ layers, O type and P type layers, are alternately stacked along the *c*-axis.[38]

The P2 type structure is favored for alkali metal deficient compositions, and therefore found for Na_xMO_2 ($0.6 < x < 0.7$) and K_xMO_2 where A^+ ions occupy trigonal prismatic sites between MO_2 layers with AB BA oxygen array stacking along the *c*-axis. In the P2 type structure, there are two MO_2 slabs in a hexagonal unit cell with the space group of $P6_3/mmc$. The P2 phase transforms into the O2 phase upon extraction of A^+ by gliding MO_2 slabs. The gliding ideally occurs either (1/3, 2/3, 0) or (2/3, 1/3, 0) vector, leading to O2 type 1 or O2 type 2, respectively (Fig. 4).[39] The formation of intermediate structure OP4 proceeds upon charge as well. An ideal OP4 type has prismatic and octahedral A^+ layers, piled up alternately along the *c*-axis and two types of O2 layers are alternately stacked as octahedral A^+ layers.[38]

The different polymorphs influence electrochemical performance. In reference to capacity, O3 type compounds deliver higher initial charge capacity due to the high concentration of A^+ ions compared to A^+ deficient phases (P2 or P3). On the other hand, A^+ ions in prismatic sites enable the realization of larger reversible extraction of A^+ from the structure and faster diffusion compared to those in octahedral sites. The absence of tetrahedral sites in P2 or P3 type structures prevents migration of transition metal ions from MO_2 slabs to A^+ layers and permits direct A^+ migration to neighboring face-shared prismatic sites.

Table 2 summarizes structure types of A_xMO_2 (A = Li, Na or K, M = a single 3d transition metal and Rh, $x \leq 1$) obtained from direct synthesis methods, not including the ion-exchange step, with a single 3d transition metal and Rh. As mentioned above, the size of A^+ governs the structure of as-prepared materials, and therefore Li_xMO_2 with the smallest Li^+ crystallizes in the O3 structure which is a most thermodynamically stable phase. In contrast, K_xMO_2 and Na_xMO_2 can crystallize in P type structures. In particular, Na^+ with an intermediate radius size permits a large variety of phases, drawing scientific interest.

2.2. Different electrochemical features of A_xMO_2

2.2.1. Different electrochemical features of O-type and P-type A_xCoO_2. Since the average operating potential of positive electrode materials is one of the key factors in determining the energy density of batteries, it is of interest to compare the average voltage (identical to the potential of the positive electrode in a full cell) as a function of A^+ in A_xCoO_2. In this manuscript, the average voltage is determined by dividing the area of the charge or discharge curve by the delivered capacity.

Fig. 5a shows charge/discharge profiles of A_xCoO_2 adopting the O3 or P(′)3 structure. O3 type Na_xCoO_2 shows a significantly lower operating voltage compared to that of $LiCoO_2$. Given that both compounds are composed of Co with octahedral coordination and adopt the same O3 phase, the site energy of A^+ and the coordination and bond lengths of A–O and M–O seem to be comparable. The lower working voltage in Na_xCoO_2 can be attributed to the changes in the redox energy of $Co^{3+/4+}$.

Table 2 Structure types of A_xMO_2 layered oxides directly synthesized (A = Li, Na or K, M = a single 3d transition metal and Rh, $x \leq 1$)

Atomic number M (M = 3d metal and Rh)	$_{21}$Sc	$_{22}$Ti	$_{23}$V	$_{24}$Cr	$_{25}$Mn	$_{26}$Fe	$_{27}$Co	$_{28}$Ni	$_{29}$Cu	$_{45}$Rh
Li_xMO_2	—	—	O3	O3	—	—	O3	O3	—	O3
Na_xMO_2	O3	O3	O3	O3	O′3 P′3 P2/P′2	O3	O3/O′3 P′3 P2	O′3	O′3	O3
K_xMO_2	O3	—	—	O3/O′3 P3/P′3	P3/P′3 P′2	—	P3 P2/P′2	—	—	O3 P2

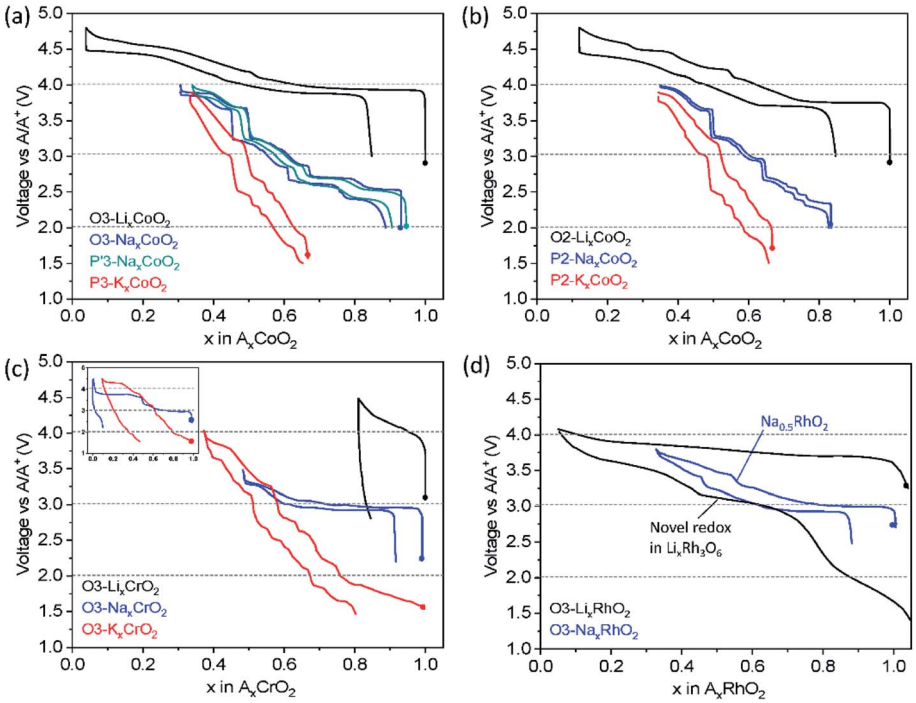

Fig. 5 Typical charge/discharge profiles of (a) O3 and P(′)3 type A_xCoO_2, (b) O2 and P(′)2 type A_xCoO_2, (c) O3 type A_xCrO_2 with an inset for those cycled in higher upper cut-off voltage, and (d) O3 type A_xRhO_2 in non-aqueous Li, Na, and K cells. Filled circle represents a starting point of charge.

According to a paper by Goodenough *et al.*, stronger covalent mixing of Co–O in the Na system raises Co–O antibonding orbital energy, and thus stronger Na^+–Na^+ repulsion increases the Co–O bond length, particularly at a higher Na^+ content, rendering lower voltage than the counterpart in the Li system.[40] In the same vein, P2 type Na_xCoO_2 and K_xCoO_2 display a lower voltage than O2 type $LiCoO_2$ (Fig. 5b) due to more covalent Co–O bonds, weaker Lewis acidity of Na^+ or K^+ and stronger Na^+–Na^+ or K^+–K^+ repulsion than those related to Li^+.

Another striking difference depending on the A^+ ion is the charge/discharge voltage profile upon galvanostatic cycling: $LiCoO_2$ exhibits smooth curves whereas the stepwise voltage profile is observed in Na_xCoO_2 and K_xCoO_2 regardless of the initial crystal structure type. The unique stepwise voltage curves are attributed to the A^+-vacancy ordering for the peculiar A^+ concentration such as 3/4, 5/8, 2/3, 4/7, 1/2, 1/3, *etc.*[41–44] The voltage jumps are related to the formation of a highly stable phase in a narrow A^+ concentration range surrounded by biphasic regimes that display voltage plateaus. During continuous changes in the concentration of A^+ in A_xCoO_2, an A_xCoO_2 single-phase is feasible, resulting in slopy voltage curves. Clear voltage jumps are evidenced at the well-known compositions of P2 type $Na_{1/2}CoO_2$ and $Na_{2/3}CoO_2$ (ref. 41) (Fig. 5b) and the phase transformation from O3 to O′3 for Na_xCoO_2 results in the voltage plateau at 2.5 V (Fig. 5a).[37]

When a certain amount of Na^+ ions are extracted, Na^+ in Na_xCoO_2 favors prismatic sites,[37,45] leading to similar voltage curve evolution as shown in O3 and P′3 type Na_xCoO_2 (Fig. 5a). The analogous voltage profiles in the range of $x \leq 2/3$ in P′3 and P2 type Na_xCoO_2 (Fig. 5a and b, respectively) upon extraction/insertion of Na^+ are probably due to fast and liquid-like Na^+ diffusion in P′3 and P2 types and weaker interaction between Na^+ and CoO_2 slabs having a wider interlayer distance than those of O3 type. The comparable voltage curves for P3 and P2 type K_xCoO_2 (Fig. 5a and b, respectively) can be explained in the same way.

2.2.2. Different electrochemical features of O3-type A_xCrO_2. Interestingly, $KCrO_2$ adopts an O3 structure because the electronic configuration of Cr^{3+} ($3d^3$), half filling t_{2g} orbitals, strongly prefers octahedral CrO_6 coordination, and the ionic radius of Cr^{3+} is large enough to compensate the penalty from K^+–K^+ repulsion.[46] It is of scientific interest to compare $ACrO_2$ since all the Li, Na, and K compounds adopt the O3 structure and the possibility of using the $Cr^{3+/6+}$ redox process is unique.

As shown in Fig. 5c, $LiCrO_2$ shows unsatisfactory electrochemical performance with notable irreversible capacity on the first cycle irrespective of particle size.[47,48] The main reason for the inferior discharge capacity is related to the irreversible structural change in the voltage range of 3.0–4.5 V (*vs.* Li/Li^+). During delithiation of $LiCrO_2$, oxidized Cr^{4+} ($3d^2$) tends to undergo the disproportionation reaction, forming Cr^{3+} ($3d^3$) and Cr^{6+} ($3d^0$). Besides, the interlayer distance in $LiCrO_2$ matches well with that in tetrahedral CrO_4^{2-}, which can be a driving force to migrate Cr^{4+} ($3d^2$) into the interstitial tetrahedral sites in Li layers in an irreversible disproportionation manner.[47] Using high angle annular dark field (HAADF) scanning transmission electron microscopy (STEM) and DFT calculation, the Cr migration from transition metal layers to Li

layers on the surface and the increased Li diffusion barrier are shown, which are responsible for the unsatisfactory electrochemical reactivity.[48]

In contrast to $LiCrO_2$, $NaCrO_2$ delivers a reasonable discharge capacity of *ca.* 110 mA h g^{-1}, corresponding to 0.43 Na^+ intercalation between 2.2 and 3.6 V (*vs.* Na/Na^+). In this voltage range, the compound undergoes O3–O′3–P′3 phase transformation with two biphasic regimes while 0.52 Na^+ is deintercalated. The structural evolution is reversible, leading to decent cycling performance.[49,50] When the upper cut-off voltage is extended to 4.5 V (*vs.* Na/Na^+), extremely small capacity is delivered on the first discharge. This is due to irreversible Cr migration induced by further phase transformation to O′3 beyond 3.6 V – in the O′3 phase vacant tetrahedral sites are formed by Na^+ extraction where oxidized Cr cations favorably migrate from their original transition metal layers, eventually the migrated Cr cations move to vacant octahedral sites and become pinned.[51] In addition, the significant voltage jump from 3.3 to 3.65 V (*vs.* Na/Na^+) shown at $x = 1/2$ in Na_xCrO_2 (Fig. 5c inset) originates from the Na^+-vacancy ordering, which is not observed in the counterpart of Li^+.[52]

In the case of $KCrO_2$, the stepwise voltage profile is more pronounced than the counterpart of Na^+ which represents a more complex phase transition. *In situ* XRD reveals the complex phase transition with the sequence of O3–O′3–P′3–P3–P′3–P3–O3 in the voltage range of 1.5–4.0 V (*vs.* K/K^+). This is probably attributed to the strong K^+–K^+ repulsion that requires several intermediate phases to minimize the K^+–K^+ repulsive interaction. The phase changes during charge are almost reversible except for the fact that the initial O3 phase is not recovered. Sluggish kinetics of K^+ is considered reason for the incomplete intercalation. As observed in $NaCrO_2$, once $KCrO_2$ is charged to 4.5 V, an additional plateau at around 4.3 V is found and significantly reduced discharge capacity is delivered (Fig. 5c inset) because the amorphous-like phase formed at the end of charge to 4.5 V lasts until the following discharge to 1.5 V.[46]

2.2.3. Different electrochemical features of O3-type A_xRhO_2. The effect of the transition metal on the operating voltage can be explained by the covalent character of the M–O bonds. A more covalent Rh–O bond than the Co–O bond causes a wider energy gap between bonding and antibonding orbitals. The raised anti-bonding orbitals are closer to the Fermi level and decrease the voltage, which is reflected in the case of $LiCoO_2$ (Fig. 5a) and $LiRhO_2$ (Fig. 5d), both adopting an O3 structure. In terms of a dynamic structure, it has been believed that the poor reversible capacity of O3 type $LiRhO_2$ between 1.0 and 4.5 V (*vs.* Li/Li^+) is related to Rh migration towards empty sites in Li layers, similar to O3 type $LiCrO_2$.[53] Later, it is revealed that when the Li content is smaller than 0.5, a novel phase is formed, identified as a rutile-ramsdellite intergrowth monoclinic $Li_xRh_3O_6$. This newly formed phase partially transforms back to the layered phase upon lithiation, providing stable capacity up to 15 cycles in the voltage range of 1.2–4.1 V (*vs.* Li/Li^+) and producing a novel plateau at 3.15 V (*vs.* Li/Li^+). Moreover, additional lithiation occurs as rutile-type and ramsdellite-type tunnels can accommodate Li^+, delivering slightly larger discharge capacity than the theoretical one (one electron per formula unit).[54]

In the case of O3 type $NaRhO_2$, the charge/discharge profiles are reversible in the voltage range of 2.5–3.8 V (*vs.* Na/Na^+) and a voltage jump is distinct when the Na^+ content is about 0.5 as shown in Fig. 5d. No phase transformation is observed until removal of a Na^+ content of 0.67 (charge to 3.8 V (*vs.* Na/Na^+)), different from $NaCoO_2$ in which gliding of CoO_2 results in P(′)3 type phases upon desodiation.[55] In addition, cation migration is expected to be prevented due to the increased covalency of Rh–O bonds using 5d electrons compared to that of 3d metal, Co–O.

From the above discussion by comparing charge/discharge profiles of A_xCoO_2, A_xCrO_2 and A_xRhO_2, we can understand that (i) larger A^+ tends to exhibit more notable stepwise load curves, (ii) dynamic structural evolution is more complex with larger A^+, (iii) the transformed phase at the end of charge dictates the reversibility of the structural transition, and (iv) using 4d or 5d transition metals might suppress MO_2 gliding upon extraction/insertion of A^+. From the practical points of view, layered oxides with a single metal, A_xMO_2, deliver generally limited capacity in Na and K cells. This drives spontaneously the research on layered oxides towards introducing multiple elements in transition metal layers.

2.3. Ordering in transition metal layers

Multiple elements in transition metal layers have been investigated as the electrochemical characteristics in the systems are significantly different from single transition metal systems, often resulting in enhanced performance. Thereby, we focus on binary and ternary systems in SIBs and PIBs here. In particular, transition metal ordering is often observed in binary systems ($A_x[M_yM'_{1-y}]O_2$ where square brackets represent transition metal layers). The differences in ionic radii as well as the valence between two cations composed of transition metal layers is believed to be a driving force to form the ordering. Honeycomb ordering is the most known in layered oxides where a cation (M) is surrounded by six cations (M′) and gives rise to the $\sqrt{3}a \times \sqrt{3}a$ superlattice. The ribbon superstructure is another ordering observed in the Li–Mn binary system where Li^+ ions separate ribbons composed of four Mn cations. The two different types of transition metal ordering are presented in Fig. 6a and b. In binary systems with adjacent transition metals, most of the compounds exhibit a disordered phase except for $Na_{2/3}[Ni_{1/3}Mn_{2/3}]O_2$ (ref. 56) in which Ni^{2+} is a center of the honeycomb superlattice. The honeycomb ordering between Ni and Mn seems to induce a stronger coupling between MO_2 layers, preventing the intercalation of water. In contrast, when Co is substituted for Ni, Mn^{3+} cations are formed and the superlattice of Ni(Co)–Mn ordering is suppressed, leading to a hydrophilic character.[56] Among layered oxides for PIBs, $K_{2/3}[Te_{1/3}Ni_{2/3}]O_2$ (ref. 57) is an interesting example having the honeycomb ordering. These transition metal ordered materials often have unique features such as moisture/air stability and oxygen redox activity.

2.3.1. Oxygen redox activity in $A_x[M_yM'_{1-y}]O_2$. To enhance the electrochemical activity of the AMO_2 electrode, reversible

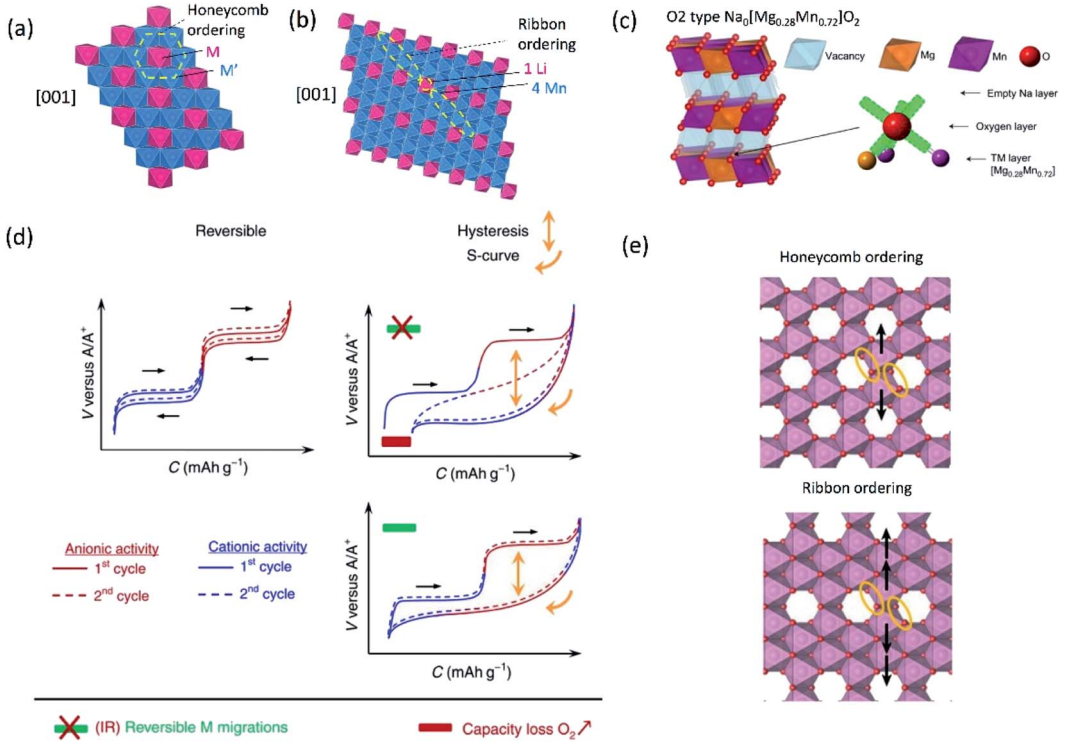

Fig. 6 Structural diagrams of (a) honeycomb and (b) ribbon ordering in the transition metal layers and (c) charged $Na_{0.67}[Mg_{0.28}Mn_{0.72}]O_2$ ($Na_0[Mg_{0.28}Mn_{0.72}]O_2$ adopting O2 type), highlighting a local oxygen environment coordinated octahedrally by two Mn and one Mg from the transition metal layer and three vacancies from the Na layer. Reprinted with permission from Springer Nature Customer Service Centre GmbH: Springer Nature, Nature Chemistry, ref. 60 copyright 2018. (d) Schematic charge/discharge curves of Li-rich and Na-rich layered oxides. Reprinted with permission from Springer Nature Customer Service Centre GmbH: Springer Nature, Nature, ref. 77 copyright 2019 (e) In-plane Mn migration (arrows) required to form O_2 molecules (orange ellipses) in the transition metal layers of charged honeycomb ordered $Na_{0.75}[Li_{0.25}Mn_{0.75}]O_2$ and ribbon ordered $Na_{0.6}[Li_{0.2}Mn_{0.8}]O_2$. Reprinted with permission from Springer Nature Customer Service Centre GmbH: Springer Nature, Nature, ref. 73 copyright 2019.

redox of $M^{n+/m+}$ and $O^{2-/(2-\delta)-}$ couples can be combined and has been investigated to date.[58] Table 3 summarizes the compounds not only having transition metal ordering but also exhibiting oxygen redox in the case of A = Na and K. Extensive theoretical studies together with experimental support have been carried out to explain the oxygen redox mechanism in layered oxides. Ceder and co-workers report that unhybridized O 2p orbitals, derived from the specific 180° Li–O–Li configurations in Li-rich layered oxides (one Li in transition metal layers and the other in Li layers), are responsible for the activation of the oxygen redox process.[59] This mechanism can explain the oxygen redox activity in sodium layered oxides containing Li^+ in transition metal layers. In the presence of specific Li–O–Na configurations, the energy level of orphaned O 2p orbitals is relatively higher than that of hybridized transition metal orbitals which trigger oxygen redox. In a similar vein, oxygen redox in the Mg–Mn binary systems can be attributed to the ionic Mg–O bonds that allow the O 2p orbitals to place at the top of the valence band upon extraction of Na^+.[60]

In the case of $Na[Na_{1/3}Ru_{2/3}]O_2$, the honeycomb ordered phase is essential to trigger oxygen redox because the short O–O bonds are created only in the ordered phase, which raises

Table 3 Binary systems of Na or K layered oxides exhibiting ordering in transition metal layers and oxygen redox

Composition $A_x[M_yM'_{1-y}]O_2$	Ionic radii M/M′ (Å) in six-fold coordination	Ordering type	Oxygen redox activity	Lattice oxygen loss	Voltage hysteresis
$Na[Li_{1/3}Mn_{2/3}]O_2$ (ref. 69)	0.76/0.53	Honeycomb	Active	O_2 evolution	Significant
$Na_{0.75}[Li_{0.25}Mn_{0.75}]O_2$ (ref. 73)	0.76/0.53	Honeycomb	Active	Suppressed	Significant
$Na_{0.6}[Li_{0.2}Mn_{0.8}]O_2$ (ref. 73 and 76)	0.76/0.53	Ribbon	Active	Suppressed	Suppressed
$Na_{2/3}[Mg_{0.28}Mn_{0.72}]O_2$ (ref. 60)	0.72/0.53	Honeycomb	Active	Suppressed	Significant
$Na[Na_{1/3}Ru_{2/3}]O_2$ (ref. 61)	1.02/0.62	Honeycomb	Active	Suppressed	Suppressed
$Na[Na_{1/3}Ir_{2/3}]O_2$ (ref. 62)	1.02/0.625	Honeycomb	Active	Suppressed	Suppressed
$Na_{2/3}[Ni_{1/3}Mn_{2/3}]O_2$ (ref. 63–66)	0.69/0.53	Honeycomb	Active/inactive	O_2 evolution/suppressed	Suppressed
$K_{2/3}[Te_{1/3}Ni_{2/3}]O_2$ (ref. 57)	0.69/0.97	Honeycomb	Active	—	Suppressed

unhybridized O 2p orbitals nearby the Fermi level. The honeycomb ordering is maintained between cationic vacancies and Ru cations after 1/3 Na^+ extraction from the transition metal layers of $[Na_{1/3}Ru_{2/3}]O_2$ slabs and leads to cooperative distortion, producing shorter O–O bonds.[61] Similarly, the shorter O–O bonds are formed in the honeycomb ordered $Na[Na_{1/3}Ir_{2/3}]O_2$ upon desodiation, featuring oxygen redox.[62] Moreover, the stronger overlapping between Ir 5d and O 2p orbitals allows oxygen redox to trigger in the earlier charge state than the 4d Ru case – oxygen redox is activated after removal of 0.5 Na^+ and 1 Na^+ in the Na–Ir and Na–Ru binary systems, respectively.

Oxygen participation in the charge compensation mechanism in P2-type $Na_{2/3}[Ni_{1/3}Mn_{2/3}]O_2$ was first proposed by Lee *et al.*[63] based on the electronic structure and density of state (DOS) calculation. However, whether oxygen redox is triggered or lattice oxygen loss dominates in the high voltage region is still under debate.[64–66]

Little investigation on oxygen redox has been performed in potassium layered oxides. Masesse *et al.* showed the participation of oxide anions in $K_{2/3}Te_{1/3}Ni_{2/3}O_2$ *via* strong hybridization between Ni 3d and O 2p orbitals.[57] Theoretical and experimental studies reveal that O 2p orbitals are in the vicinity of the Fermi level and reversible formation of ligand holes in O 2p bands during the first cycle.

Although oxygen redox represents a strategy to enhance the capacity of layered oxides *via* using cumulative cationic and anion redox processes, irreversible oxidation of the oxide anion, also referred to as lattice oxygen loss *via* O_2 evolution, and the voltage hysteresis between oxidation and reduction processes are major drawbacks for better application.

2.3.2. Oxygen redox competing with lattice oxygen loss. Bruce and co-workers proposed that at least three cations are necessary to mitigate the lattice oxygen loss by systematic studies of three compounds: $Li[Li_{0.2}Ni_{0.2}Mn_{0.6}]O_2$, $Na_{0.78}[Li_{0.25}Mn_{0.75}]O_2$ and $Na_{0.67}[Mg_{0.28}Mn_{0.72}]O_2$.[67] For the two Li^+ substituted compounds, Li^+ migrates from the transition metal layers to alkali metal layers, however only $Li[Li_{0.2}Ni_{0.2}Mn_{0.6}]O_2$ suffers from the lattice oxygen loss when almost equivalent charge is removed from their pristine state. This implies that the created transition metal vacancies through the migration of mobile Li^+ are not fully responsible for the lattice oxygen loss. Instead, the number of elements coordinated with oxygen anions upon charge is critical. For example, Mg^{2+} is retained in the transition metal layers even at deep charge for $Na_{0.67}[Mg_{0.28}Mn_{0.72}]O_2$ whereas the substituted Li^+ is extracted in $Na_{0.78}[Li_{0.25}Mn_{0.75}]O_2$. The remaining Mg^{2+} allows oxygen anions to remain coordinated by three cations, avoiding the lattice oxygen loss as illustrated in Fig. 6c. Using mapping of resonant inelastic X-ray scattering (mRIXS), it is shown that oxygen redox for $Na_{2/3}[Mg_{1/3}Mn_{2/3}]O_2$ is reversible and 87% of the initial capacity is sustained after 100 cycles.[68] An analogous result is reported for $Na[Li_{1/3}Mn_{2/3}]O_2$ where O_2 gas release commences when all Li^+ ions migrate to Na layers, meaning that oxygen anions bonded with only two Mn from the transition metal layers favor O_2 formation and are eventually released.[69]

In the case of Na-rich layered oxides with a 4d or 5d metal such as $Na[Na_{1/3}Ru_{2/3}]O_2$ and $Na[Na_{1/3}Ir_{2/3}]O_2$, ordering in the Na–Ru and Na–Ir slabs, respectively, becomes more pronounced upon desodiation, which is induced by the cooperative effect for maximizing the coulombic attraction between Na^+ and transition metal vacancies and minimizing the coulombic repulsion between Na^+ and Ru^{5+} or Ir^{5+}. This leads to the reversible phase transition O3–O1–O′1 upon cycling and provides a rigid structure to stabilize oxygen redox without lattice oxygen loss.[70]

2.3.3. Voltage hysteresis. The voltage hysteresis observed in most of the oxygen redox active materials is also correlated with the local oxygen coordination environment. Gent *et al.* proposed that transition metal migration is involved in stabilizing oxygen redox for Li-rich compounds and changes drastically the local oxygen coordination upon charge.[71,72] This lowers the oxygen redox potential relative to that of transition metal associated redox during discharge. As a consequence, the voltage hysteresis features charge/discharge profiles. Interestingly, the voltage hysteresis is suppressed for certain Na deficient compounds such as $Na_{0.6}[Li_{0.2}Mn_{0.8}]O_2$ (ref. 73–76) and Na-rich compounds composed of 4d or 5d metal.[61,62,70] Fig. 6d illustrates different scenarios driven by cationic and anionic processes in Li-rich and Na-rich layered oxides based on rigorous concepts of electronic structure theory.[77] Without cation migration and O_2 gas release, both cationic and anionic redox processes are fully reversible, resulting in a suppressed hysteresis between charge and discharge curves (top left). When lattice oxygen loss occurs due to cation migration in the first charge, a persistent hysteresis is expected in subsequent cycles (top right). The charge plateau in the high voltage region is recovered if no O_2 release takes place and cation migration is fully reversible (bottom right).

Recently, the importance of ordering in transition metal layers to alleviate the voltage hysteresis associated with cation migration has been reported by investigation of two compounds having a similar composition but adopting different transition metal ordering: honeycomb ordered $Na_{0.75}[Li_{0.25}Mn_{0.75}]O_2$ and ribbon ordered $Na_{0.6}[Li_{0.2}Mn_{0.8}]O_2$.[73] In the honeycomb superlattice, Mn migration, primarily in-plane, forms vacancies that accommodate O_2 molecules and the honeycomb ordering is lost upon charge. During discharge, the trapped O_2 molecules in the bulk are reduced and Li^+ returns to transition metal layers. However, the Li^+ ions occupy the sites where Mn is displaced rather than their original sites. The discharge voltage for this process is much lower, leading to voltage hysteresis. On the other hand, the in-plane Mn migration in the ribbon superstructure is less likely than in the honeycomb superlattice because multiple Mn displacements *via* already filled sites are necessary in the former as shown in Fig. 6e. Thereby, the ribbon type ordering provides narrow polarization of oxygen redox, which is also revealed in the Li-rich system.[78]

For the compounds based on 4d or 5d metals, large delocalization of 4d or 5d orbitals permits a larger overlap with O 2p orbitals than 3d metals. This leads to a strong covalent character of M–O bonds that suppresses transition metal migration to interlayers, as observed in $Na[Na_{1/3}Ru_{2/3}]O_2$,[61,70] $Na[Na_{1/3}Ir_{2/3}]$

O_2 (ref. 62) and $Li[Li_{1/3}Ir_{2/3}]O_2$.[79] Additionally, the well maintained honeycomb superstructure upon desodiation as mentioned above is attributed to the absence of voltage hysteresis.

Given the examples above, transition metal ordering plays an important role in not only activating oxygen redox but also stabilizing its electrochemical activity *via* suppressing lattice oxygen loss and/or voltage hysteresis. To exploit these advantages, the design of materials should be coupled with development of ultra-high-resolution XAS and RIXS to explain the complete mechanism of oxygen redox. Furthermore, a stable electrolyte at very high voltage should be considered for accurate understanding without interference from parasitic electrolyte reactions.

2.4. Binary and ternary systems for improved electrochemical performance

Designing binary and ternary system materials has been one of the strategies to enhance electrochemical performance in SIBs and PIBs as reversible and stable crystal structures both in bulk and in local and sufficient kinetics strongly depend on the composed elements. In parallel, surface modification to stabilize the interface between the electrolyte and electrode material and decreasing the primary particle size have been widely applied to achieve satisfactory performance. In the current section, P2 type $Na_{2/3}[Ni_{1/3}Mn_{2/3}]O_2$ is selected as a model compound for SIBs to examine the role of an additional substitution and its influence on electrochemical properties since this compound has been considered as a possible candidate for positive electrode materials due to not only its high operating voltage (around 3.8 V *vs.* Na/Na^+) and capacity (*ca.* 173 mA h g^{-1}) but also its air stability that is an intrinsic advantage for mass production.[39] As relatively fewer systematic studies have been carried out for layered oxides in PIBs, some examples exhibiting excellent performance are discussed, underlining the benefits of binary and ternary systems.

2.4.1. Reversible and stable crystal structure. Despite attractive features of P2 type $Na_{2/3}[Ni_{1/3}Mn_{2/3}]O_2$ described as above, long term cyclability of this compound is unsatisfactory, which is partially attributed to lattice stress induced by the phase transformation from P2 to O2 and the presence of Na^+-vacancy ordering, whose characteristics are well presented in the charge/discharge profile (Fig. 7a). Structural investigation using experimental and computational methods reveals that the P2–O2 phase transition is favored when $Na^+ < 1/3$, resulting in a long plateau at around 4.22 V (*vs.* Na/Na^+). Although this phase change is reversible,[39] the significant volume shrinkage by about 23% at the end of charge to 4.5 V (*vs.* Na/Na^+) causes significant capacity fade.[80] Limiting the upper cut-off voltage to 4.1 V, thus avoiding the phase transformation to P2, can be one way to enhance cyclability.[63] Another way is introducing electrochemically inactive elements including Li^+,[81] Mg^{2+},[82,83] or Ti^{4+} (ref. 84) in transition metal layers. The presence of the third element renders a smooth voltage profile as shown in P2 type $Na_{0.8}[Li_{0.12}Ni_{0.22}Mn_{0.66}]O_2$ and $Na_{0.67}[Mg_{0.1}Ni_{0.23}Mn_{0.67}]O_2$ (Fig. 7b), indicative of a solid-solution process and provides

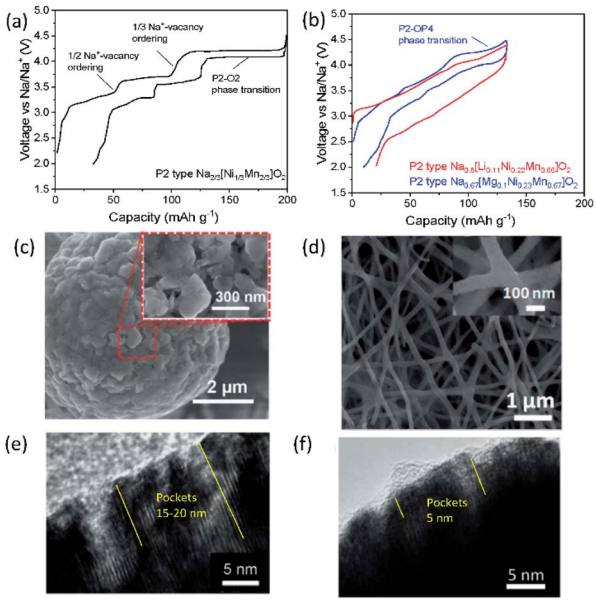

Fig. 7 Typical charge/discharge curves for (a) P2 type $Na_{2/3}[Ni_{1/3}Mn_{2/3}]O_2$ and (b) $Na_{0.8}[Li_{0.12}Ni_{0.22}Mn_{0.66}]O_2$ and $Na_{0.67}[Mg_{0.1}Ni_{0.23}Mn_{0.67}]O_2$ in red and blue, respectively. SEM images showing (c) secondary particles assembled by primary nanoparticles in P2 type $K_{0.65}[Fe_{0.5}Mn_{0.5}]O_2$. Reprinted with permission from ref. 88. Copyright 2018 John Wiley and Sons, and (d) interconnected P3 type $K_{0.7}[Fe_{0.5}Mn_{0.5}]O_2$ nanowires. Reprinted with permission from ref. 89. Copyright 2017 American Chemical Society. TEM images of (e) P2 type $Na_{2/3}[Ni_{1/3}Mn_{2/3}]O_2$ and (f) P2 type $Na_{2/3}[Al_{1/18}Ni_{11/36}Mn_{23/36}]O_2$ after 10 cycles in 2.0–4.5 V (*vs.* Na/Na^+). (e) and (f) are adopted with permission from ref. 90. Copyright 2018 John Wiley and Sons.

improved cycling performance. In the case of Li^+ doping, migration of Li^+ to Na layers at a deep charge state enables the adjacent MO_2 to be maintained, inhibiting the gliding to form the O2 phase.[81] Mg^{2+} substituted compounds also prohibit the P2–O2 phase transition, but the P2–OP4 phase transition, where the OP4 phase shows alternate stacking of octahedral and trigonal prismatic Na^+ layers along the *c*-axis, occurs in a reversible way.[82] Substitution of 1/6 Ti^{4+} for 1/6 Mn^{4+} in P2 type $Na_{2/3}[Ni_{1/3}Mn_{2/3}]O_2$ improves cycling performance through suppression of Na^+-vacancy ordering and reduced volume change upon charge to 4.5 V (23% and 12–13% for $Na_{2/3}[Ni_{1/3}Mn_{2/3}]O_2$ and $Na_{2/3}[Ti_{1/6}Ni_{1/3}Mn_{1/2}]O_2$, respectively), despite the presence of a plateau in the high voltage region.[84]

Using P2 type $Na_{2/3}[Ni_{1/3}Mn_{2/3}]O_2$ as a starting material, P2 type $K_{0.75}[Ni_{1/3}Mn_{2/3}]O_2$ is prepared using electrochemical ion-exchange by Myung and co-workers.[85] After 20 cycles, ion-exchange is completed where the honeycomb ordering is expected to be retained and a larger interlayer distance is found due to larger K^+. In contrast to $Na_{2/3}[Ni_{1/3}Mn_{2/3}]O_2$, there is no phase transformation to the O2 phase when $K_{0.75}[Ni_{1/3}Mn_{2/3}]O_2$ is charged to 4.3 V (*vs.* K/K^+) because the formation of O2 is predicted to occur below 1.5 V and beyond 4.3 V (*vs.* K/K^+) based on the computational studies. Therefore, a solid-solution reaction happens during cycling in the voltage range of 1.5–2.3 V with a voltage step due to the presence of ordering with a K^+ content of 1/2 in P2 type $K_{0.75}[Ni_{1/3}Mn_{2/3}]O_2$. This leads to

satisfactory cycling performance, retaining 86% of the initial capacity after 300 cycles at 20 mA g^{-1}.

2.4.2. Rate performance. In some cases, the substituted element contributes improvement in rate performance. For instance, Mg^{2+} (ref. 83) or Ti^{4+} (ref. 86) doping in P2 type $Na_{2/3}[Ni_{1/3}Mn_{2/3}]O_2$ provides enhanced rate performance by disruption of Na^+-vacancy ordering because high Na^+ diffusivity and low activation energy barriers are realized in Na layers. The interruption of K^+-vacancy ordering upon cycling also leads to good rate performance as observed in P3 type $K_{0.54}[Co_{0.5}Mn_{0.5}]O_2$, delivering a discharge capacity of 78 mA h g^{-1} even at 500 mA g^{-1}. In this compound, the low activation barrier of K^+ is calculated to be around 260 meV which is comparable to that for Li^+ diffusion. Besides, overlapping of O 2p orbitals with Co is anticipated to facilitate electron transfer.[87] Downsizing particles offers good rate capability as observed in P2 type $K_{0.65}[Fe_{0.5}Mn_{0.5}]O_2$ (ref. 88) and P3 type $K_{0.7}[Fe_{0.5}Mn_{0.5}]O_2$.[89] The former exhibits a hierarchical morphology consisting of a primary particle size of around 100 nm (Fig. 7c) and the latter displays a nanowire structure (Fig. 7d). They show superior capacity (151 and 178 mA h g^{-1} at 20 mA g^{-1} for P2 type $K_{0.65}[Fe_{0.5}Mn_{0.5}]O_2$ and P3 type $K_{0.7}[Fe_{0.5}Mn_{0.5}]O_2$, respectively) and rate capability (103 and 114 mA h g^{-1} at 100 mA g^{-1} for P2 type $K_{0.65}[Fe_{0.5}Mn_{0.5}]O_2$ and P3 type $K_{0.7}[Fe_{0.5}Mn_{0.5}]O_2$, respectively), which are attributed to the specific particle size and morphology whereas micrometer-sized counter compounds exhibit unsatisfactory capacity and rate performance. In addition, the carbon framework interconnected with P3 type $K_{0.7}[Fe_{0.5}Mn_{0.5}]O_2$ nanowires can offer 3D continuous electron transport pathways, leading to the excellent performance.

2.4.3. Stable interface. As electrolyte decomposition and dissolution of transition metals occur in the high voltage region, a stable interface between the electrode material and the electrolyte is in demand to realize satisfactory electrochemical performance similar to LIBs. The substituted element can affect surface degradation as the electronic state and catalytic properties of the electrode material surface can be altered by the dopant. For example, 1/18 Al substitution for P2 type $Na_{2/3}[Ni_{1/3}Mn_{2/3}]O_2$ shows a clear difference in the particle surface after 10 cycles. The Al substituted compound (P2 type $Na_{2/3}[Al_{1/18}Ni_{11/36}Mn_{23/36}]O_2$) demonstrates shallower pockets with 5 nm depth from the surface (Fig. 7f) while the non-doped compound has pockets with 15–20 nm depth from the surface (Fig. 7e).[90] These pockets (or micro-cracks) are proposed to be caused by the dissolution of transition metals in the electrolyte at high voltage due to the attack of HF produced by the decomposition of the electrolyte.[91] The Al substitution probably forms a more insoluble surface and suppresses the transition metal dissolution. Alvarado *et al.*[92] reported that Al_2O_3 coating *via* Atomic layer deposition (ALD) on the P2 type $Na_{2/3}[Ni_{1/3}Mn_{2/3}]O_2$ composite electrode affects the interface. X-ray photoelectron spectroscopy (XPS) results reveal that the CEI on the ALD-coated electrode contains fewer organic species, *e.g.* carbonates, esters, and alkoxyl functionalities, and more inorganic species such as NaF, which enables fast Na^+ kinetics and increases coulombic efficiency. Besides, the large CO component formed, associated with polymeric species such as poly(ethylene oxide) from the PC electrolyte decomposition, in the ALD-coated electrode plays an important role in forming a more flexible CEI, preventing active material particle exfoliation. The research on the CEI for PIBs is still at an early stage and optimization of the electrolyte is undergoing. Nevertheless, homogeneous surface coating and decent selection of substitution for potassium layered oxides would mitigate detrimental surface reactions and concomitant structural degradation.

3. Polyanion compounds

While layered oxides have significant precedence in research and as commercial materials, they suffer from stacking modification with slab gliding or irreversible structural transformation when the number of extracted A^+ is high. In contrast, polyanionic materials provide long-term structural stability and high thermal stability, which are their major advantages despite weight penalty. Polyanionic compounds possess an open framework structure consisting of MO_x (M = transition metals) and $(XO_x)_n$ (X = P, S, As, Si, Mo, or W) polyanionic groups. This 3D structure offers not only structural and thermal stabilities but also a large interstitial space to accommodate larger A^+ during insertion reactions. In addition, the nature of the polyanionic groups permits tuning $M^{n+/(n+1)+}$ redox potentials, which represents a way to enhance the working voltage for positive electrode materials. There are so many types of polyanionic compounds due to the diversity of their composition and structure, and it is possible to fine-tune their electrochemical properties such as capacity, rate capability, and operating potential.

In layered oxides, the selection of transition metals predominantly affects the working potential of the electrode and the cell voltage. In the same vein, the type of transition metal is essential to achieve high electrode-potential in polyanionic compounds. In addition to that, polyanionic compounds crystalize into many more structural types. Thereby, polyanionic compounds provide many more numerous ways to adjust the $M^{n+/(n+1)+}$ redox potential, which is highly correlated mainly with the transition metals and structural types. Depending on the structural type, the ionicity/covalency of the M–O bonds in the MO_x polyhedron is varied. The three most important structural factors are (i) the type of ligand, (ii) the presence and number of oxygen atoms that are simultaneously shared by all MO_x, XO_x, and AO_x polyhedra, called as commonly shared oxygen hereafter, and (iii) the sharing mode between adjacent MO_x–MO_x and the position of the ligand introduced into MO_x.

As shown in Fig. 8a, the ligands include not only XO_x oxyanionic groups but also $-F^-$ or $-OH^-$ that are more electronegative than $-O^{2-}$. When XO_x is coordinated to M, the higher electronegativity of the oxyanionic groups increases the ionic character of M–O bonds, significantly raising the $M^{n+/(n+1)+}$ redox potential as a primary inductive effect.[93] The order of their electronegativity is $(SiO_4)^{4-} < (BO_3)^{3-} < (PO_4)^{3-} < (P_2O_7)^{4-} < (C_2O_4)^{2-} < (SO_4)^{2-}$, determined by the electronegativity of Si, B, P, C, and S which is 1.9, 2.04, 2.19, 2.55, and 2.58, respectively. Therefore, $(SO_4)^{2-}$ containing polyanionic compounds exhibit

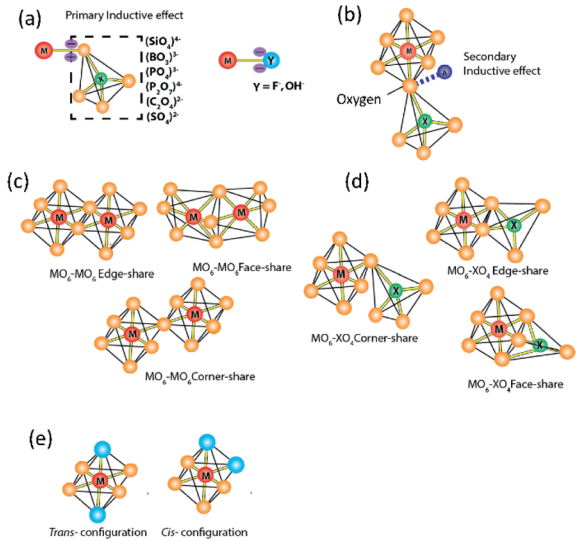

Fig. 8 Schematic illustration of (a) M-ligand bonds with various types of ligands including oxyanionic groups (dashed box) and highly electronegative anions (blue Y = F^- and OH^-), (b) oxygen shared by polyhedra of MO_x, XO_x, and AO_x at the same time, called as commonly shared oxygen, (c) sharing types between two adjacent MO_x polyhedra, (d) sharing types between MO_x and XO_x polyhedra, and (e) configuration types of substituted Y in MO_x. Orange represents the O atom.

a higher redox potential as long as other parameters, *e.g.* the valency of the redox center and the sharing mechanism, are comparable. Replacing oxygen with a highly electronegative anion, referred to as Y from now on, such as F^- (3.98) and OH^- (3.44) in the MO_x polyhedron is also shown to raise the ionic character of M–O bonds and the $M^{n+/(n+1)+}$ redox potential.

The second major factor is the presence and the number of commonly shared oxygen (Fig. 8b), which raises the $M^{n+/(n+1)+}$ redox potential as the secondary inductive effect.[94] When an A^+ ion is coordinated to the oxygen commonly shared by both the MO_x and XO_x polyhedra, the ionic character of M–O bonds further increases. This extra effect beyond the primary inductive effect is called the secondary inductive effect. The higher number of the commonly shared oxygen increases the ionicity of M–O bonds.[95] Of note, the number of commonly shared oxygen is normalized by the number of transition metals to avoid the effect of unit cell size throughout the section. Similarly, the electropositivity (low electronegativity close to zero) of A^+ would affect the secondary inductive effect.

The third major factor of the positional effects is categorized into three: sharing types between two adjacent MO_x polyhedra (Fig. 8c), sharing types between MO_x and XO_x polyhedra (Fig. 8d), and configuration types of substituted Y (Fig. 8e). First, the sharing types between MO_x affect the distance between two neighboring M: M-to-M distance. In the edge- or face-sharing, the M-to-M distance is shorter than in the corner-sharing, which promotes symmetry change through the shifting of the M position systematically from its original position to reduce electrostatic repulsion between M^{n+} and M^{n+}. The changes in the symmetry, namely distortion of MO_x, lower the energy of antibonding molecular orbitals, leading to a higher $M^{n+/(n+1)+}$ redox potential.[94] The effect of sharing type between MO_x and XO_x on the redox potential is also significant. When the MO_6 shares the edge, face, or corner with the XO_4, cationic repulsion between M and X increases the ionic character of M–O bonds in MO_6, resulting in increased redox potentials. This effect is also more pronounced in edge- or face-sharing than corner-sharing. When two O atoms in MO_x are substituted by a more electronegative element Y such as F and OH, two configurations exist based on the position of the substituted element. In the *cis*-configuration the substituted elements exist at an angle of Y–M–Y about 90° in the polyhedron, whereas in the *trans*-configuration, the Y–M–Y angle is approximately 180° (Fig. 8e). The *cis*-configuration tends to alter the symmetry of the polyhedron more significantly than the *trans*-configuration. For example, the MO_4F_2 octahedron with *cis*-configurated F has asymmetrical charge distribution compared to the MO_4F_2 octahedron with *trans*-configurated F. This asymmetrical charge distribution and the strong interaction between F–F in the *cis*-configuration leads to high distortion in the MO_4F_2 octahedron.[96] As a result, the *cis*-configurated octahedron delivers a higher $M^{n+/(n+1)+}$ redox potential compared to the *trans*-configurated octahedron. Sometimes, the *cis*-configurated substituted elements are part of the edge- or face-sharing between two adjacent polyhedra. In this case, the effect of repulsion between two metals (M–M or M–X) on the redox potential is minor.[94]

In the following sections, we will review important polyanionic compounds classified by structure types, focusing on how the nature of transition metal affects electrochemical performance as well as how the ionicity/covalency of the M–O bonds in the MO_x polyhedron influences the $M^{n+/(n+1)+}$ redox potential by presenting important examples.

3.1. Olivine related and amorphous types

To date, the most successful polyanionic material is triphylite $LiFePO_4$ with its successful application in LIBs. $LiFePO_4$ has an olivine-like structure based on a distorted oxygen hexagonal closed packing. However, unlike olivine Mg_2SiO_4 where Mg occupies both 4a and 4c octahedral sites (Fig. 9b), Li^+ and Fe^{2+} ions separately occupy the 4a and 4c sites, respectively (Fig. 9a). $LiFePO_4$ has a one-dimensional Li^+ diffusion path along the *b*-axis.[97] Despite its attractive properties such as high redox potential and excellent cycling stability, $LiFePO_4$ shows key drawbacks, including low intrinsic electronic conductivity and anti-site defect formation that significantly impede Li^+ diffusion.[98,99] Various synthetic approaches have been employed to overcome the low electronic conductivity nature,[100] *e.g.* making composites using carbonaceous materials (carbon, graphite, carbon nanotube, *etc.*), metal particle dispersion on the surface, and doping of supervalent cations (Zn^{4+}, Nb^{5+}, Ti^{4+}, Mg^{2+}, Al^{3+}). To enhance the Li^+ diffusion, nanosizing is one of the strategies. As per previous reports, when the same concentration of Li/Fe anti-site defects is present, the nano-size $LiFePO_4$ shows less trapped Li^+ compared to the micron-size one, reducing the possibility of Li^+ diffusion tunnel blocking.[101] The nano-sized

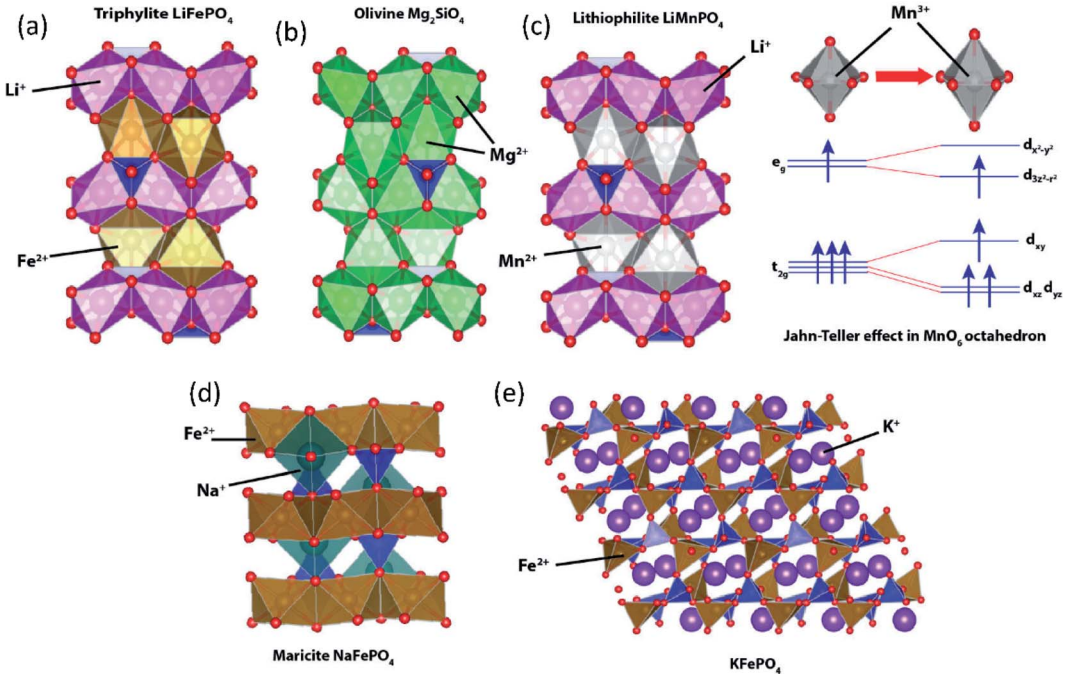

Fig. 9 Structural illustration of (a) triphylite $LiFePO_4$, (b) olivine Mg_2SiO_4, (c) lithiophilite $LiMnPO_4$ with an inset showing Jahn–Teller distortion in MnO_6, (d) maricite $NaFePO_4$, and (e) $KFePO_4$.

$LiFePO_4$ may enhance its properties, but low electrode tap density significantly reduces the volumetric energy density. Lithiophilite $LiMnPO_4$ also has a triphylite-type structure having distinctive Li^+ and Mn^{2+} sites (Fig. 9c). The redox potential driven by $Mn^{2+/3+}$ (4.1 V *vs.* Li/Li^+) is higher than that of $Fe^{2+/3+}$ (3.43 V *vs.* Li/Li^+), but $LiMnPO_4$ is a highly insulating material with a bandgap of 2 eV, and has structural instability in a fully charged state. During the charge, oxidation of Mn^{2+} generates Mn^{3+} (high spin) which is Jahn–Teller active in the MnO_6 octahedra. Asymmetrical distribution of electron density leads to elongation of bonds between Mn^{3+} and ligands in the *z*-direction, called Jahn–Teller distortion. Due to the cooperative distortion of the MnO_6 octahedron in Mn(III)PO_4, the one-dimensional Li^+ diffusion path shrinks, which is unfavorable for the subsequent lithiation process.[102,103] Although triphylite-type $LiCoPO_4$ and $LiNiPO_4$ provide higher redox potentials, the lack of a stable electrolyte in the high voltage region hinders their practical application. In addition, Ni^{3+} has a high spin configuration in the NiO_6 octahedron that has a strong Jahn–Teller distortion, hindering the one-dimensional Li^+ diffusion path.

Since the successful application of $LiFePO_4$, its counterparts have been extensively investigated in SIBs. Similar to triphylite $LiFePO_4$, maricite $NaFePO_4$ also has an olivine-like structure. However, Na^+ and Fe^{2+} ions occupy 4c and 4a octahedral sites, respectively (Fig. 9d), and the positions of the A^+ and Fe^{2+} are opposite to those of the triphylite. In the maricite-type structure, parallel FeO_6 chains are formed by FeO_6 octahedral edge-sharing, and the PO_4 tetrahedron connects three parallel FeO_6 chains, which restrict the migration of Na^+.[104] Interestingly, it has been demonstrated that maricite $NaFePO_4$ is transformed to amorphous $FePO_4$ upon the first charge, which allows Na^+ to hop between adjacent sites with lower activation energy along the *b*-axis.[105] Triphylite-type $NaFePO_4$ can be obtained by electrochemical or chemical ion exchange from triphylite $LiFePO_4$ and this material delivers a discharge capacity of 154 mA h g^{-1},[106] comparable to that of the amorphous compound.

In the case of $KFePO_4$, synthesized by a solid-state reaction, it contains units of FeO_4 tetrahedral groups linked by corner-sharing with another FeO_4 and PO_4 tetrahedral groups (Fig. 9e), different from the olivine-related types (triphylite and maricite types).[107] $KFePO_4$ (space group of $P2_1/n$) delivers very low capacity (20 mA h g^{-1}) with a slopy voltage profile, indicating an unfavorable crystal structure for K^+ extraction/insertion reactions. Recently, it has been reported that amorphous $FePO_4$ and amorphous $KFePO_4$ deliver 160 mA h g^{-1} and 90 mA h g^{-1}, respectively, in PIBs.[108] Once K^+ inserted into the amorphous $FePO_4$, it becomes a crystalline monoclinic $KFe_2(PO_4)_2$ phase delivering a high reversible capacity.[109] In 2018, our group demonstrated the K^+ storage ability of the delithiated triphylite $FePO_4$/C composite. The $FePO_4$/C composite shows a very stable capacity of 120 mA h g^{-1} with a mid-point discharge voltage (corresponding to the voltage at SOC = 50%, Table 4) of 2.3 V (*vs.* K/K^+).[110] But, it shows very slopy charge/discharge curves, indicating that insertion of larger K^+ into $FePO_4$ lowers its crystallinity, accompanied by irreversible transformation into the phase with insufficient ionic diffusivity.

3.2. NASICON type

$Na_{1+x}Zr_2Si_xP_{3-x}O_{12}$ is a promising sodium super ion conductor, so-called NASICON.[111] The general formula of NASICON type compounds is $A_xM_2(XO_4)_3$, where A is the alkali metal, alkaline

Table 4 Summary of selective polyanion-type electrode materials for Na and K ion batteries[a]

Structure type	Material	Space group	Redox couple	Sharing mechanism between two neighbouring TM polyhedra	No. of commonly shared oxygen atoms	SIB/PIB	Mid-point discharge voltage	Theoretical (*)/initial experimental capacity (mA h g^{-1})	Ref.
Olivine and amorphous	$NaFePO_4$	*Pnma*	$Fe^{2+/3+}$	Oc-ed-Oc	4	SIB	2.8	154 (1Na)/150	106
	Amorphous-$FePO_4$	—	$Fe^{2+/3+}$	—	—	SIB	2.4	177 (1Na)/154	109
	Amorphous-$FePO_4$	—	$Fe^{2+/3+}$	—	—	PIB	2.5	177 (1K)/156	109
	Hematiite-$FePO_4$	*Pnma*	$Fe^{2+/3+}$	Oc-ed-Oc	—	PIB	2.3	177 (1K)/120	110
	Amorphous-$KFePO_4$	—	$Fe^{2+/3+}$	—	—	PIB	2.5	141 (1K)/90	108
NASICON	$Na_3V_2(PO_4)_3$	$R\bar{3}c$	$V^{3+/4+}$	Oc-cor-Te_X-cor-Oc	6	SIB	3.4	118 (2Na)/115	116
	$Na_3V_2(PO_4)_3$	$R\bar{3}c$	$V^{2+/3+}$	Oc-cor-Te_X-cor-Oc	6	PIB	1.4	113 (2K)/100	This work
	$K_3V_2(PO_4)_3$	$R\bar{3}c$	$V^{3+/4+}$	Oc-cor-Te_X-cor-Oc	6	PIB	3.7	101 (2K)/80	119
	$NaTi_2(PO_4)_3$	$R\bar{3}c$	$Ti^{3+/4+}$	Oc-cor-Te_X-cor-Oc	6	SIB	2.1	133 (2Na)/130	120
	$NaFe_2PO_4(SO_4)_2$	$R\bar{3}c$	$Fe^{2+/3+}$	Oc-cor-Te_X-cor-Oc	3	SIB	3.1	100 (2Na)/90	123
Tavorite and triplite	$NaVPO_4F$	I_4/mmm	$V^{3+/4+}$	Oc-cor-Te_X-cor-Oc	4	SIB	3.8	143 (2Na)/133	131
	$NaFeSO_4F$	$P2_1/c$	$Fe^{2+/3+}$	Oc-cor[F]-Oc	3	SIB	3.55	138 (1Na)/75	135
$KTiOPO_4$ type	$KTiOPO_4$	$Pna2_1$	$Ti^{3+/4+}$	Oc-cor-Oc	3.5	PIB	0.8	135 (1K)/130	139
	$KVOPO_4$	$Pna2_1$	$V^{4+/5+}$	Oc-cor-Oc	3.5	PIB	3.95	133 (1K)/84	142
	$KVPO_4F$	$Pna2_1$	$V^{3+/4+}$	Oc-cor[F]-Oc	4	PIB	4.05	131 (1K)/92	142
	$KTiPO_4F$	$Pna2_1$	$Ti^{3+/4+}$	Oc-cor[F]-Oc	4	PIB	3	133 (1K)/97	144
	$KFeSO_4F$	$Pna2_1$	$Fe^{3+/4+}$	Oc-cor[F]-Oc	3	PIB	3.6	127 (1K)/111	145
Alluaudite	$Na_{0.67}FePO_4$	$C2/c$	$Fe^{2+/3+}$	Oc-ed-Oc	4	SIB	2.5	154 (1Na)/143	147
	$Na_2Fe_2(SO_4)_3$	$C2/c$	$Fe^{2+/3+}$	Oc-ed-Oc	4	SIB	3.8	120 (2Na)/102	148
Others	$Na_3V_2(PO_4)_2F_3$	*Cmcm*	$V^{3+/4+}$	Oc-cor[F]-Oc	4	SIB	3.75	128 (2Na)/114	152
	$Na_3V_2(PO_4)_2F_3$	*Cmcm*	$V^{3+/4+}$	Oc-cor[F]-Oc	4	PIB	3.7	128 (2Na)/100	154
	$Na_3V_2O_{2x}(PO_4)_2F_{3-2x}$	*Cmcm*	$V^{3+/4+}$	Oc-cor[F]-Oc	4	SIB	3.6	130 (2Na)/125	153
	$Na_3V_2O_{2x}(PO_4)_2F_{3-2x}$	*Cmcm*	$V^{3+/4+}$	Oc-cor[F]-Oc	4	PIB	3.8	130 (2Na)/118	154
	$Na_2FeP_2O_7$	$P\bar{1}$	$Fe^{2+/3+}$	Oc-cor-Te_X-cor-Oc	5	SIB	2.9	97 (2Na)/84	157
	$Na_2FeP_2O_7$	$P\bar{1}$	$Fe^{2+/3+}$	Oc-cor-Te_X-cor-Oc	5	PIB	2.8	97 (2Na)/77	159
	$Na_2MnP_2O_7$	$P\bar{1}$	$Mn^{2+/3+}$	Oc-cor-Te_X-cor-Oc	5	SIB	3.4	93 (2Na)/80	160
	$Na_2CoP_2O_7$	$Pna2_1$	$Co^{2+/3+}$	Te-cor-Te_X-cor-Te	4	SIB	4	96 (2Na)/78	161
	$Na_4Fe_3(PO_4)_2(P_2O_7)$	$Pn2_1a$	$Fe^{2+/3+}$	Oc-cor-Sp	3	SIB	3.1	129 (3Na)/100	165
	$Na_4Fe_3(PO_4)_2(P_2O_7)$	$Pn2_1a$	$Fe^{2+/3+}$	Oc-cor-Sp	3	PIB	2.8	129 (3Na)/118	165
	KVP_2O_7	$P2_1/c$	$V^{3+/4+}$	Oc-cor-Te_X-cor-Oc	5	PIB	4.5	101 (1K)/60	170

[a] Oc = MO_6 octahedron; Te = MO_4 tetrahedron; Sp = MO_5 square pyramid; Te_X = XO_4 tetrahedron; Oc-cor-Oc = corner sharing two MO_6 octahedra; Oc-cor[F]-Oc = F atom in the corner sharing bond between two octahedra; Oc-ed-Oc = edge sharing two MO_6 octahedra. * Numbers of alkali metal ions were used for theoretical capacity calculation.

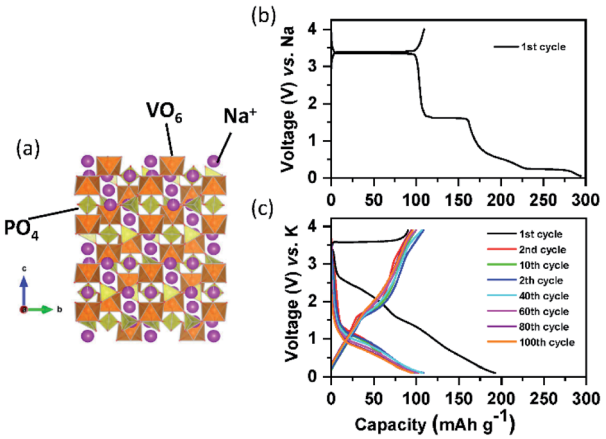

Fig. 10 (a) Structural diagram of $Na_3V_2(PO_4)_3$; charge/discharge curves of the carbon coated $Na_3V_2(PO_4)_3$ composite in the (b) SIB and (c) PIB.

earth metal, or vacancy, M is any of the trivalent, tetravalent, or pentavalent transition metal alone or in combination, and X is one of P, S, Si, or As.[112] The valence of transition metals is varied between divalent and pentavalent to realize charge neutrality in the compounds. The NASICON type structure (Fig. 10a) consists of a three-dimensional network made up of MO_6 octahedra sharing all their corners with XO_4 tetrahedra and *vice versa* to form so-called lantern units ($M_2(XO_4)_3$). The lantern units are aligned parallel to each other, offering a free space for A^+ migration, and the number of commonly shared oxygen of six.[113] Despite the high value, its effect on redox potential is negligible because the MO_6 octahedron shares its six ligand (O) commonly with other polyhedral groups, and thereby the covalency of six M–O bonds is equal. NASICON type materials have been promising electrode materials due to their high ionic conductivity and structural stability. However, their low-activity polarons for electron transfer due to the absence of direct contact between MO_6 octahedra leads to low electronic conductivity.

Since lithium vanadium phosphate, $Li_3V_2(PO_4)_3$ (LVP) is the first positive electrode material applied to LIBs among the NASICON type compounds, its electrochemical behaviors will be compared to those of Na and K counterparts. LVP displays a voltage plateau at around 3.7 V (*vs.* Li/Li^+) based on the $V^{3+/4+}$ redox potential, corresponding to a two-phase transition between the compositions of $Li_3V_2(PO_4)_3$ and $LiV_2(PO_4)_3$.[114,115] Sodium vanadium phosphate, $Na_3V_2(PO_4)_3$ (NVP) exhibits exactly the same reaction with a flat voltage plateau at about 3.4 V (*vs.* Na/Na^+), corresponding to the reactions from $Na_3V_2(PO_4)_3$ to $NaV_2(PO_4)_3$ and *vice versa*.[116] Inspired by NVP, potassium vanadium phosphate, $K_3V_2(PO_4)_3$ (KVP), has been studied by a few research groups[117,118] and is usually prepared by the sol–gel reaction. In contrast to the NVP case, asymmetric charge/discharge profiles are observed. Upon depotassiation, KVP delivers a capacity of 55 mA h g^{-1} (about half of its theoretical capacity), with reaction from $K_3V_2(PO_4)_3$ to $K_{1.5}V_2(PO_4)_3$, which is reversible, and its mid-point discharge voltage is 3.7 V (*vs.* K/K^+). During potassiation, extra K^+ can be inserted into the $K_3V_2(PO_4)_3$ using the $V^{2+/3+}$ redox couple, forming the final composition of $K_4V_2(PO_4)_3$ and its mid-point discharge voltage is 1.4 V (*vs.* K/K^+).[119] Our group studied a Na-based carbon-coated NVP composite in both the NIB and PIB. As shown in Fig. 10b, NVP shows three flat voltage plateaus on the first cycle, corresponding to three different two-phase reactions during sodiation in the voltage window of 3.9–0.05 V (*vs.* Na/Na^+). In contrast, NVP shows no clear plateaus upon potassiation between 3.9 and 0.05 V (*vs.* K/K^+) (Fig. 10c). Although the exact exchange mechanism between Na^+ and K^+ upon depotassiation is under investigation, the sloping voltage profiles upon potassiation imply that K^+ can insert into the structure due to the large enough empty space. From comparison between the first and second cycle, there is a high irreversible capacity due to the electrolyte decomposition in the first discharge and therefore in the second cycle onwards less K^+ is reversibly inserted into the NVP structure. Similar to $A_3V_2(PO_4)_3$, $ATi_2(PO_4)_3$ (A = Li and Na) compounds, adopting the NASICON structure, are also electrochemically active in LIBs and SIBs based on the $Ti^{3+/4+}$ redox couple of 2.4 V (*vs.* Li/Li^+) and 2.1 V (*vs.* Na/Na^+). As a characteristic of NASICON type compounds, $NaTi_2(PO_4)_3$ also shows an excellent 3D open crystal structure, leading to superior A^+ migration.[120]

There are only two NASICON type sulfates reported for alkali metal ion battery applications: $Fe_2(SO_4)_3$ and $NaFe_2PO_4(SO_4)_2$. The former one contains no A^+ at the pristine state, but Li^+ and Na^+ can be inserted and extracted reversibly in the LIB and SIB, respectively. It is shown that the maximum insertion is restrained to about 1 Li^+ and 0.6 Na^+ per $Fe_2(SO_4)_3$.[121] Both, $Fe_2(SO_4)_2$ and $NaFe_2PO_4(SO_4)_2$ demonstrate the same average $Fe^{2+/3+}$ redox potential of 3.1 V (*vs.* Na/Na^+).[122,123] Even though high electronegativity $(SO_4)^{2-}$ may increase the Fe–O bond ionicity, all the six oxygens of FeO_6 participate in primary and secondary inductive effects, and thereby the resultant effect of $(SO_4)^{2-}$ on the redox centre is insignificant in the NASICON phase. This is different from the cases in the alluaudite phase that will be discussed later. $NaFe_2PO_4(MoO_4)_2$ is another example having the $Fe^{2+/3+}$ redox couple (2.5 V *vs.* Na/Na^+) and crystallizing in the NASICON type structure. Astonishingly, $NaFe_2PO_4(MoO_4)_2$ has high electronic conductivity due to the formation of Mo 4d orbitals at the bottom of the conduction band, which results in the formation of electronically connective MoO_4 groups in this compound.[124] Despite the general trend of low electronic conductivity for NASICON type compounds, the NASICON structure offers a rich ability for chemical substitution, which can be an effective way to increase the working voltage of the positive electrodes as shown in $Na_2TiV(PO_4)_3$, $Na_3FeV(PO_4)_3$, $Na_4MnV(PO_4)_3$, $Na_3MnZr(PO_4)_3$, and $Na_3MnTi(PO_4)_3$.[112,125] In addition, various methods such as carbon coating and reducing the particle size have been shown to improve the electronic conductivity, eventually providing satisfactory electrochemical properties.[100,126]

3.3. Tavorite and triplite types

Tavorite is a type of structure for polyanion compounds with a general formula of $AMXO_4Y$ (A = Li, Na, K; M = Fe, V, Mn, Ti; X

= P, S; Y = OH, O, F). The Y atoms are coordinated to M to form the *trans*-coordinated MO_4F_2 octahedron and infinite [Y–MO_4–Y–MO_4–] chains, and XO_4 tetrahedra connect to these chains to form a 3D network as well as channels for A^+ diffusion. The number of commonly shared oxygen by MO_4F_2, AO_X, and XO_4 polyhedral groups is three in the tavorite structured materials. Tavorite-type phosphates such as $LiFePO_4F$[127] and $LiFePO_4OH$ have been studied as positive electrode materials for LIBs. Unlike the materials mentioned above, the Fe ions in these phosphate materials are initially trivalent, and the electrochemical test generally starts from lithiation. These materials show an average lithiation potential of 2.7 and 2.6 V (*vs.* Li/Li^+),[128] respectively, *via* $Fe^{2+/3+}$ reduction. Comparing the redox potentials of $LiFePO_4F$ and $LiFePO_4OH$, it is clear that the relatively high electronegativity of F provides a slightly higher redox potential in a given structure. Vanadium based tavorite $LiVPO_4F$ and $NaVPO_4F$ are also reported as high-capacity positive electrode materials. $LiVPO_4F$ and $NaVPO_4F$ deliver an average voltage of 4.3 V (*vs.* Li/Li^+) and 3.8 V (*vs.* Na/Na^+), respectively. In particular, the high working voltage in $NaVPO_4F$ can be explained by the primary inductive effect of F and the four commonly shared oxygen.[129–131]

$LiFeSO_4F$ is an interesting material as it can crystallize in either tavorite or triplite type, as shown in Fig. 11a and b, respectively. An interesting point is that triplite $LiFeSO_4F$ shows a higher voltage of 3.9 V (*vs.* Li/Li^+) than that of tavorite $LiFeSO_4F$ (3.6 V *vs.* Li/Li^+) and the voltage is the highest among Fe-based polyanion compounds reported. This particularly high voltage relies on its crystal structure. In the triplite $LiFeSO_4F$, two F atoms are arranged into a FeO_4F_2 octahedron in a *cis*-coordination, and are shared by two adjacent FeO_4F_2 octahedra to form a shared F–F edge.[94] Furthermore, the number of the commonly shared oxygen is three, while the tavorite type has two commonly shared oxygen. The voltage increase in triplite $LiFeSO_4F$ is directly related to the *cis*-configurations of the F in FeO_4F_2, not because of the strong Fe^{3+}–Fe^{3+} repulsive interactions in the edge-sharing mechanism.[132,133] Preliminary electrochemical properties of tavorite type $NaFeSO_4F$ are reported, and 55% of the theoretical capacity is achieved with a plateau near 3.55 V (*vs.* Na/Na^+).[134] The Na^+ migration energy in $NaFeSO_4F$ is *ca.* 0.9 eV; higher than the Li^+ migration energy of 0.4 eV in $LiFeSO_4F$. The difference is due to the size effect of A^+ in the same structure – small size Li^+ favors the 3D pathway in $LiFeSO_4F$ while larger size Na^+ mobility takes place within the 1D channels in $NaFeSO_4F$.[135]

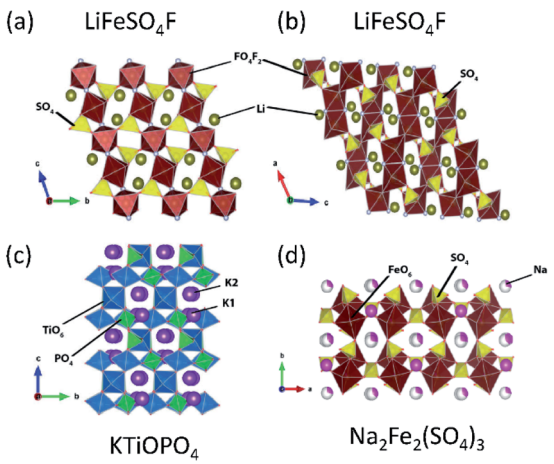

Fig. 11 Typical compounds representing (a) tavorite, (b) triplite, (c) $KTiOPO_4$, and (d) alluaudite types.

3.4. $KTiOPO_4$ type

The $KTiOPO_4$ structure comprises a three-dimensional framework of MO_4Y_2 octahedra and XO_4 tetrahedra with a formula of $AMXO_4Y$. The corner-sharing MO_4Y_2–MO_4Y_2 octahedra form infinite chains along the *bc* plane, and A^+ ions are located in the channels (Fig. 11c), providing extraordinary mobility of K^+ ions: high ionic conductivity around 10^{-4} S cm^{-1} at room temperature.[136] Hence, this structural type is attractive for designing electrode materials for alkali metal ion batteries.[137,138] Even though the $KTiOPO_4$ structure has four commonly shared oxygens, the covalency of Ti–O bonds slightly decreases due to the distortion in the octahedron induced by *cis*- and *trans*-configurated oxygen compared to other frameworks. $KTiOPO_4$ itself demonstrates a mid-point discharge voltage of 0.8 V (*vs.* K/K^+) *via* the $Ti^{3+/4+}$ redox reaction, thereby being unsuitable for a positive electrode material despite a discharge capacity of 135 mA h g^{-1}.[139] Replacing V for Ti in the same structure enables the $V^{4+/5+}$ redox couple to be used as shown in $LiVOPO_4$, $NaVOPO_4$, and $KVOPO_4$ with the mid-point discharge voltage of 3.9 V (*vs.* Li/Li^+),[140] 3.5 V (*vs.* Na/Na^+),[141] and 3.95 V (*vs.* K/K^+).[142] In particular, the $KTiOPO_4$ type materials are attractive for PIBs, and one of the promising materials is $KVPO_4F$. This compound shows a wider open framework than $KVOPO_4$, assembled by corner-sharing $V^{3+}O_4F_2$ octahedra and PO_4 tetrahedra, lowering the activation energy of K^+.[143] In addition, its average high mid-point discharge voltage of 4.05 V (*vs.* K/K^+) is due to the highly electronegative F atoms. $KTiPO_4F$ shows *cis*- and *trans*-configuration effects since two different TiO_4F_2 octahedra exist as a result of the F configuration within the TiO_4F_2 octahedra: one with *cis*-configurated F and another with *trans*-configurated F. The $Ti^{3+/4+}$ redox in *trans*-configurated TiO_4F_2 octahedra is reflected in the lower slopy plateau at 2.9 V (*vs.* K/K^+) while that in *cis*-configurated octahedra shows a plateau around 3.5 V (*vs.* K/K^+).[144] Similar influence is observed in $KFeSO_4F$, *i.e.*, $Fe^{2+/3+}$ redox potential at 3.5 and 4.1 V (*vs.* K/K^+) originating from the *trans*- and the *cis*-configuration of F, respectively.[145]

3.5. Alluaudite type

Alluaudite type compounds have the general formula of $AA'MM'_2(XO_4)_3$. The structure consists of infinite chains of edge-sharing MO_6 and $M'O_6$ octahedra, and XO_4 tetrahedra link these chains to form a 3D architecture with two tunnels where the A and A′ ions are located (Fig. 11d). So far, only one alluaudite structured material has been reported for LIBs, *i.e.*, $Li_{0.67}FePO_4$, prepared by the soft chemical ion-exchange method.[146] Its redox potential of $Fe^{2+/3+}$ is lower (3.0 *vs.* Li/Li^+) than that of triphylite $LiFePO_4$ (3.4 *vs.* Li/Li^+) probably due to the less localized charge in Fe as a result of edge-sharing of all FeO_6

octahedra, and the reduced inductive effect due to the corner-sharing between FeO_6 and PO_4 in the alluaudite.[146] In SIBs, the alluaudite type $Na_{0.67}FePO_4$/CNT composite electrode delivers a discharge capacity of 143 mA h g^{-1} based on the $Fe^{2+/3+}$ redox reaction (2.5 V *vs.* Na/Na^+) and exhibits stable cyclability.[147] Yamada *et al.* reported that the alluaudite type $Na_2Fe_2(SO_4)_3$ demonstrates the redox potential of $Fe^{2+/3+}$ at 3.8 V (*vs.* Na/Na^+) and fast kinetics, which draws much attention for the low-cost Fe-based sulfates for SIBs.[148] Another alluaudite type Fe-based sulfate is $Na_2Fe(SO_4)_2$ (can be described as $Na_3Fe_{1.5}(SO_4)_3$) that displays a high operating voltage of around 3.6 V (*vs.* Na/Na^+) based on the $Fe^{2+/3+}$ redox couple as well as superior thermal stability (around 580 °C).[149] These alluaudite type sulfate compounds show higher voltage compared to the NASICON type $Na_xFe_2(SO_4)_3$ due to the more covalent Fe–O bonds originating from the six equal corner sharing mechanism between FeO_6–SO_4 polyhedra and four commonly shared oxygens.[121]

3.6. Other types

Sodium vanadium oxyfluoride phosphates, $Na_3V_2O_{2x}(PO_4)_2F_{3-2x}$ ($0 \le x \le 1$),[150,151] have been gaining much attention since the successful implementation of $Na_3V_2(PO_4)_2F_3$ in Tiamat's prototype SIB cells. In the structure of the $Na_3V_2O_{2x}(PO_4)_2F_{3-2x}$ family, MO_4F_2 octahedra are corner-shared *via* their *trans*-configurated F and form a $M_2O_8F_3$ octahedron dimer. This dimer is bridged by PO_4 tetrahedra, building a 3D framework and offering Na^+ migration channels along the *a* and *b*-axes. The number of the commonly shared oxygen is four. All compounds in this family have three Na^+ ions occupying two different sites: two fully filled Na(1) sites and two half-filled Na(2) sites. Even though one can see two main voltage plateaus at 3.6 V and 4.1 V in the charge–discharge curves, precise mechanistic studies reveal more voltage plateaus and very complicated reactions, which include the multiple redox processes of vanadium ions through vanadium's disproportionation ($2V^{4+} \rightarrow V^{3+} + V^{5+}$) and simultaneous extraction/insertion of Na^+ from/into the both sites (Fig. 12).[152] The phase evolution is rather complicated: three biphasic reactions of $Na_3V_2(PO_4)_2F_3$–$Na_{2.4}V_2(PO_4)_2F_3$, $Na_{2.4}V_2(PO_4)_2F_3$–$Na_{2.2}V_2(PO_4)_2F_3$, and $Na_{2.2}V_2(PO_4)_2F_3$–$Na_2V_2(PO_4)_2F_3$ in the lower voltage region and two biphasic and one monophasic reactions of $Na_2V_2(PO_4)_2F_3$–$Na_{1.8}V_2(PO_4)_2F_3$, $Na_yV_2(PO_4)_2F_3$ ($1.8 < y < 1.3$), and $Na_{1.3}V_2(PO_4)_2F_3$–$NaV_2(PO_4)_2F_3$ in the higher voltage region during the charging process.[153] Recently, our group observed excellent electrochemical properties of the $Na_3V_2O_{2x}(PO_4)_2F_{3-2x}$/MWCNT composite in K cells. The composite electrode delivers an initial discharge capacity of 118 mA h g^{-1} at 13 mA g^{-1} with a mid-point discharge voltage of 3.8 V (*vs.* K/K^+). During the first charge, two Na^+ ions are extracted from $Na_3V_2O_{2x}(PO_4)_2F_{3-2x}$ and form $NaV_2O_{2x}(PO_4)_2F_{3-2x}$. The remaining one Na^+ is exchanged with K^+ during subsequent discharge, producing $K_3V_2O_{2x}(PO_4)_2F_{3-2x}$. Once $K_3V_2O_{2x}(PO_4)_2F_{3-2x}$ is formed insertion/extraction of K^+ take place reversibly, maintaining $K_3V_2O_{2x}(PO_4)_2F_{3-2x}$ at the end of 4th discharge.[154]

In 2010, Yamada and co-workers successfully developed a new polyanionic group, pyrophosphate $(P_2O_7)^{4-}$ to increase the $M^{n+/(n+1)+}$ redox potential.[155] They have reported the electrochemical and structural characteristics of new pyrophosphate compounds $A_2MnP_2O_7$ (A = Li and Na; M = Fe, Mn and Co) synthesized by a conventional solid–state reaction. In α-$Li_2FeP_2O_7$ (space group of $P2_1/n$), FeO_6 octahedra and FeO_5 pyramids are connected in an edge-sharing manner. The redox potential of Fe in the FeO_5 pyramid is affected by the commonly shared oxygen atoms and more attractive interaction between Fe and O atoms in FeO_5 than in FeO_6 delivers a higher redox potential of $Fe^{2+/3+}$. Based on the calculation, 3.9 V (*vs.* Li/Li^+) is anticipated, however the experimental redox voltage is 3.5 V (*vs.* Li/Li^+) due to structural rearrangement related to Fe migration.[156] In SIBs, β-$Na_2FeP_2O_7$ (space group of $P\bar{1}$) shows two different voltage plateaus at 2.9 V and 2.5 V (*vs.* Na/Na^+), because of two distinct constituent Fe sites.[157,158] $Na_2FeP_2O_7$ also shows K^+ storage ability with a mid-point discharge voltage of 2.8 V (*vs.* K/K^+), however huge polarization and a slopy voltage plateau are observed due to the size of K^+.[159] As expected, replacing Fe with Mn or Co provides a higher mid-point discharge voltage, which is shown in $Na_2MnP_2O_7$ with 3.4 V (*vs.* Na/Na^+)[160] and $Na_2CoP_2O_7$ with 4.0 V (*vs.* Na/Na^+).[161] $Na_2CoP_2O_7$ adopts a layered structure where each of four O in a CoO_4 tetrahedron is linked with four of the surrounding PO_4 units to form $[Co(P_2O_7)]_{22}$ layers parallel to ⟨001⟩ and stacked alternately with a layer of Na. In this layered structure, $Na_2CoP_2O_7$ demonstrates mid-point discharge voltage at 4.0 V (*vs.* Na/Na^+) *via* $Co^{2+/3+}$. This difference might be explained by the less ionic character of Co–O bonds in the tetrahedral coordination.[162]

Mixed phosphates of $Na_4M_3(PO_4)_2(P_2O_7)$ using $M^{2+/3+}$ have emerged as promising positive electrode materials for NIBs, which are unique frameworks only obtained in the Na system using direct synthetic methods. In particular, cost effective Fe-containing $Na_4Fe_3(PO_4)_2(P_2O_7)$ shows low volume change during desodiation/sodiation (<4%) *via* a one-phase reaction and superior thermal stability.[163,164] The trivial volume variation is attributed to the P_2O_7 bitetrahedron that is able to rotate and distort to accommodate the structural change in the desodiated

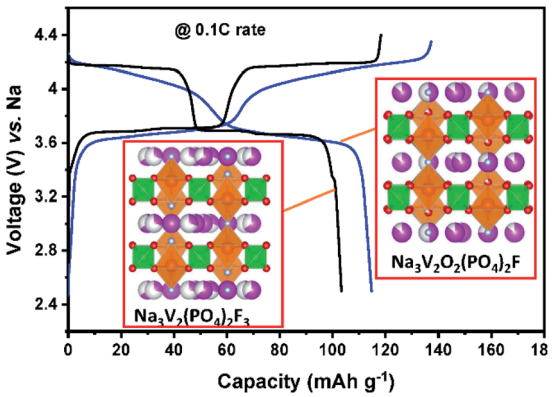

Fig. 12 Charge/discharge curves of $Na_3V_2(PO_4)_2F_3$ in black and $Na_3V_2O_2(PO_4)_2F$ in blue for SIBs. Both structures show the connectivity of VO_6 (orange) octahedra and PO_4 (green) tetrahedra along the [010] direction. The pink, red, and silver balls represent sodium, oxygen, and fluorine, respectively.

phase of $NaFe_3(PO_4)_2(P_2O_7)$ in a reversible way.[165] The replacement of Fe with Co[166] or Ni[167] raises the $M^{2+/3+}$ redox potential from 3.2 to 4.5 or 4.8 V (*vs.* Na/Na^+), respectively. However, electrochemical performances of $Na_4Co_3(PO_4)_2(P_2O_7)$ and $Na_4Ni_3(PO_4)_2(P_2O_7)$ are not as good as $Na_4Fe_3(PO_4)_2(P_2O_7)$, and the Co containing compound exhibits complex phase transformation upon charge including four biphasic and a solid-solution reactions.[168,169]

Park *et al.* carried out computation studies to propose suitable high voltage polyanionic compounds for PIBs.[170] They found seven electrochemically active pyrophosphate compounds ($KCrP_2O_7$, $KFeP_2O_7$, $KTiP_2O_7$, KVP_2O_7, $KMoP_2O_7$, $K_2(VO)_3(P_2O_7)_2$, and $K_2MnP_2O_7$). Among these, redox potentials of $KCrP_2O_7$ and $KFeP_2O_7$ are suggested to be beyond the stability window of common electrolytes. Experimentally, KVP_2O_7 is shown to deliver 60% of its theoretical capacity (based on $V^{3+/4+}$) with a mid-point discharge voltage of 4.5 V (*vs.* K/K^+).[170] Structural investigation reveals that KVP_2O_7 crystallizes in the monoclinic phase in which VO_6 octahedral groups corner-share with the P_2O_7 diphosphate group and have one-dimensional diffusion pathways along the ⟨001⟩ direction. The monoclinic KVP_2O_7 undergoes reversible phase transformation into triclinic ($P\bar{1}$) $K_{0.4}VP_2O_7$ at the fully depotassiated state.

Overall, polyanionic compounds deliver a high redox potential along with high structural stability, and in consequence high energy density and higher thermal stability related to battery safety. However, they have inherently low electronic conductivity and should be prepared along with different carbonaceous materials to provide efficient electron conduction paths in the composite electrode.

4. Prussian blue analogues

As discussed in the previous polyanion compound section, open structures are preferable for the electrochemical insertion of larger A^+ such as Na^+ and K^+. Among the various 3D framework materials, open-channel hexacyanometallate compounds, also known as PBAs, have been studied as Li^+,[171] Na^+,[172] and K^+[173–175] insertion hosts. Generally, Prussian blue ($K_xFe[Fe(CN)_6]_y$) is well known as a traditional pigment. Although it comprises cyanide, it is not toxic because of the extraordinary stability of the $[Fe(CN)_6]^{4-/3-}$ complex. Various PBAs containing different metals have also been reported. The chemical formula of PBAs is represented as $A_xM1[M2(CN)_6]_y \cdot nH_2O$ ($0 \leq x \leq 2$, $y \leq 1$), where A is typically an alkali metal, and M1 and M2 can be various metals such as Ti, V, Cr, Fe, Co, Ni, Cu, and Zn. $A_xM1[M2(CN)_6]_y \cdot nH_2O$ is abbreviated as M1M2–PBA or AM1M2–PBA for simplicity hereafter.

Fig. 13a and b illustrate a typical crystal structure of $A_0M1[M2(CN)_6]$ and $A_2M1[M2(CN)_6]$, respectively. PBAs have 3D open-frameworks in which $M1N_6$ and $M2C_6$ octahedra are

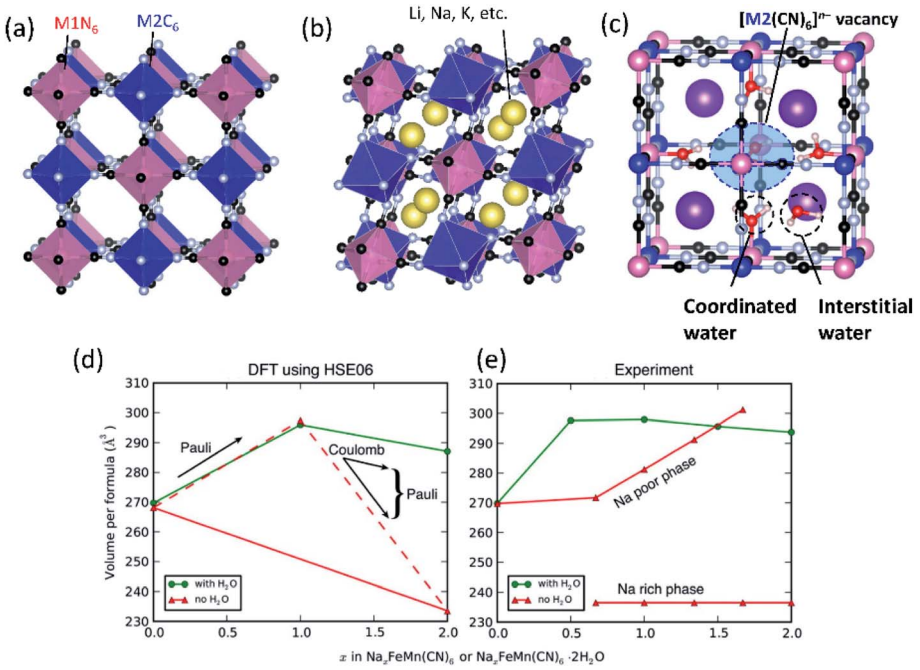

Fig. 13 Crystal structures of (a) $A_0M1[M2(CN)_6]$ and (b) $A_2M1[M2(CN)_6]$, where A is an alkali metal, and M1 and M2 can be various metals. The blue and pink polyhedra represent $M1N_6$ and $M2C_6$, while the yellow spheres represent alkali metals. (a) and (b) are reproduced with permission from ref. 4. Copyright 2020 American Chemical Society. (c) Structure of the domain with the $[M2(CN)_6]^{n-}$ vacancy, where oxygen and hydrogen atoms of interstitial and coordinated water are represented as red and pale pink spheres, respectively. Volume change comparison of NaMnFe–PBA between (d) theory and (e) experiment. In the DFT results, the solid lines represent the average volume of the formula unit in the crystal under equilibrium conditions. The dashed red line is out of equilibrium, in which the half-filled Na structure, slightly above the convex hull, is assumed to be formed. In the experimental results, the volume of the Na poor and rich phases is determined separately, and the value of *x* is an average of these two phases. (d) and (e) are reproduced with permission from ref. 176. Copyright 2015 American Chemical Society.

linked *via* cyano ligands.[176] The framework structure provides an open 3D channel available for mobile metal diffusion, which is suitable for the diffusion of large ions. Another feature of PBAs is the different spin states of the transition metals in the $M1N_6$ and $M2C_6$ octahedra, which is explained by the ligand field theory. For transition metals such as Fe and Mn, the high-spin (HS) M1 is located in the $M1N_6$ octahedron, while the low-spin (LS) M2 is located in the $M2C_6$ octahedron owing to their respective weak N-coordinated and strong C-coordinated ligand fields.[177] PBAs usually have the $[M2(CN)_6]^{n-}$ anion vacancy in the framework as shown in Fig. 13c. In addition, the framework contains two kinds of crystal water, *i.e.*, interstitial water in the interstitial site and coordinated water bound to M1 metal next to the anion vacancy (Fig. 13c).

Typical PBAs whose alkali metal content is ≤ 1.5 per formula possess a cubic structure (space group of $Fm\bar{3}m$) in which all the octahedra are arranged linearly (Fig. 13a). On the other hand, the octahedra rotate cooperatively in the alkali metal-rich phase, resulting in monoclinic (space group of $P2_1/n$) or rhombohedral (typically the space group of $R\bar{3}$; Fig. 13b) structures. For example, Na-rich phases have monoclinic structures when water molecules are in the interstitial site (interstitial water), while dehydrated Na-rich PBAs have rhombohedral structures whose lattice volume per formula is smaller than that of the monoclinic phase.[176,178] This structural change is explained by Song *et al.* using experiments and DFT calculations as follows. Fig. 13d and e compare the calculated and experimental volume of the NaMnFe–PBA crystal with or without interstitial H_2O at different Na contents. The DFT calculation shows that the volume of the Na-free structure is essentially the same with and without interstitial H_2O. In the fully sodiated state, the volume of the hydrated phase is larger than that of the desodiated phase. The calculation results are found to be in quantitative agreement with the experimental data (Fig. 13e). The volume reduction of the dehydrated structure indicates that there is a strong coulombic interaction between the intercalated Na^+ and the host framework. On the other hand, the presence of interstitial H_2O in the lattice suppresses the lattice contraction due to the strong Pauli repulsion. Similar to the Na-poor PBAs adopting a cubic phase, K-poor PBAs have a cubic structure. However, K-rich PBAs have monoclinic structures, regardless of the presence of interstitial H_2O.[174,175,179,180] This phenomenon is explained by the large ionic radius of K^+, which increases the Pauli repulsion in the lattice and prevents lattice shrinkage,[178] and the formation of a monoclinic phase with a larger lattice volume than that of the rhombohedral phase. Furthermore, most K-rich PBAs contain significantly less interstitial water[174,175,179] than Na-rich PBAs, which typically contain about 2 mol interstitial water per formula unit.[178] These facts indicate that K^+ and water molecules rarely occupy the interstitial sites of the PBAs simultaneously, because of the limited interstitial space formed by the $[Fe(CN)_6]$ vacancy.

Based on the features of PBAs described above, the material design of PBAs is achieved by varying transition metal species, the amount of crystal water, the type and content of alkali metals, and the number of anion vacancies. The varied transition metals result in a wide variety of redox potentials on Na^+ and K^+ insertion. Among the reported PBAs, $A_2Mn[Fe(CN)_6]$ and $A_2Fe[Fe(CN)_6]$ have attracted attention because of their high reversible capacity and suitable high potential based on $Fe^{2+/3+}$ and $Mn^{2+/3+}$ redox.[175,177,178,181–183] Fig. 14a shows the charge–discharge curves of $K_2Mn[Fe(CN)_6]$ (KMnFe–PBA) and $K_2Fe[Fe(CN)_6]$ (KFeFe–PBA) in K cells.[175] KFeFe–PBA shows two voltage plateaus at around 3.3 and 3.8 V, which are attributed to HS $Fe^{2+/3+}$ and LS $Fe^{2+/3+}$, respectively.[177] As shown in Fig. 14b, in the half-discharged state ($K_1Fe(II)[Fe(II)(CN)_6]$) the high redox voltage of LS $Fe^{2+/3+}$ is due to the stable electronic state $(t_{2g})^6$ and low energy level of the t_{2g} orbital caused by the large ligand field splitting. KMnFe–PBA shows two voltage plateaus at *ca.* 3.8 and 4.1 V. The plateau at *ca.* 3.8 V is attributed to LS $Fe^{2+/3+}$, whereas the higher voltage plateau at *ca.* 4.1 V is attributed to HS $Mn^{2+/3+}$ (Fig. 14). The higher redox potential of HS $Mn^{2+/3+}$ in $K_2Mn[Fe(CN)_6]$ than HS $Fe^{2+/3+}$ in $K_2Fe[Fe(CN)_6]$ results in a higher working potential of $K_2Mn[Fe(CN)_6]$ than that of $K_2Fe[Fe(CN)_6]$. The correlation between the redox potential and transition metals is quite similar to Na cases. Thus, $K_2Mn[Fe(CN)_6]$ and $Na_2Mn[Fe(CN)_6]$ are promising materials in terms of their high redox potential for the positive electrode in a full cell.

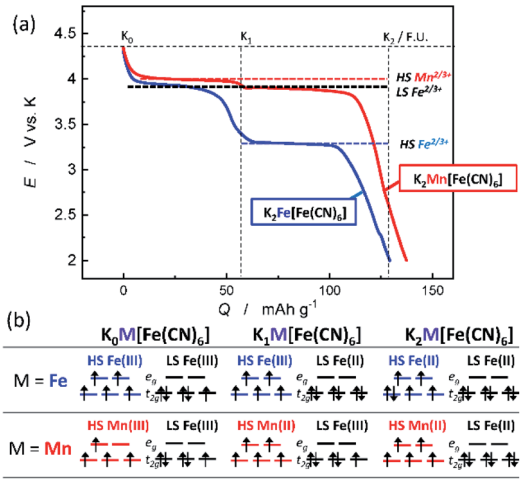

Fig. 14 (a) Typical discharge curves of KFeFe–PBA and KMnFe–PBA in K cells. (b) Electronic structures of $K_xM[Fe(CN)_6]$, where $x = 0$, 1, 2, and M = Fe or Mn.

In addition to the transition metal species, the effects of interstitial water, alkali metal species, and anion vacancies on Na^+ and K^+ insertion have been investigated. In 2015, Song *et al.* reported a significant impact of interstitial water of NaMnFe–PBA on electrochemical properties.[178] Fig. 15a and b show the charge/discharge curves of hydrated NaMnFe–PBA ($Na_{1.89}Mn[Fe(CN)_6]_{0.97}\cdot 1.87H_2O$) and dehydrated ($Na_{1.89}Mn[Fe(CN)_6]_{0.97}$) in Na cells. The hydrated sample exhibits two slopy voltage plateaus in the range of 3.17–3.45 and 3.5–3.8 V, whereas the dehydrated sample shows a single clear plateau around 3.5 V. Soft XAS reveals that the Fe and Mn redox reactions in hydrated electrodes are separated to the lower and higher voltage plateaus, respectively. In contrast, mixed Fe and Mn redox in the same voltage range is found for the dehydrated system.[184] Since the t_{2g} orbital of C-coordinated LS Fe^{2+} has a low energy

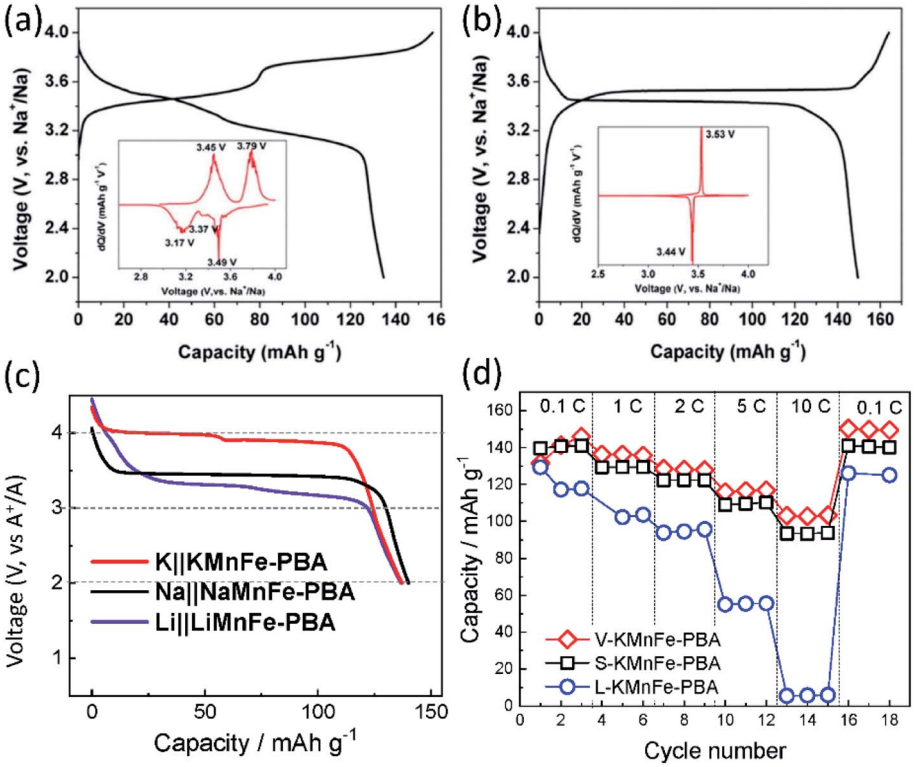

Fig. 15 Initial charge/discharge profiles of (a) hydrated NaMnFe–PBA and (b) dehydrated NaMnFe–PBA. Differential *versus* voltage (d*Q*/d*V*) plots are shown in the insets (a) and (b) are reproduced with permission from ref. 178. Copyright 2015 American Chemical Society. (c) Galvanostatic discharge curves of $Li_xMn[Fe(CN)_6]_y$ (LiMnFe–PBA), $Na_xMn[Fe(CN)_6]_y$ (NaMnFe–PBA), and $K_{1.75}Mn[Fe(CN)_6]_{0.93}$ (KMnFe–PBA) in nonaqueous Li, Na, and K cells, respectively. (d) Variations of discharge capacity of S-KMnFe–PBA, L-KMnFe–PBA, and V-KMnFe–PBA. The electrodes were charged at 0.1C (15.5 mA g^{-1}) and discharged at different discharge current densities. Reproduced with permission from ref. 188. Copyright 2021 Wiley-VCH.

level due to the strong ligand field, the LS $Fe^{2+/3+}$ exhibits a relatively high redox potential in the case of the dehydrated sample. Thus, the redox potential of LS $Fe^{2+/3+}$ is competitive with that of HS $Mn^{2+/3+}$, eventually generating a single potential merged from the two potentials in the dehydrated NaMnFe–PBA. In contrast, the existence of interstitial water is believed to dilute the strong ligand field, resulting in a gap between the redox potentials of $Fe^{2+/3+}$ and $Mn^{2+/3+}$.[184] The structural change caused by the interstitial water would also affect the change in the redox potential. Although hydrated NaMnFe–PBA shows a smaller volume change of about 10% during the charge/discharge process than dehydrated NaMnFe–PBA (*ca.* 27%), the release of crystal water into the electrolyte and the structural change to the dehydrated phase could lead to capacity degradation. Future studies would clarify the effects of volume change and crystal water release on the capacity degradation to develop long-life PBA materials for SIBs. In contrast to the significant effect of interstitial water of Na–PBAs, the interstitial water has no significant influence on the electrochemical performance of KMnFe–PBA in K half-cells,[180] which could be due to the fact that the large K^+ and water molecules hardly occupy the same interstitial sites of the PBA simultaneously.

Since the open-framework structure of PBAs suits reversible storage of different cations, including Li^+, Na^+, and K^+, we compare the electrochemical properties of different A^+ insertions in nonaqueous electrolytes. Fig. 15c summarizes the charge/discharge curves of $Li_xMn[Fe(CN)_6]_y$ (LiMnFe–PBA), $Na_xMn[Fe(CN)_6]_y$ (NaMnFe–PBA), and $K_{1.75}Mn[Fe(CN)_6]_{0.93}$ (KMnFe–PBA) in the Li, Na, and K cells, respectively. The NaMnFe–PBA and KMnFe–PBAs were synthesized by a simple precipitation method. On the other hand, LiMnFe–PBA was synthesized *via* electrochemical ionic exchange in the K cell because it is hardly obtained *via* a simple precipitation method. Fig. 15c illustrates that LiMnFe–PBA, NaMnFe–PBA, and KMnFe–PBA deliver similar discharge capacities of 137, 140, and 137 mA h g^{-1}, respectively. The Mn–Fe-based PBAs exhibit average discharge voltages of 3.3, 3.4 (3.7 V *vs.* Li), and 3.8 V (3.7 V *vs.* Li) in the Li, Na, and K cells, respectively. The specific energy densities of LiMnFe–PBA, NaMnFe–PBA, and KMnFe–PBA were 446, 472, and 521 W h kg^{-1} in the Li-, Na-, and K-metal cells, respectively. These results indicate that PBAs are promising electrode materials, especially for high-energy density SIBs and PIBs.

The effect of anion vacancies on Na^+ insertion performance has been extensively studied, and several studies prove that anion-vacancy free (stoichiometric) Na–PBAs demonstrate larger capacity and better capacity retention in the repeated cycles than the nonstoichiometric Na–PBAs with anion

vacancies.[177,183,185] This larger reversible capacity is attributed to a larger fraction of redox-active Fe in $[Fe(CN)_6]$ vacancy-free samples.[183] Similar to Na–PBAs, a previous study shows that K–PBAs with few anion vacancies exhibit a large reversible capacity.[186] Additionally, it has been suggested that the anion vacancies promote the diffusion of K^+.[187,188] To fully understand the effect of anion vacancies on the K^+ insertion, independent control of the number of anion vacancies and particle size is essential. This is because these two factors generally have a strong negative correlation, *i.e.*, samples with a small particle size have many anion vacancies and *vice versa*. Thus, our group synthesized three KMnFe–PBAs whose particle size and the number of anion vacancies are varied by employing precipitation synthesis with addition of a suitable amount of chelate agent and the Na/K ion exchange route.[188] The chemical composition of the three samples, small (S)-, large (L)-, and anion-vacant (V)-KMnFe–PBAs, are estimated to be $K_{1.9}Mn[Fe(CN)_6]_{1.0}$, $K_{1.8}Mn[Fe(CN)_6]_{0.99}\square_{0.01}$, and $Na_{0.10}K_{1.6}Mn[Fe(CN)_6]_{0.85}\square_{0.15}$, respectively after drying at 200 °C. The particle size of S-KMnFe–PBA ranges in 100–200 nm, whereas the particle size of L- and V-KMnFe–PBA is approximately 1–2 μm. Thus, the effects of particle size and anion vacancies are investigated by comparing S-KMnFe–PBA with L-KMnFe–PBA and L-KMnFe–PBA with V-KMnFe–PBA, respectively. Fig. 15d displays the variation in discharge capacities at different discharge rates from 0.1 to 10C and a constant charge rate at 0.1C. The V-KMnFe–PBA electrode demonstrates superior rate performance to L-KMnFe–PBA and is competitive with that of S-KMnFe–PBA, consisting of much smaller particles. The superior rate performance of V-KMnFe–PBA is attributed to the enhanced K^+ diffusion in the lattice with anion vacancies based on the galvanostatic intermittent titration technique measurements and DFT calculation results.[188] These results prove that the appropriate number of anion vacancies promotes K^+ insertion into PBAs, which is different from the sodium case.

Overall, PBAs are potential positive electrode materials for SIBs and PIBs because of their relatively high gravimetric energy density based on the $Fe^{2+/3+}$ and $Mn^{2+/3+}$ redox and good rate and cycle performance. As a Chinese company, CATL, announced the commercialization of SIBs using PBA as the positive electrode material in July 2021, practical development is expected to be accelerated based on the development of advanced SIB/PIB materials.

5. Carbon-based negative electrode materials

5.1. Types of carbon applied for batteries

While significant effort is being made towards improving and understanding positive electrode material performance for emerging SIBs and PIBs, researchers are also approaching better performance for negative electrode materials. As with positive electrode materials, the structure is key to the interaction with different A^+ and not all electrode materials are equally suitable for Li^+, Na^+ and K^+ ions.[21,189–192] In this section, we

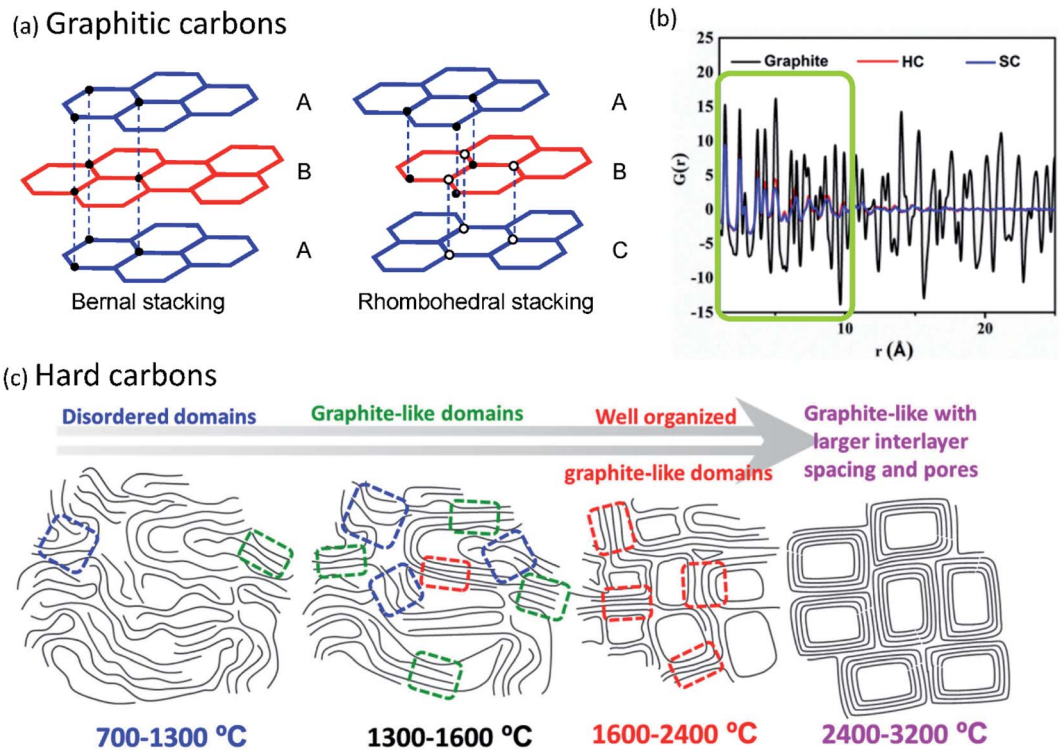

Fig. 16 Structural differences for graphitic and hard carbons. (a) Structure and stacking of graphite. (b) Neutron total scattering showing short- and long-range ordering in different forms of carbon. Reprinted with permission from ref. 272. Copyright 2017 American Chemical Society. (c) Structure of hard carbons prepared with increasing temperature.

discuss carbon-based negative electrode materials which continue to be heavily explored due to their wide array of structure and morphological variability, continued application in modern day LIBs, and promising performance within both SIBs and PIBs.[191,193,194] Aside from being made of an abundant and sustainable material,[195,196] carbon-based negative electrode materials take advantage of multiple features including low cost, good chemical stability, high conductivity, and large specific surface area.[8,191,193] Carbon materials applied in batteries include a variety of structures ranging in dimensionality (*e.g.* 3D, 2D), order (*e.g.* long or short range ordering), and heteroatom doping (*e.g.* N or O adatoms). Among highly ordered carbons, the most common material is based on graphite (Fig. 16a), a negative electrode material extensively applied in commercial LIBs.[191,197] Graphitic carbons are based on a 3D crystalline structure with layered domains of sp^2-hybridized carbon (graphene) that typically follows hexagonal AB stacking (a.k.a. Bernal stacking or 2H) for synthetic graphite;[198,199] though alternative stacking, *e.g.* ABC or rhombohedral (3R), is also found for multi-layered graphene and natural graphite.[200]

The other most common carbon-based electrode materials being applied and explored for battery applications are those based on hard carbons. Unlike graphite, hard carbons do not display a long-range periodic structure in plane or along the stacking direction (Fig. 16b). The name 'hard carbons' for these materials derives from their often observed mechanical hardness and original patent,[201] though they can be relatively soft when prepared under low-temperature conditions. More appropriately, hard carbons can be labelled as non-graphitizable; they do not change to a graphite structure even at very high temperatures (*e.g.* 3000 °C) as demonstrated long ago in the studies of Rosalind Franklin.[202] Many of the structural features found in hard carbons including amorphous regions (sp^3) with randomly aligned sp^2 graphitic microdomains, pore structures, and defect content, are directly impacted by the preparation temperature (Fig. 16c). In contrast, 'soft carbons' have a structure which enables greater mobility in the carbon atoms to rearrange into graphite at temperatures between 1500 and 3000 °C. Preparation of soft carbons under low temperature preparation shows some similar features to hard carbons and can even form hard carbons when heated under an oxygen environment.

The structure of carbon-based materials heavily determines the energy storage mechanism and thus understanding relationships between the structure and performance becomes essential for improving their performance inside batteries. In the following sections, we outline the main progress with different types of carbon-based anode materials applied in LIBs, SIBs and PIBs, discuss their limitations, and highlight research efforts to push these materials to higher performance.

5.2. Graphitic electrodes for Li^+, Na^+, and K^+

Graphite remains one of the most common anode materials for LIBs[191,197] and also is a promising candidate for PIBs.[4,21,192,203,204] The graphite structure features weak van der Waals bonding in the vertical direction between the graphene sheets producing an average interlayer spacing of approximately 3.35 Å. When the graphite electrode is charged, the layers are filled by the intercalated alkali metal atoms (A) (Fig. 17a) and the interlayer spacing increases to accommodate the insertion, as confirmed with *in situ*/*operando* XRD methods.[7,205–208] This process follows a staging mechanism where alkali metal atoms order within domains in the graphite crystal structure and initially are accompanied by empty layers between the A-filled regions forming a series of stages or graphite intercalation compounds (A-GICs), *e.g.* KC_{36}, KC_{24}, KC_8.[21,203,209] The stage-number signifies

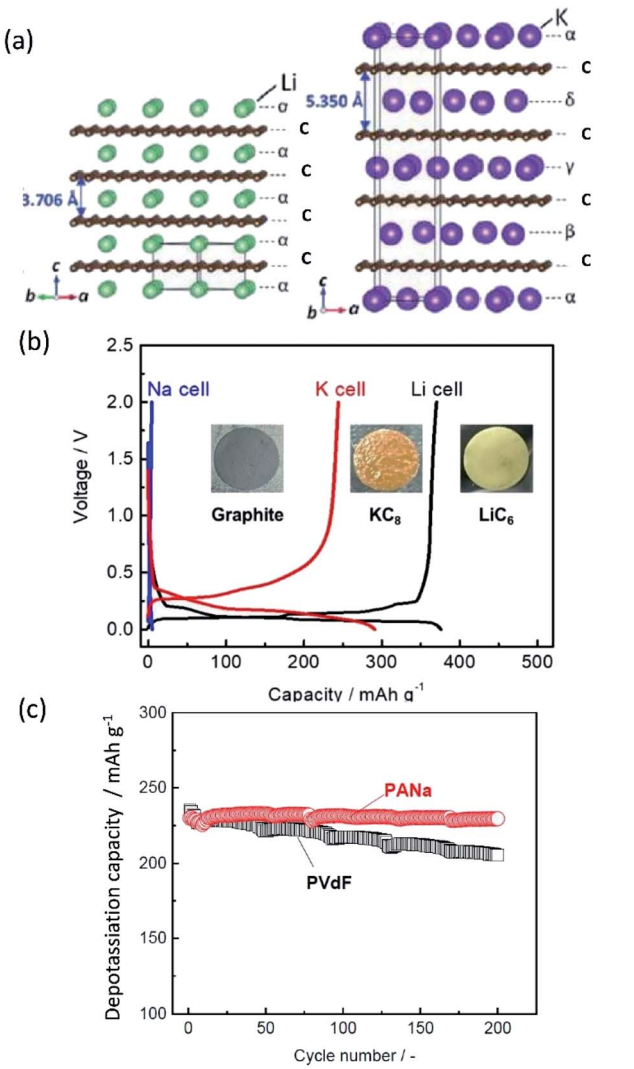

Fig. 17 Comparison of Li, Na and K interaction in the graphite electrode. (a) Difference in inter-layer distance and ordering of alkali metal atoms within the lattice for stage-1 Li-GIC (LiC_6) and K-GIC (KC_8). The organization of Li atoms in subsequent layers is identical, denoted as alpha, while K atoms organize into 4 unique layers with offset positions relative to graphite, denoted as α, β, γ, and δ. C represents a graphene layer. (b) Charge/discharge curves in a K-cell with graphite. Reprinted with permission from ref. 7. Copyright 2018 John Wiley and Sons. (c) Comparison of binder impact on graphite cycling between poly(-vinylidene fluoride) (PVDF) and sodium polyacrylate (PANa). (a) and (c) are reproduced with permission from ref. 205. Copyright 2021, Royal Society of Chemistry.

the number of layers in between the A layers, *e.g.* stage-4 has three empty layers between the subsequent A-filled layers within a four graphene layer domain. Moving from Li to the much larger K leads to an increase in the interlayer distance upon intercalation and some differences in the staging process (Fig. 17a).[21,205] The increased A size also impacts the distance between adjacent A atoms relative to the surrounding carbon atoms,[210] and this leads to a lower number of intercalated A from LiC_6 with a theoretical capacity of 372 mA h g^{-1} to KC_8 with a capacity near 279 mA h g^{-1}.[21,203] Ultimately, the matching of the graphite structure to the intercalated A and chemical affinities are key to the electrochemical (de)intercalation process, where interactions of graphite with A energetically compete with A-to-A and A-to-solvent interactions. The mismatch in structure leads to unfavorable thermodynamic interactions between graphite and Na and poor capacity access during cycling (Fig. 17b), though Na^+ is smaller in ionic radius than K^+.[210–213] Na-GICs have a lower energetic stability and their calculated formation potentials are shown to be below that of sodium metal.[211–215] As such, most research efforts have focused on applying graphite with K^+ and Li^+ for better cyclability and capacity access.

Considering the volume expansion that occurs within graphite during A^+ insertion, the role of the binder becomes vital in maintaining the electrode structure during cycling.[5,216–218] In general, the binder is a polymeric material that functions by adhering the electrode particles together with the current collector; while at the same time, enabling flow of A^+ and solvent molecules to/from the bulk electrolyte. At times, binders also incorporate conductive additives, especially for poorly conductive materials, *e.g.* oxides used as positive electrodes. Commercial binders include polyvinylidene fluoride (PVDF), carboxyl methylcellulose (CMC), and styrene-butadiene rubber (SBR).[216] As seen in Fig. 17c, the choice of binder can significantly impact the capacity retention of the electrodes during cycling.[219] Binders become even more important when considering large increases in interlayer distance, as in the K^+ case, and for some of the emerging high capacity negative electrode materials which undergo more significant volume changes during cycling, *e.g.* Si, P, *etc.*[216,217,220,221] Also, the binder choice can have a direct impact on the forming interphase structures on carbon-based electrodes.[222–225] Recent efforts have pushed to better understand the role of the binder, improve its preparation, and provide more functionality beyond acting as a glue, such as interphase stabilization and inherent conductivity.[216,226–228] Ultimately, the role of the binder remains somewhat overlooked, though it seems to play an important role in achieving higher performance.

In addition, solvated Na^+ ions can interact favorably and form stable intercalation compounds with graphite when their insertion is accompanied by co-intercalating solvent molecules. The reversible formation of these structures, known as ternary graphite intercalation compounds (*t*-GICs), was first pioneered in the work by Jache and Adelhelm.[229] It is reported that *t*-GICs can be formed in a diglyme electrolyte (Fig. 18a) showing reversible insertion of Na^+ with a structure of $Na(diglyme)_2C_{20}$ and capacity close to 100 mA h g^{-1} at 0.1C for 1000 cycles. These solvated Na^+ ions are much larger than the native Na^+, resulting in expansion of the interlayer spacing to very large distances (>10 nm) to accommodate the $Na(diglyme)_2$ insertion (Fig. 18b).[230,231] To date, several ether solvents have been demonstrated to reversibly co-intercalate with Na^+ (Fig. 18c).[230,232,233] The co-intercalation process occurs due to a high Na-solvent solvation energy which maintains a stable Na-solvent structure during insertion.[230,234] In a Na-ion full cell like graphite/Na^+-diglyme/$NaMO_2$, asymmetric reactions of co-intercalation and solvent-free intercalation at graphite and $NaMO_2$ electrodes, respectively, will cause a change in diglyme concentration in the electrolyte, which may be an issue for stable battery operation. Recent research efforts have focused on improving the binder to accommodate this breathing process of large expansion and shrinkage and on manipulation of the material interlayer spacing.[235,236] Likewise, Li^+ and K^+ can form *t*-GICs.[229,237–239] While all three A^+ ions show similar initial capacities, the cyclability of Li^+ *t*-GICs tends to be unstable due to the strong interactions between graphite and Li^+ resulting in

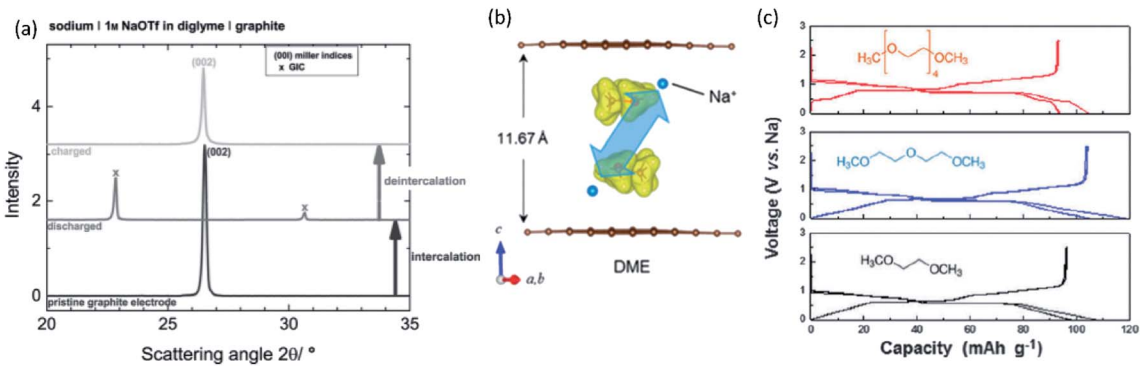

Fig. 18 Na^+ intercalation into graphite *via* solvent co-intercalation. (a) Diffraction patterns of graphite electrodes in 1 M sodium triflate (NaOTf) in diglyme. Bottom: pristine graphite electrode, middle: charged to 0.01 V (*vs.* Na/Na^+), top: discharged to 3.0 V (*vs.* Na/Na^+). Reprinted with permission from ref. 229. Copyright 2014 John Wiley and Sons. (b) Structure of co-intercalated Na^+ in dimethyl ether (DME). (c) Na^+ co-intercalation with graphite during charge/discharge in ether-based solvents of varying chain length; tetraethylene glycol dimethyl ether (red), diethylene glycol dimethyl ether (blue), and dimethoxyethane (black). (b) and (c) reproduced from ref. 230. Copyright 2015, Royal Society of Chemistry.

separation and free solvent that remains in the graphite structure.[237,240] On the other hand, both Na^+ and K^+ *t*-GICs show good cyclability at high rates. Nevertheless, ether-based electrolytes remain limited in their application toward actual batteries due to their narrow voltage windows compared with carbonate ester-based electrolytes.

5.3. Hard carbon electrodes for Li^+, Na^+, and K^+

Hard carbons are promising alternatives to graphite with improved compatibility with Na^+.[189,241,242] They have already been applied as commercialized negative electrodes in LIBs and continue to be used for high power applications.[243] Currently, hard carbons are the negative electrodes of choice and only materials likely to be commercialized for SIBs due to their promising electrochemical properties including: a low working potential, high capacity, good cycling stability;[8,10,190] and their preparation from environmentally friendly, low cost sources.[244–246]

While graphitic carbons mostly rely on (de)intercalation to store energy, hard carbons show a more complex mechanism involving multiple presumed ion storage modes.[194,247–249] Depending on the hard carbon structure, the overall charge/discharge response may result from cumulative reactions including: (i) adsorption/desorption to heteroatom, edge and defect structures, (ii) (de)intercalation processes and (iii) pore-filling.[189,194,249] The (de)intercalation process involves insertion into layered structures of the hard carbon that tends to display greater disorder and interlayer spacing than graphite.[247,248,250] The A^+ adsorption process involves cations adsorbing at edge sites and defects within the pore structure.[249,251] Depending on the adsorption site, A^+ adsorption can either irreversibly trap A^+ ions or enable rapid A^+ migration.[251] The pore-filling process involves adsorption and gradual filling of the pore structures with A^+ leading to high capacities >400 mA h g^{-1}.[252,253]

As seen in Fig. 19a, the electrochemical behavior for this complex mechanism can be broken down into different regions.[253,254] An initial sloping region (red part of the curve) is attributed to adsorption on defects in the pore wall and at edge sites, and A^+ intercalation into defective graphite-like domains.[253] As such, this process is highly dependent on the amount and type of defects in the material. Thereafter, the plateau region involves intercalation into graphitic domains or the formation of island-shaped clusters in the pore wall (blue part of the curve) followed by eventual A^+ filling of the pore structure (green part of the curve).[194,255] To account for observed electrochemical behaviors for various hard carbons, multiple mechanisms incorporating these reactions have been proposed including: adsorption-pore filling,[249] adsorption-intercalation[250] and intercalation-pore filling or the "house of cards" model.[247,248] Considering the vast number of hard carbons that have been explored some materials may show different mechanisms or predominant reactions that are dependent on their structure and energetics for each process.[193,241,242]

The structure and performance are highly impacted by the preparation precursors and temperature as presented in Fig. 19b.[256] Hard carbons for battery applications are typically

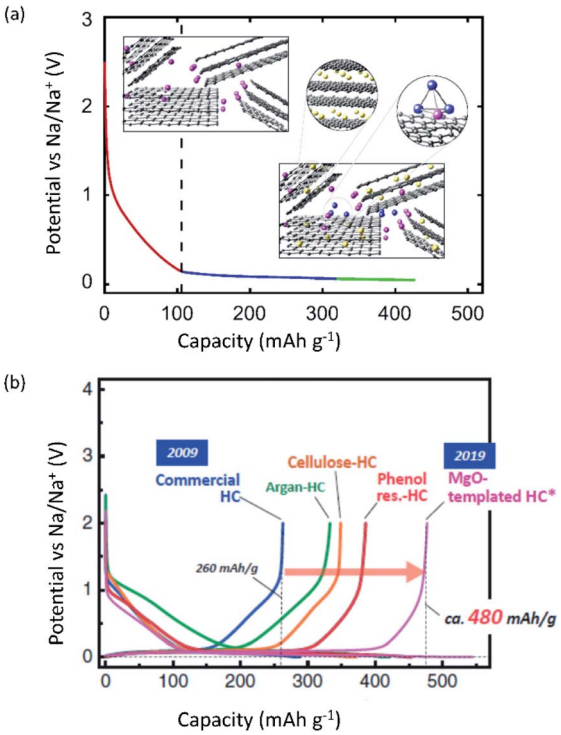

Fig. 19 Impact of the carbon structure on capacity. (a) Proposed alkali ion storage mechanism of hard carbon electrodes. Reprinted with permission from Springer Nature Customer Service Centre GmbH: Springer Nature, *npj Computational Materials*, ref. 253. Copyright 2021. (b) Cycling behavior of hard carbons prepared with different precursors. Reproduced from ref. 256.

prepared through a complex carbonization process involving chemical pre-treatment steps followed by thermal–driven reactions including decomposition of organic materials and σ-bond rearrangement.[241,244] During carbonization, small molecules are removed from the structure including H_2O, CO_2 and N_2 leading to extensive porosity, low apparent desnsity, low particle density, and low bulk powder density.[202,257,258] Interestingly, the prepared hard carbon material tends to maintain much of its original microstructure and morphology based on the parent material. At the same time, very different hard carbon end products with unique structural and morphological properties can be obtained from the same parent material depending on how the hard carbon is prepared.[257,259–261] The final product can be considered a combination of distorted graphene-like nanosheets and fullerenic structures, with edges, defect/heteroatom substitutions, and closed and/or open pores.[262,263] The graphene-type layers are stacked randomly in a turbostratic structure that cannot be unfolded or flattened and contain a wide size-range of voids and pores.[262] The exact nature of these structures can greatly impact electrode performance. Having open structures can enable greater electrolyte penetration leading to high irreversible charge capacities and SEI formation. Materials with large pores may inhibit the effectiveness of the pore-filling mechanism. Not all defect adsorption sites are highly reversible, so the type and amount will impact electrochemical performance. Overall, the structure of hard carbons

can vary substantially, and no single model should be expected to cover all of the possible hard carbon structures, and thus characterization is essential for understanding the origin of high performance or issues with the material.

Recent efforts to further improve the capacity and cyclability of hard carbons have focused on template-synthesis methods.[264,265] Template synthesis involves the incorporation of inorganic materials, such as MgO,[265] zeolites[266] or silica,[267] which act to control the pore structure during synthesis. As discussed above, micro- and nano-pores can accommodate A^+ clusters[252] leading to high capacities with Na^+ (>400 mA h g^{-1}).[264,268] Recently, our group reported novel hard carbon materials that were synthesized *via* a MgO template technique and demonstrated a reversible capacity of 478 mA h g^{-1} at 25 mA g^{-1}.[264] As seen in Fig. 20a–c, the structure of the hard carbon is prepared by tuning the size and concentration of the MgO templates through using mixtures of Mg gluconate (Glu) and glucose (Glc). The compounds were mixed by dry mechanical mixing and freeze–drying methods, Fig. 20a, showing distinct electrochemical behavior (Fig. 20d). The freeze–drying aided in dispersion of the Mg Glu and suppressed its crystallization. Our methods demonstrated the potential for optimizing and improving hard carbon behavior through exploring various synthetic routes. The structure of the pores is not fully understood, yet higher capacities may still be attainable as we come to understand the optimization of this mechanism.

5.4. Other carbon materials

With the vast variety of carbon materials there are other carbon structures being explored for battery applications. Like hard carbons, soft carbons can also be prepared with a structure and mechanism dependent on preparation conditions.[269] These materials show more graphitic character and take advantage of heteroatom doping to give them distinctly different microstructures and energy storage behaviors from hard carbon or graphite.[194,270–273] Soft carbons contain significant sp^2 carbon and layers with interlayer distances greater than that found in natural graphite enabling (de)intercalation even for Na^+.[202,272] In 1991, soft carbons were used as the negative electrode materials in Sony's first-generation of LIBs,[243] and their energy storage mechanism has been investigated.[194,272,274] They tend to show some irreversible character with expansion and A^+ remaining in the structure after charging. Still, they show relatively fast kinetics and long cycle-lifetimes at high rates.[273,275] For SIBs, soft carbons can potentially present higher capacities than graphite while taking advantage of some of the aspects of hard carbons. Our knowledge on the potential for soft carbons remains limited due to the much fewer studies compared with hard carbons and graphite. Perhaps, we will see some exciting materials being developed in the near future toward SIBs and PIBs.

Yet other carbon allotropes include a wide variety of nanoscale and thin layered structures such as graphene.[276] Such graphene materials show higher Li^+ storage capacity than graphite,[277] and upon doping they can show promising results for Na^+ and K^+ storage.[278,279]

6. Alloy materials

As discussed in the previous section, carbon-based negative electrode materials provide the capacity to store A^+ in the

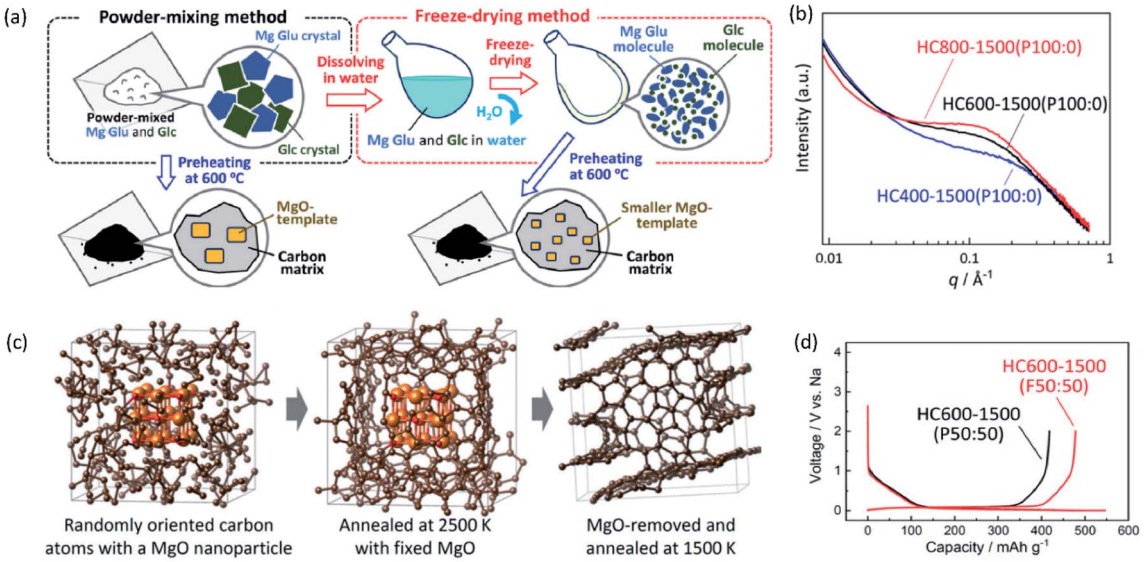

Fig. 20 Improving the pore structure in hard carbons through template-synthesis. (a) Schematic of the preparation methods for template-based synthesis for hard carbons. (b) Small-angle X-ray scattering of magnesium gluconate-based hard carbons prepared with different preheating temperatures; 400 °C (blue), 600 °C (black) and 800 °C (red). (c) First-principles molecular dynamic calculations of MgO/carbon composite structures and MgO-removed. Brown, orange, and red spheres represent carbon, magnesium, and oxygen atoms, respectively. (d) Charge–discharge profile for hard carbons prepared with 50 : 50 molar ratio (Mg Glu : Mg Glc) for powder mixing (P) or freeze–drying (F) methods with preheating at 600 °C, acid treatment, and post-heating at 1500 °C. (a)–(d) are reprinted with permission from ref. 264. Copyright 2021 John Wiley and Sons.

interlayers or nanopores of the carbon structure. In this section, we introduce active materials that can store A^+ *via* alloying reactions. In LIBs, Si[280] forms metastable crystalline phases such as $Li_{12}Si_7$, $Li_{14}Si_6$, $Li_{13}Si_4$, $Li_{15}Si_4$, and $Li_{22}Si_5$.[281] Hereafter, electrochemical lithium insertion into Si forming these silicides, which are compounds correctly, not alloys, is regarded as an alloying reaction for simplicity. When the metastable phases are formed, the alloying reaction proceeds *via* complex combination of amorphization and recrystallization.[282] Since the study of the electrochemical performance of various alloy materials and alloying mechanisms has been exhaustively explained in the literature,[280,283–289] we will focus our discussion on the most promising alloy materials in SIBs and PIBs.

One of the advantages of alloy materials is delivering extremely high capacity due to their superior ability to accommodate multiple A atoms in the matrix structure compared to topotactic insertion materials[290] as shown in Fig. 21[4,221,291–297] where the theoretical gravimetric and volumetric capacities of alloy materials in Li, Na, and K systems are compared.

With reference to the gravimetric capacity (Fig. 21a), Si is known to be the most promising alloy material for LIBs owing to its high gravimetric capacity (4200 mA h g^{-1} for $Li_{4.4}Si$ and 3580 mA h g^{-1} for $Li_{3.75}Si$).[280] NaSi and KSi are recognized as the most alkali metal-rich silicide phases in Na and K systems, respectively, being expected to deliver 954 mA h g^{-1}.[298] However, to the best of our knowledge, the electrochemical formation of NaSi and KSi in the SIB and PIB has not hitherto been reported.[4] Similar to Si, other group-14 elements (Ge, Sn, and Pb) are known to form 1 : 1 alloys with alkali metals. Although the reaction mechanism and final discharge products were different among various alloys, the corresponding theoretical capacities for Na^+ and K^+ are generally lower than those for Li^+ due to the increased weight of the alkali metal (Li < Na < K).[298] However, it is worth noting that the Na–Sn alloy shows lower reaction voltage compared with the Li–Sn case, which could increase the energy density of SIBs when used as a negative electrode.[299] While Na-rich $Na_{15}Sn_4$ formation (847 mA h g^{-1}) was reported in the Na cell, only KSn formation (226 mA h g^{-1}) was confirmed in K cells.[300] Regarding group-15 elements (P, Sb, and Bi), alkali metal-rich phases are formed, for example, Li_3P and Na_3P (2597 mA h g^{-1}), Li_3Sb, Na_3Sb and K_3Sb (660 mA h g^{-1}), and Li_3Bi, Na_3Bi, and K_3Bi (385 mA h g^{-1}).[4] For phosphorus based alloys, alkali metal rich Li_3P and Na_3P can be formed in Li and Na cells, however, only KP[301] or K_4P_3 [302] can be formed in the K cell, where the detailed reaction mechanism for K_xP formation is still unclear.

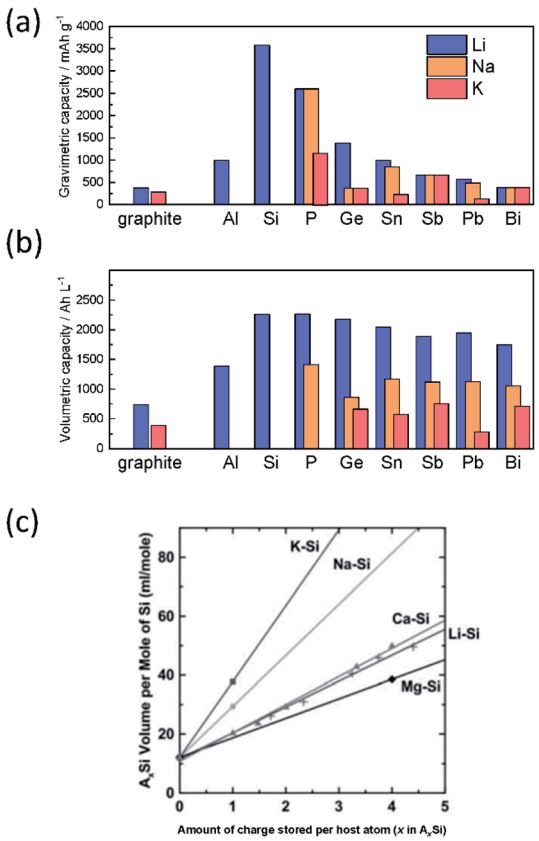

Fig. 21 Theoretical (a) gravimetric and (b) volumetric capacities of selected alloy materials for LIBs, SIBs, and PIBs. The volumetric capacities were calculated at the fully charged state. (a) and (b) are adopted with permission from ref. 4. Copyright 2020 American Chemical Society. (c) Volume of A_xSi per mole of Si plotted as a function of the charge stored. Reproduced with permission from ref. 303. Copyright IOP Publishing.

In addition to the gravimetric capacity, volumetric capacity is an important factor, and it should be discussed with respect to the volume at the fully charged state. Fig. 21b shows the volumetric capacities calculated based on the expanded volume.[4,303] In general, the molar volume of K in K compounds tends to be higher because of the larger ionic radius of K^+ than that of Na^+ and Li^+. Therefore, the volumetric capacity of K-alloy materials is lower than that of Li-and Na-alloy materials. For example, Sb shows the same theoretical gravimetric capacity in Li, Na, and K cells, but their volumetric capacities calculated with fully alloying volume are 1890, 1120, and 760 A h L^{-1} in the Li, Na, and K cells, respectively.

Not only the higher capacity but also relatively low reaction potential of alloy materials is beneficial for negative electrode materials, leading to the increase in the cell voltage and eventually increasing the energy density of the cell. However, the electrode suffers from a large volume change during charge and discharge. As a result, the alloy-based electrode is physically pulverized through repeated volume expansion/shrinkage during cycling.[304,305] The interfacial resistance between the electrode and the electrolyte continuously increases due to the repetitive decomposition reaction of the electrolyte on the newly formed charged alloy surface in every charge cycle. Fig. 21c shows the volume expansion of the alkali metal-Si alloys as a function of the alkali metal content.[298] The volumes of the materials increase monotonically with increasing alkali metal content, and the volume expansion increases in the order of Li < Na < K. This large volume change destroys the electrode structure and triggers side reactions such as continuous decomposition of the electrolyte, leading to a decrease in capacity, accompanied by electrical isolation of active materials.

To reduce the detrimental effects of volume expansion, core–shell[306–308] or thin platelets materials,[309] highly elastic

binders,[310–315] and nanosized particulates[316] are used, when employing alloy-based materials. Particularly, nanoparticles are widely used to prevent degradation of the electrode structure during battery cycling.[280,317,318] It is well known that the use of nanosized Si for LIBs enables the suppression of pulverization by continuous volume change.[280,315,319–321] However, nanoparticles are industrially expensive and a hazard to health, requiring complicated preparation methods. In addition, the use of nanoparticles cannot completely suppress the continuous electrolyte decomposition on the surface of the active materials because a new surface is still formed in every cycle through repetitive expansion/shrinkage.[304] The formation of the new surface cannot be prevented by solely modifying the active material architecture. To control the continuous growth of the surface decomposition layer, two methods have been investigated: (i) the use of functional binders to coat the active material surface and form a passivation layer;[219,315,322–324] and (ii) design of the electrolyte with appropriate solvents, salts, and additives to control the decomposition reaction of the electrolyte.[304,325–329] The surface reaction of the active material is strongly affected by the components of the electrolyte. As shown in Fig. 22, the cycling performance is significantly affected by the electrolyte components, such as salts and organic solvents.[304] With regard to the Na–Bi alloy system, the PF_6^- anion shows superior capacity retention compared with that of ClO_4^- and $CF_3SO_3^-$ (TfO^-) anions (Fig. 22a). Additionally, the ether-based solvent shows higher retention than the carbonate ester solvent (Fig. 22b). Similar behavior can be observed in the K–Bi alloy system as shown in Fig. 22c and d, where the ether-based electrolyte shows superior capacity retention compared with carbonate solvents. This is because continuous electrolyte decomposition occurs on the new surface formed in every charging cycle, and pulverization of the macroparticles occurs due to volume expansion, as shown in Fig. 22e. Therefore, a major challenge lies in passivating the repeatedly exposed new surface by using a functional binder or additive, or by appropriate electrolyte design, in order to use an alloy-based anode with extremely high reversible capacity.

7. Interphases on positive and negative electrodes

As highlighted in the sections of negative electrode materials, interphases between the electrode and the electrolyte significantly impact battery performance.[330–332] The interphases represent highly complex, multiphase structures that control

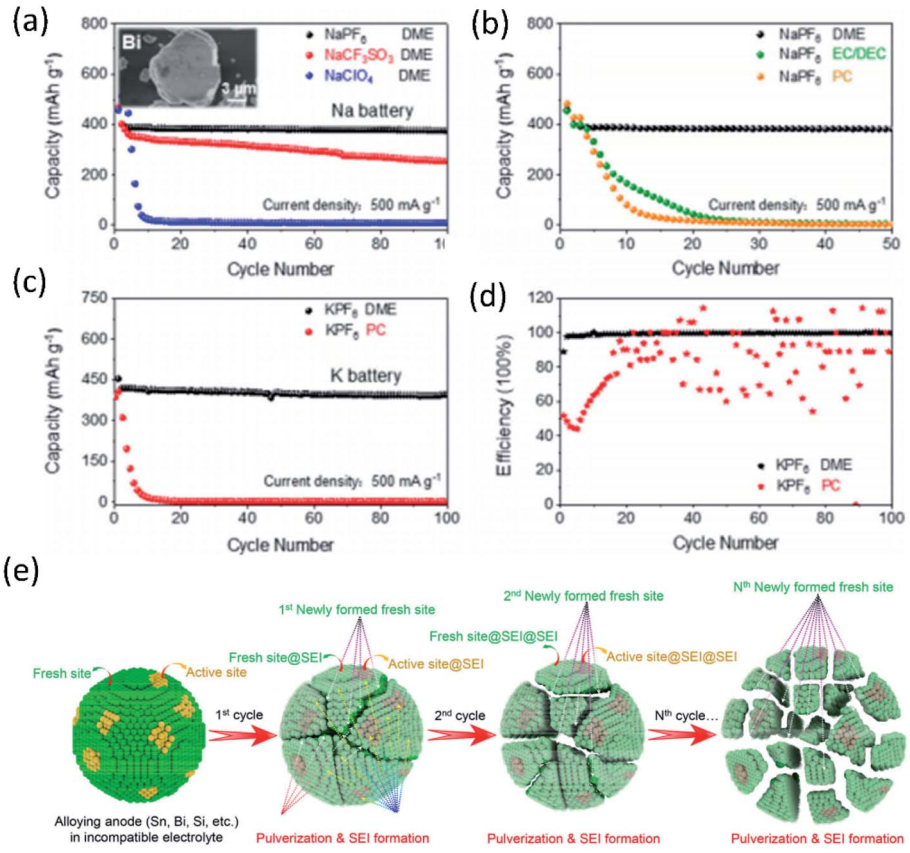

Fig. 22 Comparative performance of alloy materials in Na cells filled with different electrolytes. Cycling performance of Bi in (a) 1.0 M $NaPF_6$, $NaCF_3SO_3$ or $NaClO_4$ in DME and in (b) 1.0 M $NaPF_6$ in DME, EC/DEC, or PC, respectively. Inset in the panel (a) is the SEM images of the microsized Bi particles. (c) Cycling performance and (d) coulombic efficiency of Bi in K cells filled with 1.0 M KPF_6, in DME or PC. (e) Alloying reaction model: behaviors of alloying electrode materials in the incompatible electrolyte upon cycling (a–e) are reprinted with permission from ref. 304. Copyright 2020 American Chemical Society.

the flux of A^+ carrier ions to and from the electrolyte before A^+ ions interact with the electrodes' bulk structure.[332–334] As such, these structures directly influence the rate performance of batteries and improving their chemistry is essential for attaining higher rates. Further, the formation of interphase structures, especially at the negative electrode, is crucial for attaining high voltage batteries.[332,335] Only a few studies reported electrolytes that showed no apparent SEI formation and instead likely involved solvent co-intercalation.[336] In general, the lack of an interphase on the negative electrode leads to continuous electrolyte degradation during charging and would not effectively store energy.

Though the SEI has been extensively studied within LIBs, interphase chemistry is also a well-known phenomenon in high-voltage SIBs and PIBs.[337,338] However, compared with our knowledge on the properties of bulk electrodes, these interphases are much less understood due to their thin and complex composition, fluctuation across the lifetime of the battery, heterogeneity across the electrode surfaces,[339] and strong dependence on the electrolyte composition.[332,335,340,341] Because of their multi-phase and dynamic nature, it becomes essential to conduct *in situ* or *operando* analyses.[342,343] Through various materials characterization techniques, understanding of the SEI components,[344,345] their reactivity and formation,[346,347] and their A^+ content and transfer properties are being revealed.[348–350]

To date, most research has focused on better comprehending the behavior of the SEI that occurs at negative electrodes. The SEI forms when electrons at the negative electrode surface meet and reduce electrolyte species, solvent molecules, or electrolyte additives in a cascade of complex reactions.[351–353] These reactions heavily depend on the content of the electrolyte, electrochemical conditions, electrode surface, temperature, and so on. In the electrolyte, the cations can coordinate with the solvent molecules or anions (depending on electrolyte concentration),[354,355] and this can result in changes in thermodynamics and oxidation/reduction stability.[356,357] Generally, most of this chemistry occurs during initial cycles and results in the nanoscale film with a compact inorganic layer, consisting mainly of metal fluorides, oxides and carbonates, and a mostly organic, outer layer of more alkyl carbonates, semicarbonates, and polymers.[332,353] However, the thickness of this interphase can change with cycling and is heavily dependent on the electrolyte.[341] Further, concentrated electrolytes tend to show interphases that are anion-derived producing predominantly inorganic passivating structures.[358,359]

The SEI impacts battery performance in multiple ways including the initial capacity loss, self-discharge behavior, voltage efficiency, cycle life and safety. Since it is desirable to have low potentials for the negative electrodes to achieve a high voltage for the battery, this generally always leads to interface chemistry that occurs during the initial charging of the battery; that is an irreversible component. In the case of graphite and other uncharged electrodes, this leads to consumption of some of the positive electrode material capacity and some of the electrolyte content. Therefore, having a large irreversible loss during the first charging step is undesirable since it would require an additional positive active material and less efficient utilization. The electrolyte components and additives can have a significant impact on this first cycle coulombic efficiency and subsequent cycle life.[340,360,361] Metals and other negative electrode in their charged state can continue to react with the electrolyte if not effectively covered with an SEI, leading to undesirable self-discharge, further electrolyte consumption and a decrease in coulombic efficiency.[341,353] Lastly, the SEI directly impacts plating reactions and potential for dendrite formation; therefore, it can play an important role in maintaining battery safety in developing metal and air batteries.[362–365]

While significant work has been done regarding Li^+ (Li-SEI), only a limited number of papers have focused on the interphases that occur in SIBs and PIBs with most focusing on characterization of the SEI composition, morphology and structure. As with other components of the electrolyte, the kind and concentration of A^+ ions impact the reduction stability of the electrolyte and the SEI formation. The Li-SEI tends to show stable SEI components with greater polymerization and cross-linking, while Na-SEI components tend to show poorer stability and higher solubility.[366,367] In addition, the K-SEI can show incomplete coverage leading to higher likelihood of plating.[368] A comparison of the SEI on hard carbons conducted by our group indicates that 1 M Li^+, Na^+ and K^+ (bis(fluorosulfonyl)imide) (FSI^-) electrolytes show differences in initial reversible capacity/coulombic efficiency and structural compositions based on XPS and time-of-flight secondary ion mass spectrometry (TOF-SIMS) analyses.[4] Specifically, these results show that the overall organic and inorganic contents in the Li and K cells are more significant than the Na cell, suggesting a thinner Na-SEI in agreement with other studies.[367] The K-SEI shows unique anion-derived chemical components and a relatively small amount of KF,[4] strongly contrasting with LiF which is thought to play a key role in Li-SEI function.[369] In terms of distribution across the SEI, TOF-SIMS further indicates that only the Li-SEI shows organic and inorganic content at the outer layer of the SEI, while the Na and K cells show mainly inorganic components.[4] Interestingly, utilizing a preformed Li-SEI for applications in a K electrolyte has shown improved cycling, further emphasizing differences in the properties of the formed SEI.[368] Altogether these results suggest different formation mechanisms, structures and stabilities for the Li-, Na-, and K-SEI with dramatically diverse results even when using analogous electrolytes.

In terms of performance, symmetrical cells and impedance measurements show that the equivalent Na- and K-SEIs display poorer ionic conductivity compared with Li, leading to polarization even at low current densities.[370] Localized measurements further indicate higher Li^+ uptake during SEI formation and more rapid passivation.[371] This likely derives from not only the overall interphase structure, but the individual components which can show different properties. For example, theoretical studies have indicated significant differences in ion-transfer capabilities of NaF compared with LiF while metal carbonates and oxides can attain faster ion-transfer rates.[372] Likewise, the observed stability of the SEI toward dissolution also derives from the individual components as solubility for Li, Na, and K salts is known to vary drastically and depends on the solvent. When considering practical batteries, research also shows that

the Li-SEI chemistry has greater stability toward extreme operating temperatures.[373] Understanding these individual components and their synergistic interactions remains quite complex, but is still an important goal toward obtaining high-performance batteries.[4,374]

In general, improving the interphase chemistry focuses on two main strategies: engineering of the electrolyte, through concentration and additive approaches, and artificial interphases, where a preformed structure is prepared before constructing a battery. Toward electrolyte engineering, vinylene carbonate (VC) and fluoroethylene carbonate (FEC) are two widely explored additives applied for improving LIBs.[375,376] In PIBs, FEC can show mixed effects toward the positive and negative electrodes[360,377] and at different additive concentrations.[378] Therefore, modifications cannot be easily generalized across different battery systems.[379] Still, the use of electrolyte additives can improve polarization, change the reaction products, and inhibit electrolyte degradation during cycling.[365,380] Another option is engineering of the interphase directly with the so-called artificial SEI[381,382] or alternatively through direct modification of the electrode structure that interacts with the forming SEI.[383,384] An artificial SEI generally refers to an interphase structure formed on the surface of the negative electrode through various means before cycling or assembly of the battery. Artificial SEIs have been widely explored for Li and Na metals including the use of Al_2O_3, graphene, carbon nanotubes, and polymers, to list a few.[381,382] Comparatively, less work has focused on highly reactive K metal anodes.[380,385] Due to their highly reducing potentials, artificial SEIs can be electrochemically prepared on such alkali metal electrodes under spontaneous conditions.[385,386] Harnessing this chemistry could lead to interesting interphase properties before the electrodes make contact with the electrolyte. It seems that both additive and interphase engineering can provide benefits toward battery performance and safety, thus determining optimal conditions from both could be very useful for future battery concepts.

Though they have received much less attention, the CEI structure and processes may also play an important role in battery stability and achieving high voltage batteries as decomposition of the electrolyte at LIB cathodes is a well-known occurrence.[387,388] Recently, Scipioni *et al.* used atom probe tomography to examine the CEI layers on $LiMn_2O_4$. Their results indicated a mixed nanometer-thick, layered-mosaic structure consisting of an inner layer of Mn_xO_y and MnF_x and an outer network made of LiF, Li_2O and organic components, *e.g.* polycarbonates.[330] Likewise, interfacial chemistry involving Co atoms was revealed on $LiCoO_2$ showing some link to electrocatalytic behavior of the transition metal oxide and battery degradation,[389] and other reports have indicated that the CEI can continuously grow with cycling, storage time and temperature.[387] CEI chemistry is also known to occur on cathode materials for SIBs[92,390] and PIBs,[391] though significantly less knowledge has been acquired on these structures. Much remains unknown about the prevalence of the CEI or its importance in SIB and PIB operations, but future studies will reveal further details for achieving better performance.

8. Conclusions

We have reviewed promising positive (layered oxides, polyanion materials, and PBAs) and negative electrode (graphitic carbon, hard carbon, soft carbon, and alloy) materials for SIBs and PIBs, focusing on the crystal structure and interfacial phenomena.

Characteristics of Na^+ provide a large variety of structure types and the appropriate selection of substitutional elements in transition metal layers enables not only the enhancement of electrochemical performance but also activates oxygen redox in the case of layered oxides. As a result, layered oxides are in leading positions for positive electrode materials in SIBs. In contrast, layered oxides with larger K^+ often suffer from structural instability with consecutive phase transitions and deliver inferior capacity in PIBs. Cation permutation either in the transition or alkali metal layers is one of the strategies to overcome those disadvantages. Alternatively, polyanion materials and PBAs are favorable choices since the 3D framework structure provides decent channels and interstitial sites for large K^+ diffusion and insertion/extraction, respectively. In addition, high working voltage driven by tuning the covalency of M–O bonds is one of the advantages for open-framework materials for both SIBs and PIBs.

With reference to negative electrode materials, Na^+ and K^+ show distinctive features with graphite, the most commonly used carbon-based electrode material in LIBs. In the case of Na^+, the unfavorable thermodynamic interaction with the graphite results in no stable intercalation compounds. In contrast, graphite is promising for PIBs although the number of intercalated K^+ ions is lower than that of Li^+. Using co-intercalating solvent molecules also enables the formation of stable intercalation compounds for both Na^+ and K^+. This further opens possibilities for graphite application even for SIBs.

Hard carbons are the most promising for SIBs and meet the philosophy of SIBs: environmentally friendly preparation methods and low-cost sources. Depending on the synthetic conditions of hard carbons including precursors, temperatures, and templates, their structure is rather complex and diverse. This simultaneously necessitates the incorporation of multiple mechanisms to elucidate observed electrochemical behaviors.

Alloy materials are attractive due to their superior gravimetric and volumetric capacities. However, the volume change during charge/discharge produces mechanical stress, rapidly leading to the electrochemical pulverization of active materials. In addition, new portions of metal surface are exposed to the electrolyte at each charge, which promotes continuous electrolyte degradation and impedes stabilization of the SEI. Two promising methods to overcome the issues related to the volume change include the use of functional binders and the design of appropriate electrolytes.

Those strategies spontaneously stress the importance of comprehending the exclusive SEI features observed in SIBs and PIBs, *e.g.* unstable and soluble SEI components in the electrolyte and poor ionic conductivity. Since the SEI formation mechanism highly depends on the electrolyte such as its

concentration and composition, the design of the electrolyte formulation is critical. Moreover, *in situ*/*operando* characterization is much preferred to understand the SEI properties, but these measurements under realistic conditions are still challenging. Few studies have been carried out for the CEI although a stable CEI would expand the selection of transition metal as well as the use of oxygen redox for positive electrode materials. As the lower Lewis acidity of Na^+ and K^+ might allow fast ionic diffusion in the electrolyte and the interphase, comprehensive studies on the SEI and CEI would further shed insights on the rate capability for SIBs and PIBs.

A global push to reduce fossil fuel reliance will create a massive market for energy storage. For stationary applications where cost, safety, ease of maintenance, reliability, and lifetime are more important than size and weight, SIBs can be competitive against LIBs in the near term based on their current state of development. The practical application of PIBs necessities further improvement of their electrochemical performance and decent safety strategies. However, as evidenced by recent intensive studies on PIBs, PIBs are also promising next generation battery candidates. From a scientific point of view, research on the development of SIBs and PIBs should be approached in a multidisciplinary way to understand rather complex phenomena involved in electrode materials, electrolytes, electrolyte additives, and functional binders.

Author contributions

The manuscript was written through contributions of all authors. All authors have given approval to the final version of the manuscript.

Conflicts of interest

There are no conflicts to declare.

Acknowledgements

This study was partly funded by the MEXT program "ESICB" (Grant No. JPMXP0112101003), the JST through A-STEP program (Grant No. JPMJTS1611), the CONCERT-Japan program, CREST (Grant No. JPMJCR21O6), NEDO (JPNP20004), and JSPS KAKENHI (Grant No. JP20H02849, JP20K05690, JP21K14724, and JP21K20561). Schematic illustrations of the crystal structures were drawn using the program VESTA.[392]

References

1 R. Schmuch, R. Wagner, G. Hörpel, T. Placke and M. Winter, *Nat. Energy*, 2018, **3**, 267–278.
2 C. Vaalma, D. Buchholz, M. Weil and S. Passerini, *Nat. Rev. Mater.*, 2018, **3**, 1–11.
3 E. A. Olivetti, G. Ceder, G. G. Gaustad and X. Fu, *Joule*, 2017, **1**, 229–243.
4 T. Hosaka, K. Kubota, A. S. Hameed and S. Komaba, *Chem. Rev.*, 2020, **120**, 6358–6466.
5 S. Komaba, *Electrochemistry*, 2019, 19-16-E2677.
6 S. Komaba, *Chem. Lett.*, 2020, **49**, 1507–1516.
7 K. Kubota, M. Dahbi, T. Hosaka, S. Kumakura and S. Komaba, *Chem. Rec.*, 2018, **18**, 459–479.
8 N. Yabuuchi, K. Kubota, M. Dahbi and S. Komaba, *Chem. Rev.*, 2014, **114**, 11636–11682.
9 K. Kubota, *Electrochemistry*, 2020, **88**, 507–514.
10 J.-Y. Hwang, S.-T. Myung and Y.-K. Sun, *Chem. Soc. Rev.*, 2017, **46**, 3529–3614.
11 J. Y. Hwang, S. T. Myung and Y. K. Sun, *Adv. Funct. Mater.*, 2018, **28**, 1802938.
12 H. Kim, J. C. Kim, M. Bianchini, D. H. Seo, J. Rodriguez-Garcia and G. Ceder, *Adv. Energy Mater.*, 2018, **8**, 1702384.
13 G. G. Eshetu, G. A. Elia, M. Armand, M. Forsyth, S. Komaba, T. Rojo and S. Passerini, *Adv. Energy Mater.*, 2020, **10**, 2000093.
14 R. D. Shannon, *Acta Crystallogr., Sect. A: Cryst. Phys., Diffr., Theor. Gen. Crystallogr.*, 1976, **32**, 751–767.
15 Y. Matsuda, H. Nakashima, M. Morita and Y. Takasu, *J. Electrochem. Soc.*, 1981, **128**, 2552.
16 M. Okoshi, Y. Yamada, S. Komaba, A. Yamada and H. Nakai, *J. Electrochem. Soc.*, 2016, **164**, A54.
17 F. Sagane, T. Abe, Y. Iriyama and Z. Ogumi, *J. Power Sources*, 2005, **146**, 749–752.
18 Y. Yamada, Y. Iriyama, T. Abe and Z. Ogumi, *Langmuir*, 2009, **25**, 12766–12770.
19 F. Sagane, T. Abe and Z. Ogumi, *J. Phys. Chem. C*, 2009, **113**, 20135–20138.
20 Y. Marcus, *Pure Appl. Chem.*, 1985, **57**, 1129–1132.
21 S. Komaba, T. Hasegawa, M. Dahbi and K. Kubota, *Electrochem. Commun.*, 2015, **60**, 172–175.
22 T. Hosaka, S. Muratsubaki, K. Kubota, H. Onuma and S. Komaba, *J. Phys. Chem. Lett.*, 2019, **10**, 3296–3300.
23 A. Rudola, C. J. Wright and J. Barker, *Energy Mater. Adv.*, 2021, 1–12.
24 A. Rudola, A. J. Rennie, R. Heap, S. S. Meysami, A. Lowbridge, F. Mazzali, R. Sayers, C. J. Wright and J. Barker, *J. Mater. Chem. A*, 2021, **9**, 8279–8302.
25 N. Tapia-Ruiz, A. R. Armstrong, H. Alptekin, M. A. Amores, H. Au, J. Barker, R. Boston, W. R. Brant, J. M. Brittain and Y. Chen, *J. Phys.: Energy*, 2021, **3**, 031503.
26 Z. Guo, J. Zhu, J. Feng and S. Du, *RSC Adv.*, 2015, **5**, 69514–69521.
27 B. Song, I. Dhiman, J. C. Carothers, G. M. Veith, J. Liu, H. Z. Bilheux and A. Huq, *ACS Energy Lett.*, 2019, **4**, 2402–2408.
28 W. Lu, C. M. López, N. Liu, J. T. Vaughey and A. Jansen, *J. Electrochem. Soc.*, 2012, **159**, A566.
29 N. Xiao, W. D. McCulloch and Y. Wu, *J. Am. Chem. Soc.*, 2017, **139**, 9475–9478.
30 H. Kondou, J. Kim and H. Watanabe, *Electrochemistry*, 2017, **85**, 647–649.
31 C. Delmas, C. Fouassier and P. Hagenmuller, *Physica B+C*, 1980, **99**, 81–85.
32 R. Kanno, T. Shirane, Y. Inaba and Y. Kawamoto, *J. Power Sources*, 1997, **68**, 145–152.

33 T. Shirane, R. Kanno, Y. Kawamoto, Y. Takeda, M. Takano, T. Kamiyama and F. Izumi, *Solid State Ionics*, 1995, **79**, 227–233.
34 L. Hoffmann and R. Hoppe, *Z. Anorg. Allg. Chem.*, 1977, **430**, 115–120.
35 J.-P. Parant, R. Olazcuaga, M. Devalette, C. Fouassier and P. Hagenmuller, *J. Solid State Chem.*, 1971, **3**, 1–11.
36 E. Chappel, M. Nunez-Regueiro, G. Chouteau, O. Isnard and C. Darie, *Eur. Phys. J. B*, 2000, **17**, 615–622.
37 C. Delmas, J.-J. Braconnier, C. Fouassier and P. Hagenmuller, *Solid State Ionics*, 1981, **3**, 165–169.
38 N. Yabuuchi, M. Kajiyama, J. Iwatate, H. Nishikawa, S. Hitomi, R. Okuyama, R. Usui, Y. Yamada and S. Komaba, *Nat. Mater.*, 2012, **11**, 512–517.
39 Z. Lu and J. Dahn, *J. Electrochem. Soc.*, 2001, **148**, A1225.
40 J. B. Goodenough, K. Mizushima and T. Takeda, *Jpn. J. Appl. Phys.*, 1980, **19**, 305.
41 R. Berthelot, D. Carlier and C. Delmas, *Nat. Mater.*, 2011, **10**, 74–80.
42 J. L. Kaufman and A. Van der Ven, *Phys. Rev. Mater.*, 2019, **3**, 015402.
43 M. Y. Toriyama, J. L. Kaufman and A. Van der Ven, *ACS Appl. Energy Mater.*, 2019, **2**, 2629–2636.
44 Y. Hironaka, K. Kubota and S. Komaba, *Chem. Commun.*, 2017, **53**, 3693–3696.
45 Y. Lei, X. Li, L. Liu and G. Ceder, *Chem. Mater.*, 2014, **26**, 5288–5296.
46 H. Kim, D.-H. Seo, A. Urban, J. Lee, D.-H. Kwon, S.-H. Bo, T. Shi, J. K. Papp, B. D. McCloskey and G. Ceder, *Chem. Mater.*, 2018, **30**, 6532–6539.
47 S. Komaba, C. Takei, T. Nakayama, A. Ogata and N. Yabuuchi, *Electrochem. Commun.*, 2010, **12**, 355–358.
48 Y. Lyu, L. Ben, Y. Sun, D. Tang, K. Xu, L. Gu, R. Xiao, H. Li, L. Chen and X. Huang, *J. Power Sources*, 2015, **273**, 1218–1225.
49 S. Komaba, T. Nakayama, A. Ogata, T. Shimizu, C. Takei, S. Takada, A. Hokura and I. Nakai, *ECS Trans.*, 2009, **16**, 43.
50 Y.-N. Zhou, J.-J. Ding, K.-W. Nam, X. Yu, S.-M. Bak, E. Hu, J. Liu, J. Bai, H. Li and Z.-W. Fu, *J. Mater. Chem. A*, 2013, **1**, 11130–11134.
51 K. Kubota, I. Ikeuchi, T. Nakayama, C. Takei, N. Yabuuchi, H. Shiiba, M. Nakayama and S. Komaba, *J. Phys. Chem. C*, 2015, **119**, 166–175.
52 N. Yabuuchi, I. Ikeuchi, K. Kubota and S. Komaba, *ACS Appl. Mater. Interfaces*, 2016, **8**, 32292–32299.
53 A. Mendiboure, H. Eickenbusch, R. Schöllhorn and G. S. Rao, *J. Solid State Chem.*, 1987, **71**, 19–28.
54 D. Mikhailova, O. M. Karakulina, D. Batuk, J. Hadermann, A. M. Abakumov, M. Herklotz, A. A. Tsirlin, S. Oswald, L. Giebeler and M. Schmidt, *Inorg. Chem.*, 2016, **55**, 7079–7089.
55 L. Verger, M. Guignard and C. Delmas, *Inorg. Chem.*, 2019, **58**, 2543–2549.
56 Z. Lu and J. Dahn, *Chem. Mater.*, 2001, **13**, 1252–1257.
57 T. Masese, K. Yoshii, Y. Yamaguchi, T. Okumura, Z.-D. Huang, M. Kato, K. Kubota, J. Furutani, Y. Orikasa and H. Senoh, *Nat. Commun.*, 2018, **9**, 1–12.
58 M. Zhang, D. A. Kitchaev, Z. Lebens-Higgins, J. Vinckeviciute, M. Zuba, P. J. Reeves, C. P. Grey, M. S. Whittingham, L. F. Piper and A. Van der Ven, *Nat. Rev. Mater.*, 2022, 1–19.
59 D.-H. Seo, J. Lee, A. Urban, R. Malik, S. Kang and G. Ceder, *Nat. Chem.*, 2016, **8**, 692–697.
60 U. Maitra, R. A. House, J. W. Somerville, N. Tapia-Ruiz, J. G. Lozano, N. Guerrini, R. Hao, K. Luo, L. Jin and M. A. Pérez-Osorio, *Nat. Chem.*, 2018, **10**, 288–295.
61 B. M. De Boisse, G. Liu, J. Ma, S.-i. Nishimura, S.-C. Chung, H. Kiuchi, Y. Harada, J. Kikkawa, Y. Kobayashi and M. Okubo, *Nat. Commun.*, 2016, **7**, 1–9.
62 A. J. Perez, D. Batuk, M. Saubanère, G. Rousse, D. Foix, E. Mccalla, E. J. Berg, R. Dugas, K. HW van den Bos and M.-L. Doublet, *Chem. Mater.*, 2016, **28**, 8278–8288.
63 D. H. Lee, J. Xu and Y. S. Meng, *Phys. Chem. Chem. Phys.*, 2013, **15**, 3304–3312.
64 K. Dai, J. Mao, Z. Zhuo, Y. Feng, W. Mao, G. Ai, F. Pan, G. Liu and W. Yang, *Nano Energy*, 2020, **74**, 104831.
65 Y. Zhang, M. Wu, J. Ma, G. Wei, Y. Ling, R. Zhang and Y. Huang, *ACS Cent. Sci.*, 2020, **6**, 232–240.
66 C. Cheng, S. Li, T. Liu, Y. Xia, L.-Y. Chang, Y. Yan, M. Ding, Y. Hu, J. Wu and J. Guo, *ACS Appl. Mater. Interfaces*, 2019, **11**, 41304–41312.
67 R. A. House, U. Maitra, L. Jin, J. G. Lozano, J. W. Somerville, N. H. Rees, A. J. Naylor, L. C. Duda, F. Massel, A. V. Chadwick, S. Ramos, D. M. Pickup, D. E. McNally, X. Lu, T. Schmitt, M. R. Robers and P. G. Bruce, *Chem. Mater.*, 2019, **31**, 3293–3300.
68 K. Dai, J. Wu, Z. Zhuo, Q. Li, S. Sallis, J. Mao, G. Ai, C. Sun, Z. Li and W. E. Gent, *Joule*, 2019, **3**, 518–541.
69 Q. Wang, S. Mariyappan, G. Rousse, A. V. Morozov, B. Porcheron, R. Dedryvère, J. Wu, W. Yang, L. Zhang and M. Chakir, *Nat. Mater.*, 2021, **20**, 353–361.
70 B. M. de Boisse, M. Reynaud, J. Ma, J. Kikkawa, S.-i. Nishimura, M. Casas-Cabanas, C. Delmas, M. Okubo and A. Yamada, *Nat. Commun.*, 2019, **10**, 1–7.
71 J. Hong, W. E. Gent, P. Xiao, K. Lim, D.-H. Seo, J. Wu, P. M. Csernica, C. J. Takacs, D. Nordlund and C.-J. Sun, *Nat. Mater.*, 2019, **18**, 256–265.
72 W. E. Gent, K. Lim, Y. Liang, Q. Li, T. Barnes, S.-J. Ahn, K. H. Stone, M. McIntire, J. Hong and J. H. Song, *Nat. Commun.*, 2017, **8**, 1–12.
73 R. A. House, U. Maitra, M. A. Perez-Osorio, J. G. Lozano, L. Jin, J. W. Somerville, L. C. Duda, A. Nag, A. Walters and K.-J. Zhou, *Nature*, 2020, **577**, 502–508.
74 K. Du, J. Zhu, G. Hu, H. Gao, Y. Li and J. B. Goodenough, *Energy Environ. Sci.*, 2016, **9**, 2575–2577.
75 X. Rong, J. Liu, E. Hu, Y. Liu, Y. Wang, J. Wu, X. Yu, K. Page, Y.-S. Hu and W. Yang, *Joule*, 2018, **2**, 125–140.
76 E. J. Kim, P. A. Maughan, E. N. Bassey, R. J. Clément, L. A. Ma, L. C. Duda, D. Sehrawat, R. Younesi, N. Sharma, C. P. Grey and A. R. Armstong, *Adv. Energy Mater.*, 2021, 2102325.
77 M. Ben Yahia, J. Vergnet, M. Saubanère and M.-L. Doublet, *Nat. Mater.*, 2019, **18**, 496–502.

78 R. A. House, G. J. Rees, M. A. Pérez-Osorio, J.-J. Marie, E. Boivin, A. W. Robertson, A. Nag, M. Garcia-Fernandez, K.-J. Zhou and P. G. Bruce, *Nat. Energy*, 2020, **5**, 777–785.
79 E. McCalla, A. M. Abakumov, M. Saubanère, D. Foix, E. J. Berg, G. Rousse, M.-L. Doublet, D. Gonbeau, P. Novák and G. Van Tendeloo, *Science*, 2015, **350**, 1516–1521.
80 Y. Yoda, K. Kubota, H. Isozumi, T. Horiba and S. Komaba, *ACS Appl. Mater. Interfaces*, 2018, **10**, 10986–10997.
81 J. Xu, D. H. Lee, R. l. J. Clément, X. Yu, M. Leskes, A. J. Pell, G. Pintacuda, X.-Q. Yang, C. P. Grey and Y. S. Meng, *Chem. Mater.*, 2014, **26**, 1260–1269.
82 G. Singh, N. Tapia-Ruiz, J. M. Lopez del Amo, U. Maitra, J. W. Somerville, A. R. Armstrong, J. Martinez de Ilarduya, T. Rojo and P. G. Bruce, *Chem. Mater.*, 2016, **28**, 5087–5094.
83 N. Tapia-Ruiz, W. M. Dose, N. Sharma, H. Chen, J. Heath, J. W. Somerville, U. Maitra, M. S. Islam and P. G. Bruce, *Energy Environ. Sci.*, 2018, **11**, 1470–1479.
84 H. Yoshida, N. Yabuuchi, K. Kubota, I. Ikeuchi, A. Garsuch, M. Schulz-Dobrick and S. Komaba, *Chem. Commun.*, 2014, **50**, 3677–3680.
85 J. H. Jo, J. U. Choi, Y. J. Park, Y. H. Jung, D. Ahn, T. Y. Jeon, H. Kim, J. Kim and S. T. Myung, *Adv. Energy Mater.*, 2020, **10**, 1903605.
86 P.-F. Wang, H.-R. Yao, X.-Y. Liu, Y.-X. Yin, J.-N. Zhang, Y. Wen, X. Yu, L. Gu and Y.-G. Guo, *Sci. Adv.*, 2018, **4**, eaar6018.
87 J. U. Choi, J. Kim, J.-Y. Hwang, J. H. Jo, Y.-K. Sun and S.-T. Myung, *Nano Energy*, 2019, **61**, 284–294.
88 T. Deng, X. Fan, J. Chen, L. Chen, C. Luo, X. Zhou, J. Yang, S. Zheng and C. Wang, *Adv. Funct. Mater.*, 2018, **28**, 1800219.
89 X. Wang, X. Xu, C. Niu, J. Meng, M. Huang, X. Liu, Z. Liu and L. Mai, *Nano Lett.*, 2017, **17**, 544–550.
90 K. Kubota, S. Kumakura, Y. Yoda, K. Kuroki and S. Komaba, *Adv. Energy Mater.*, 2018, **8**, 1703415.
91 U.-H. Kim, S.-T. Myung, C. S. Yoon and Y.-K. Sun, *ACS Energy Lett.*, 2017, **2**, 1848–1854.
92 J. Alvarado, C. Ma, S. Wang, K. Nguyen, M. Kodur and Y. S. Meng, *ACS Appl. Mater. Interfaces*, 2017, **9**, 26518–26530.
93 A. Gutierrez, N. A. Benedek and A. Manthiram, *Chem. Mater.*, 2013, **25**, 4010–4016.
94 M. Ben Yahia, F. Lemoigno, G. Rousse, F. Boucher, J.-M. Tarascon and M.-L. Doublet, *Energy Environ. Sci.*, 2012, **5**, 9584–9594.
95 B. C. Melot, D. O. Scanlon, M. Reynaud, G. Rousse, J.-N. Chotard, M. Henry and J.-M. Tarascon, *ACS Appl. Mater. Interfaces*, 2014, **6**, 10832–10839.
96 P. Kubacek and R. Hoffmann, *J. Am. Chem. Soc.*, 1981, **103**, 4320–4332.
97 S. Adams, *J. Solid State Electrochem.*, 2010, **14**, 1787–1792.
98 K.-Y. Park, I. Park, H. Kim, H.-d. Lim, J. Hong, J. Kim and K. Kang, *Chem. Mater.*, 2014, **26**, 5345–5351.
99 C. A. J. Fisher, V. M. Hart Prieto and M. S. Islam, *Chem. Mater.*, 2008, **20**, 5907–5915.
100 T. V. S. L. Satyavani, A. Srinivas Kumar and P. S. V. Subba Rao, *Engineering Science and Technology, an International Journal*, 2016, **19**, 178–188.
101 R. Malik, D. Burch, M. Bazant and G. Ceder, *Nano Lett.*, 2010, **10**, 4123–4127.
102 C. Delacourt, L. Laffont, R. Bouchet, C. Wurm, J. B. Leriche, M. Morcrette, J. M. Tarascon and C. Masquelier, *J. Electrochem. Soc.*, 2005, **152**, A913.
103 L. F. J. Piper, N. F. Quackenbush, S. Sallis, D. O. Scanlon, G. W. Watson, K. W. Nam, X. Q. Yang, K. E. Smith, F. Omenya, N. A. Chernova and M. S. Whittingham, *J. Phys. Chem, C*, 2013, **117**, 10383–10396.
104 M.-y. Zheng, Z.-y. Bai, Y.-W. He, S. Wu, Y. Yang and Z.-Z. Zhu, *ACS Omega*, 2020, **5**, 5192–5201.
105 J. Kim, D.-H. Seo, H. Kim, I. Park, J.-K. Yoo, S.-K. Jung, Y.-U. Park, W. A. Goddard Iii and K. Kang, *Energy Environ. Sci.*, 2015, **8**, 540–545.
106 C. Berlanga, I. Monterrubio, M. Armand, T. Rojo, M. Galceran and M. Casas-Cabanas, *ACS Sustainable Chem. Eng.*, 2020, **8**, 725–730.
107 O. V. Yakubovich, W. Massa and O. V. Dimitrova, *Z. Anorg. Allg. Chem.*, 2005, **631**, 2445–2449.
108 I. Sultana, M. M. Rahman, S. Mateti, N. Sharma, S. Huang and Y. Chen, *Batteries Supercaps*, 2020, **3**, 450–455.
109 V. Mathew, S. Kim, J. Kang, J. Gim, J. Song, J. P. Baboo, W. Park, D. Ahn, J. Han, L. Gu, Y. Wang, Y.-S. Hu, Y.-K. Sun and J. Kim, *NPG Asia Mater.*, 2014, **6**, e138.
110 T. Hosaka, T. Shimamura, K. Kubota and S. Komaba, *Chem. Rec.*, 2019, **19**, 735–745.
111 J. B. Goodenough, H. Y. P. Hong and J. A. Kafalas, *Mater. Res. Bull.*, 1976, **11**, 203–220.
112 R. Rajagopalan, Z. Zhang, Y. Tang, C. Jia, X. Ji and H. Wang, *Energy Storage Materials*, 2021, **34**, 171–193.
113 C. Masquelier and L. Croguennec, *Chem. Rev.*, 2013, **113**, 6552–6591.
114 S. Patoux, C. Wurm, M. Morcrette, G. Rousse and C. Masquelier, *J. Power Sources*, 2003, **119–121**, 278–284.
115 S. C. Yin, H. Grondey, P. Strobel, M. Anne and L. F. Nazar, *J. Am. Chem. Soc.*, 2003, **125**, 10402–10411.
116 X. Zhang, X. Rui, D. Chen, H. Tan, D. Yang, S. Huang and Y. Yu, *Nanoscale*, 2019, **11**, 2556–2576.
117 X. Wang, C. Niu, J. Meng, P. Hu, X. Xu, X. Wei, L. Zhou, K. Zhao, W. Luo, M. Yan and L. Mai, *Adv. Energy Mater.*, 2015, **5**, 1500716.
118 J. Han, G.-N. Li, F. Liu, M. Wang, Y. Zhang, L. Hu, C. Dai and M. Xu, *Chem. Commun.*, 2017, **53**, 1805–1808.
119 L. Zhang, B. Zhang, C. Wang, Y. Dou, Q. Zhang, Y. Liu, H. Gao, M. Al-Mamun, W. K. Pang, Z. Guo, S. X. Dou and H. K. Liu, *Nano Energy*, 2019, **60**, 432–439.
120 C. Delmas, A. Nadiri and J. L. Soubeyroux, *Solid State Ionics*, 1988, **28–30**, 419–423.
121 S.-C. Chung, J. Ming, L. Lander, J. Lu and A. Yamada, *J. Mater. Chem. A*, 2018, **6**, 3919–3925.
122 S.-F. Li, X.-K. Hou, Z.-Y. Gu, Y.-F. Meng, C.-D. Zhao, H.-X. Zhang and X.-L. Wu, *New J. Chem.*, 2021, **45**, 4854–4859.

123 R. Essehli, A. Alkhateeb, A. Mahmoud, F. Boschini, H. Ben Yahia, R. Amin and I. Belharouak, *J. Power Sources*, 2020, **469**, 228417.
124 Y. Wu, Z. Cao, L. Song and J. Gao, *ACS Appl. Mater. Interfaces*, 2021, **13**, 48865–48871.
125 P. Ramesh Kumar, A. Kheireddine, U. Nisar, R. A. Shakoor, R. Essehli, R. Amin and I. Belharouak, *J. Power Sources*, 2019, **429**, 149–155.
126 U. Ahmadu, in *Advanced Sensor and Detection Materials*, 2014, pp. 265–308.
127 B. L. Ellis, T. N. Ramesh, W. N. Rowan-Weetaluktuk, D. H. Ryan and L. F. Nazar, *J. Mater. Chem.*, 2012, **22**, 4759–4766.
128 N. R. Khasanova, O. A. Drozhzhin, D. A. Storozhilova, C. Delmas and E. V. Antipov, *Chem. Mater.*, 2012, **24**, 4271–4273.
129 E. Boivin, J.-N. Chotard, T. Bamine, D. Carlier, P. Serras, V. Palomares, T. Rojo, A. Iadecola, L. Dupont, L. Bourgeois, F. Fauth, C. Masquelier and L. Croguennec, *J. Mater. Chem. A*, 2017, **5**, 25044–25055.
130 E. Boivin, J.-N. Chotard, M. Ménétrier, L. Bourgeois, T. Bamine, D. Carlier, F. Fauth, C. Masquelier and L. Croguennec, *J. Phys. Chem, C*, 2016, **120**, 26187–26198.
131 M. Ling, Z. Lv, F. Li, J. Zhao, H. Zhang, G. Hou, Q. Zheng and X. Li, *ACS Appl. Mater. Interfaces*, 2020, **12**, 30510–30519.
132 N. Recham, J. N. Chotard, L. Dupont, C. Delacourt, W. Walker, M. Armand and J. M. Tarascon, *Nat. Mater.*, 2010, **9**, 68–74.
133 S. Lee and S. S. Park, *J. Phys. Chem, C*, 2014, **118**, 12642–12648.
134 R. Tripathi, T. N. Ramesh, B. L. Ellis and L. F. Nazar, *Angew. Chem., Int. Ed.*, 2010, **49**, 8738–8742.
135 R. Tripathi, G. R. Gardiner, M. S. Islam and L. F. Nazar, *Chem. Mater.*, 2011, **23**, 2278–2284.
136 N. E. Novikova, N. I. Sorokina, I. A. Verin, O. A. Alekseeva, E. I. Orlova, V. I. Voronkova and M. Tseitlin, *Crystals*, 2018, **8**, 283.
137 S. S. Fedotov, A. S. Samarin and E. V. Antipov, *J. Power Sources*, 2020, **480**, 228840.
138 S. S. Fedotov, A. S. Samarin, V. A. Nikitina, D. A. Aksyonov, S. A. Sokolov, A. Zhugayevych, K. J. Stevenson, N. R. Khasanova, A. M. Abakumov and E. V. Antipov, *J. Mater. Chem. A*, 2018, **6**, 14420–14430.
139 P. R. Kumar, K. Kubota, D. Igarashi and S. Komaba, *J. Phys. Chem, C*, 2021, **125**, 24823–24830.
140 K. L. Harrison and A. Manthiram, *Chem. Mater.*, 2013, **25**, 1751–1760.
141 G. He, A. Huq, W. H. Kan and A. Manthiram, *Chem. Mater.*, 2016, **28**, 1503–1512.
142 K. Chihara, A. Katogi, K. Kubota and S. Komaba, *Chem. Commun.*, 2017, **53**, 5208–5211.
143 J. Ding, Y.-C. Lin, J. Liu, J. Rana, H. Zhang, H. Zhou, I.-H. Chu, K. M. Wiaderek, F. Omenya, N. A. Chernova, K. W. Chapman, L. F. J. Piper, S. P. Ong and M. S. Whittingham, *Adv. Energy Mater.*, 2018, **8**, 1800221.
144 S. S. Fedotov, N. D. Luchinin, D. A. Aksyonov, A. V. Morozov, S. V. Ryazantsev, M. Gaboardi, J. R. Plaisier, K. J. Stevenson, A. M. Abakumov and E. V. Antipov, *Nat. Commun.*, 2020, **11**, 1484.
145 N. Recham, G. Rousse, M. T. Sougrati, J.-N. Chotard, C. Frayret, S. Mariyappan, B. C. Melot, J.-C. Jumas and J.-M. Tarascon, *Chem. Mater.*, 2012, **24**, 4363–4370.
146 J. Kim, H. Kim, I. Park, Y.-U. Park, J.-K. Yoo, K.-Y. Park, S. Lee and K. Kang, *Energy Environ. Sci.*, 2013, **6**, 830–834.
147 W. Huang, J. Zhou, B. Li, L. An, P. Cui, W. Xia, L. Song, D. Xia, W. Chu and Z. Wu, *Small*, 2015, **11**, 2170–2176.
148 P. Barpanda, G. Oyama, S.-i. Nishimura, S.-C. Chung and A. Yamada, *Nat. Commun.*, 2014, **5**, 4358.
149 W. Pan, W. Guan, S. Liu, B. B. Xu, C. Liang, H. Pan, M. Yan and Y. Jiang, *J. Mater. Chem. A*, 2019, **7**, 13197–13204.
150 P. R. Kumar, Y. H. Jung, C. H. Lim and D. K. Kim, *J. Mater. Chem. A*, 2015, **3**, 6271–6275.
151 P. R. Kumar, Y. H. Jung, J. E. Wang and D. K. Kim, *J. Power Sources*, 2016, **324**, 421–427.
152 M. Bianchini, F. Fauth, N. Brisset, F. Weill, E. Suard, C. Masquelier and L. Croguennec, *Chem. Mater.*, 2015, **27**, 3009–3020.
153 M. Bianchini, N. Brisset, F. Fauth, F. Weill, E. Elkaim, E. Suard, C. Masquelier and L. Croguennec, *Chem. Mater.*, 2014, **26**, 4238–4247.
154 P. R. Kumar, K. Kubota, Y. Miura, M. Ohara, K. Gotoh and S. Komaba, *J. Power Sources*, 2021, **493**, 229676.
155 S.-i. Nishimura, M. Nakamura, R. Natsui and A. Yamada, *J. Am. Chem. Soc.*, 2010, **132**, 13596–13597.
156 T. Ye, P. Barpanda, S.-i. Nishimura, N. Furuta, S.-C. Chung and A. Yamada, *Chem. Mater.*, 2013, **25**, 3623–3629.
157 P. Barpanda, T. Ye, S.-i. Nishimura, S.-C. Chung, Y. Yamada, M. Okubo, H. Zhou and A. Yamada, *Electrochem. Commun.*, 2012, **24**, 116–119.
158 P. Barpanda, G. Liu, C. D. Ling, M. Tamaru, M. Avdeev, S.-C. Chung, Y. Yamada and A. Yamada, *Chem. Mater.*, 2013, **25**, 3480–3487.
159 R. Gond, S. Singh, S. P. Vanam, V. Pralong and P. Barpanda, *In Situ X-Ray Diffraction and Alkali Ion (A = Li, Na, K) Intercalation Behavior of Na2FeP2O7 Pyrophosphate*, Singapore, 2021.
160 Y. Niu, Y. Zhang and M. Xu, *J. Mater. Chem. A*, 2019, **7**, 15006–15025.
161 H. Kim, C. S. Park, J. W. Choi and Y. Jung, *Angew. Chem., Int. Ed.*, 2016, **55**, 6662–6666.
162 P. Barpanda, M. Avdeev, C. D. Ling, J. Lu and A. Yamada, *Inorg. Chem.*, 2013, **52**, 395–401.
163 H. Kim, I. Park, D.-H. Seo, S. Lee, S.-W. Kim, W. J. Kwon, Y.-U. Park, C. S. Kim, S. Jeon and K. Kang, *J. Am. Chem. Soc.*, 2012, **134**, 10369–10372.
164 H. Kim, I. Park, S. Lee, H. Kim, K.-Y. Park, Y.-U. Park, H. Kim, J. Kim, H.-D. Lim and W.-S. Yoon, *Chem. Mater.*, 2013, **25**, 3614–3622.
165 B. Senthilkumar, C. Murugesan, K. Sada and P. Barpanda, *J. Power Sources*, 2020, **480**, 228794.
166 M. Zarrabeitia, M. Jauregui, N. Sharma, J. C. Pramudita and M. Casas-Cabanas, *Chem. Mater.*, 2019, **31**, 5152–5159.

167 H. Zhang, I. Hasa, D. Buchholz, B. Qin, D. Geiger, S. Jeong, U. Kaiser and S. Passerini, *NPG Asia Mater.*, 2017, **9**, e370.
168 P. R. Kumar, H. B. Yahia, I. Belharouak, M. T. Sougrati, S. Passerini, R. Amin and R. Essehli, *J. Solid State Electrochem.*, 2020, **24**, 17–24.
169 P. R. Kumar, R. Essehli, H. B. Yahia, R. Amin and I. Belharouak, *RSC Adv.*, 2020, **10**, 15983–15989.
170 W. B. Park, S. C. Han, C. Park, S. U. Hong, U. Han, S. P. Singh, Y. H. Jung, D. Ahn, K.-S. Sohn and M. Pyo, *Adv. Energy Mater.*, 2018, **8**, 1703099.
171 N. Imanishi, T. Morikawa, J. Kondo, R. Yamane, Y. Takeda, O. Yamamoto, H. Sakaebe and M. Tabuchi, *J. Power Sources*, 1999, **81–82**, 530–534.
172 Y. Lu, L. Wang, J. Cheng and J. B. Goodenough, *Chem. Commun.*, 2012, **48**, 6544.
173 A. Eftekhari, *J. Power Sources*, 2004, **126**, 221–228.
174 L. Xue, Y. Li, H. Gao, W. Zhou, X. Lü, W. Kaveevivitchai, A. Manthiram and J. B. Goodenough, *J. Am. Chem. Soc.*, 2017, **139**, 2164–2167.
175 X. Bie, K. Kubota, T. Hosaka, K. Chihara and S. Komaba, *J. Mater. Chem. A*, 2017, **5**, 4325–4330.
176 P. Xiao, J. Song, L. Wang, J. B. Goodenough and G. Henkelman, *Chem. Mater.*, 2015, **27**, 3763–3768.
177 L. Wang, J. Song, R. Qiao, L. A. Wray, M. A. Hossain, Y. D. Chuang, W. Yang, Y. Lu, D. Evans, J. J. Lee, S. Vail, X. Zhao, M. Nishijima, S. Kakimoto and J. B. Goodenough, *J. Am. Chem. Soc.*, 2015, **137**, 2548–2554.
178 J. Song, L. Wang, Y. Lu, J. Liu, B. Guo, P. Xiao, J.-J. Lee, X.-Q. Yang, G. Henkelman and J. B. Goodenough, *J. Am. Chem. Soc.*, 2015, **137**, 2658–2664.
179 J. Liao, Q. Hu, Y. Yu, H. Wang, Z. Tang, Z. Wen and C. Chen, *J. Mater. Chem. A*, 2017, **5**, 19017–19024.
180 P. A. Morozova, I. A. Trussov, D. P. Rupasov, V. A. Nikitina, A. M. Abakumov and S. S. Fedotov, *Crystals*, 2021, **11**, 895.
181 Y. Lu, L. Wang, J. Cheng and J. B. Goodenough, *Chem. Commun.*, 2012, **48**, 6544–6546.
182 L. Wang, Y. Lu, J. Liu, M. Xu, J. Cheng, D. Zhang and J. B. Goodenough, *Angew. Chem.*, 2013, **52**, 1964–1967.
183 Y. You, X.-L. Wu, Y.-X. Yin and Y.-G. Guo, *Energy Environ. Sci.*, 2014, **7**, 1643.
184 J. Wu, J. Song, K. Dai, Z. Zhuo, L. A. Wray, G. Liu, Z.-x. Shen, R. Zeng, Y. Lu and W. Yang, *J. Am. Chem. Soc.*, 2017, **139**, 18358–18364.
185 Y. You, X. Yu, Y. Yin, K.-W. Nam and Y.-G. Guo, *Nano Res.*, 2014, **8**, 117–128.
186 L. Deng, J. Qu, X. Niu, J. Liu, J. Zhang, Y. Hong, M. Feng, J. Wang, M. Hu and L. Zeng, *Nat. Commun.*, 2021, **12**, 1–9.
187 M. Ishizaki, H. Ando, N. Yamada, K. Tsumoto, K. Ono, H. Sutoh, T. Nakamura, Y. Nakao and M. Kurihara, *J. Mater. Chem. A*, 2019, **7**, 4777–4787.
188 T. Hosaka, T. Fukabori, H. Kojima, K. Kubota and S. Komaba, *ChemSusChem*, 2021, **14**, 1166–1175.
189 K. Kubota, S. Shimadzu, N. Yabuuchi, S. Tominaka, S. Shiraishi, M. Abreu-Sepulveda, A. Manivannan, K. Gotoh, M. Fukunishi and M. Dahbi, *Chem. Mater.*, 2020, **32**, 2961–2977.
190 M. Dahbi, N. Yabuuchi, K. Kubota, K. Tokiwa and S. Komaba, *Phys. Chem. Chem. Phys.*, 2014, **16**, 15007–15028.
191 G. Wang, M. Yu and X. Feng, *Chem. Soc. Rev.*, 2021, **50**, 2388–2443.
192 J. Zhang, L. Lai, H. Wang, M. Chen and Z. X. Shen, *Mater. Today Energy*, 2021, 100747.
193 L. Zhang, W. Wang, S. Lu and Y. Xiang, *Adv. Energy Mater.*, 2021, **11**, 2003640.
194 D. Cheng, X. Zhou, H. Hu, Z. Li, J. Chen, L. Miao, X. Ye and H. Zhang, *Carbon*, 2021, **182**, 758–769.
195 D. Larcher and J.-M. Tarascon, *Nat. Chem.*, 2015, **7**, 19–29.
196 G. Haxel, *Rare earth elements: critical resources for high technology*, US Department of the Interior, US Geological Survey, 2002.
197 R. Marom, S. F. Amalraj, N. Leifer, D. Jacob and D. Aurbach, *J. Mater. Chem.*, 2011, **21**, 9938–9954.
198 J. D. Bernal, *Proc. R. Soc. London, Ser. A*, 1924, **106**, 749–773.
199 P. Trucano and R. Chen, *Nature*, 1975, **258**, 136–137.
200 A. Yacoby, *Nat. Phys.*, 2011, **7**, 925–926.
201 MOTIG, Manufacture of hard carbon, *US Pat.*, US338542A, 1886, USA, Utility patent.
202 R. E. Franklin, *Proc. R. Soc. London, Ser. A*, 1951, **209**, 196–218.
203 Z. Jian, W. Luo and X. Ji, *J. Am. Chem. Soc.*, 2015, **137**, 11566–11569.
204 S. Dhir, S. Wheeler, I. Capone and M. Pasta, *Chem*, 2020, **6**, 2442–2460.
205 H. Onuma, K. Kubota, S. Muratsubaki, W. Ota, M. Shishkin, H. Sato, K. Yamashita, S. Yasuno and S. Komaba, *J. Mater. Chem. A*, 2021, **9**, 11187–11200.
206 J. C. Pramudita, V. K. Peterson, J. A. Kimpton and N. Sharma, *Powder Diffr.*, 2017, **32**, S43–S48.
207 L. Fan, R. Ma, Q. Zhang, X. Jia and B. Lu, *Angew. Chem.*, 2019, **131**, 10610–10615.
208 T. Ohzuku, Y. Iwakoshi and K. Sawai, *J. Electrochem. Soc.*, 1993, **140**, 2490.
209 Y. Li, Y. Lu, P. Adelhelm, M.-M. Titirici and Y.-S. Hu, *Chem. Soc. Rev.*, 2019, **48**, 4655–4687.
210 M. S. Dresselhaus and G. Dresselhaus, *Adv. Phys.*, 1981, **30**, 139–326.
211 H. Moriwake, A. Kuwabara, C. A. J. Fisher and Y. Ikuhara, *RSC Adv.*, 2017, **7**, 36550–36554.
212 Y. Liu, B. V. Merinov and W. A. Goddard, *Proc. Natl. Acad. Sci. U.S.A.*, 2016, **113**, 3735–3739.
213 O. Lenchuk, P. Adelhelm and D. Mollenhauer, *Phys. Chem. Chem. Phys.*, 2019, **21**, 19378–19390.
214 K. Nobuhara, H. Nakayama, M. Nose, S. Nakanishi and H. Iba, *J. Power Sources*, 2013, **243**, 585–587.
215 Y. Okamoto, *J. Phys. Chem. C*, 2014, **118**, 16–19.
216 F. Zou and A. Manthiram, *Adv. Energy Mater.*, 2020, **10**, 2002508.
217 W. Zhang, M. Dahbi and S. Komaba, *Curr. Opin. Chem. Eng.*, 2016, **13**, 36–44.
218 P.-F. Cao, G. Yang, B. Li, Y. Zhang, S. Zhao, S. Zhang, A. Erwin, Z. Zhang, A. P. Sokolov and J. Nanda, *ACS Energy Lett.*, 2019, **4**, 1171–1180.

219 S. Komaba, N. Yabuuchi, T. Ozeki, K. Okushi, H. Yui, K. Konno, Y. Katayama and T. Miura, *J. Power Sources*, 2010, **195**, 6069–6074.
220 S. Komaba, N. Yabuuchi, T. Ozeki, Z.-J. Han, K. Shimomura, H. Yui, Y. Katayama and T. Miura, *J. Phys. Chem. C*, 2012, **116**, 1380–1389.
221 N. Yabuuchi, Y. Matsuura, T. Ishikawa, S. Kuze, J.-Y. Son, Y.-T. Cui, H. Oji and S. Komaba, *ChemElectroChem*, 2014, **1**, 580–589.
222 K. Ui, D. Fujii, Y. Niwata, T. Karouji, Y. Shibata, Y. Kadoma, K. Shimada and N. Kumagai, *J. Power Sources*, 2014, **247**, 981–990.
223 T. Zhang, I. de Meatza, X. Qi and E. Paillard, *J. Power Sources*, 2017, **356**, 97–102.
224 S. Komaba, T. Ozeki and K. Okushi, *J. Power Sources*, 2009, **189**, 197–203.
225 S. Komaba, K. Okushi, T. Ozeki, H. Yui, Y. Katayama, T. Miura, T. Saito and H. Groult, *Electrochem. Solid-State Lett.*, 2009, **12**, A107.
226 D. Bresser, D. Buchholz, A. Moretti, A. Varzi and S. Passerini, *Energy Environ. Sci.*, 2018, **11**, 3096–3127.
227 V. A. Nguyen and C. Kuss, *J. Electrochem. Soc.*, 2020, **167**, 065501.
228 Y. Ma, J. Ma and G. Cui, *Energy Storage Materials*, 2019, **20**, 146–175.
229 B. Jache and P. Adelhelm, *Angew. Chem.*, 2014, **126**, 10333–10337.
230 H. Kim, J. Hong, G. Yoon, H. Kim, K.-Y. Park, M.-S. Park, W.-S. Yoon and K. Kang, *Energy Environ. Sci.*, 2015, **8**, 2963–2969.
231 M. Goktas, C. Bolli, E. J. Berg, P. Novak, K. Pollok, F. Langenhorst, M. V. Roeder, O. Lenchuk, D. Mollenhauer and P. Adelhelm, *Adv. Energy Mater.*, 2018, **8**, 1702724.
232 H. Kim, J. Hong, Y. U. Park, J. Kim, I. Hwang and K. Kang, *Adv. Funct. Mater.*, 2015, **25**, 534–541.
233 Z.-L. Xu, G. Yoon, K.-Y. Park, H. Park, O. Tamwattana, S. J. Kim, W. M. Seong and K. Kang, *Nat. Commun.*, 2019, **10**, 1–10.
234 G. Yoon, H. Kim, I. Park and K. Kang, *Adv. Energy Mater.*, 2017, **7**, 1601519.
235 I. Escher, Y. Kravets, G. A. Ferrero, M. Goktas and P. Adelhelm, *Energy Technol.*, 2021, **9**, 2000880.
236 Y. J. Kim, S. Pyo, S. Kim and W.-H. Ryu, *Carbon*, 2021, **175**, 585–593.
237 H. Kim, G. Yoon, K. Lim and K. Kang, *Chem. Commun.*, 2016, **52**, 12618–12621.
238 L. Li, L. Liu, Z. Hu, Y. Lu, Q. Liu, S. Jin, Q. Zhang, S. Zhao and S. L. Chou, *Angew. Chem.*, 2020, **132**, 13017–13024.
239 A. P. Cohn, N. Muralidharan, R. Carter, K. Share, L. Oakes and C. L. Pint, *J. Mater. Chem. A*, 2016, **4**, 14954–14959.
240 S. C. Jung, Y.-J. Kang and Y.-K. Han, *Nano Energy*, 2017, **34**, 456–462.
241 X. Dou, I. Hasa, D. Saurel, C. Vaalma, L. Wu, D. Buchholz, D. Bresser, S. Komaba and S. Passerini, *Mater. Today*, 2019, **23**, 87–104.
242 D. Saurel, B. Orayech, B. Xiao, D. Carriazo, X. Li and T. Rojo, *Adv. Energy Mater.*, 2018, **8**, 1703268.
243 Y. Nishi, *Chem. Rec.*, 2001, **1**, 406–413.
244 X. Dou, I. Hasa, M. Hekmatfar, T. Diemant, R. J. Behm, D. Buchholz and S. Passerini, *ChemSusChem*, 2017, **10**, 2668–2676.
245 E. M. Lotfabad, J. Ding, K. Cui, A. Kohandehghan, W. P. Kalisvaart, M. Hazelton and D. Mitlin, *ACS Nano*, 2014, **8**, 7115–7129.
246 H. Hou, X. Qiu, W. Wei, Y. Zhang and X. Ji, *Adv. Energy Mater.*, 2017, **7**, 1602898.
247 D. A. Stevens and J. R. Dahn, *J. Electrochem. Soc.*, 2000, **147**, 1271.
248 S. Komaba, W. Murata, T. Ishikawa, N. Yabuuchi, T. Ozeki, T. Nakayama, A. Ogata, K. Gotoh and K. Fujiwara, *Adv. Funct. Mater.*, 2011, **21**, 3859–3867.
249 P. Bai, Y. He, X. Zou, X. Zhao, P. Xiong and Y. Xu, *Adv. Energy Mater.*, 2018, **8**, 1703217.
250 S. Qiu, L. Xiao, M. L. Sushko, K. S. Han, Y. Shao, M. Yan, X. Liang, L. Mai, J. Feng and Y. Cao, *Adv. Energy Mater.*, 2017, **7**, 1700403.
251 C. Chen, Z. Wang, B. Zhang, L. Miao, J. Cai, L. Peng, Y. Huang, J. Jiang, Y. Huang and L. Zhang, *Energy Storage Materials*, 2017, **8**, 161–168.
252 J. M. Stratford, P. K. Allan, O. Pecher, P. A. Chater and C. P. Grey, *Chem. Commun.*, 2016, **52**, 12430–12433.
253 Y. Youn, B. Gao, A. Kamiyama, K. Kubota, S. Komaba and Y. Tateyama, *npj Comput. Mater.*, 2021, **7**, 1–8.
254 J. M. Stratford, A. K. Kleppe, D. S. Keeble, P. A. Chater, S. S. Meysami, C. J. Wright, J. Barker, M.-M. Titirici, P. K. Allan and C. P. Grey, *J. Am. Chem. Soc.*, 2021, **143**, 14274–14286.
255 Y. Morikawa, S. i. Nishimura, R. i. Hashimoto, M. Ohnuma and A. Yamada, *Adv. Energy Mater.*, 2020, **10**, 1903176.
256 A. Kamiyama, K. Kubota and S. Komaba, presented in part at *The 46th Annual Meeting of the Carbon Society of Japan*, 2019.
257 B. Zhang, C. M. Ghimbeu, C. Laberty, C. Vix-Guterl and J. m. Tarascon, *Adv. Energy Mater.*, 2016, **6**, 1501588.
258 J. J. Kipling, J. N. Sherwood, P. V. Shooter and N. R. Thompson, *Carbon*, 1964, **1**, 315–320.
259 Y. Li, M. P. Paranthaman, K. Akato, A. K. Naskar, A. M. Levine, R. J. Lee, S.-O. Kim, J. Zhang, S. Dai and A. Manthiram, *J. Power Sources*, 2016, **316**, 232–238.
260 A. M. Navarro-Suarez, D. Saurel, P. Sanchez-Fontecoba, E. Castillo-Martinez, J. Carretero-González and T. Rojo, *J. Power Sources*, 2018, **397**, 296–306.
261 H. Yamamoto, S. Muratsubaki, K. Kubota, M. Fukunishi, H. Watanabe, J. Kim and S. Komaba, *J. Mater. Chem. A*, 2018, **6**, 16844–16848.
262 Z. Li, C. Bommier, Z. S. Chong, Z. Jian, T. W. Surta, X. Wang, Z. Xing, J. C. Neuefeind, W. F. Stickle and M. Dolgos, *Adv. Energy Mater.*, 2017, **7**, 1602894.
263 P. J. F. Harris, *Crit. Rev. Solid State Mater. Sci.*, 2005, **30**, 235–253.

264 A. Kamiyama, K. Kubota, D. Igarashi, Y. Youn, Y. Tateyama, H. Ando, K. Gotoh and S. Komaba, *Angew. Chem., Int. Ed.*, 2021, **60**, 5114–5120.
265 T. Morishita, T. Tsumura, M. Toyoda, J. Przepiórski, A. W. Morawski, H. Konno and M. Inagaki, *Carbon*, 2010, **48**, 2690–2707.
266 T. Kyotani, Z. Ma and A. Tomita, *Carbon*, 2003, **41**, 1451–1459.
267 R. Ryoo, S. H. Joo and S. Jun, *J. Phys. Chem. B*, 1999, **103**, 7743–7746.
268 Q. Meng, Y. Lu, F. Ding, Q. Zhang, L. Chen and Y.-S. Hu, *ACS Energy Lett.*, 2019, **4**, 2608–2612.
269 Y. Qi, Y. Lu, F. Ding, Q. Zhang, H. Li, X. Huang, L. Chen and Y. S. Hu, *Angew. Chem., Int. Ed.*, 2019, **58**, 4361–4365.
270 B. Cao, H. Liu, B. Xu, Y. Lei, X. Chen and H. Song, *J. Mater. Chem. A*, 2016, **4**, 6472–6478.
271 Y. Xu, C. Zhang, M. Zhou, Q. Fu, C. Zhao, M. Wu and Y. Lei, *Nat. Commun.*, 2018, **9**, 1–11.
272 Z. Jian, C. Bommier, L. Luo, Z. Li, W. Wang, C. Wang, P. A. Greaney and X. Ji, *Chem. Mater.*, 2017, **29**, 2314–2320.
273 D. Ni, W. Sun, Z. Wang, Y. Bai, H. Lei, X. Lai and K. Sun, *Adv. Energy Mater.*, 2019, **9**, 1900036.
274 J. R. Dahn, T. Zheng, Y. Liu and J. Xue, *Science*, 1995, **270**, 590–593.
275 W. Luo, Z. Jian, Z. Xing, W. Wang, C. Bommier, M. M. Lerner and X. Ji, *ACS Cent. Sci.*, 2015, **1**, 516–522.
276 J. Ni and Y. Li, *Adv. Energy Mater.*, 2016, **6**, 1600278.
277 E. Yoo, J. Kim, E. Hosono, H.-s. Zhou, T. Kudo and I. Honma, *Nano Lett.*, 2008, **8**, 2277–2282.
278 S. Gong and Q. Wang, *J. Phys. Chem. C*, 2017, **121**, 24418–24424.
279 C. Ling and F. Mizuno, *Phys. Chem. Chem. Phys.*, 2014, **16**, 10419–10424.
280 X. Zuo, J. Zhu, P. Müller-Buschbaum and Y.-J. Cheng, *Nano Energy*, 2017, **31**, 113–143.
281 H. Okamoto, *J. Phase Equilib. Diffus.*, 2009, **30**, 118–119.
282 M. R. Zamfir, H. T. Nguyen, E. Moyen, Y. H. Lee and D. Pribat, *J. Mater. Chem. A*, 2013, **1**, 9566.
283 W.-J. Zhang, *J. Power Sources*, 2011, **196**, 13–24.
284 M. Lao, Y. Zhang, W. Luo, Q. Yan, W. Sun and S. X. Dou, *Adv. Mater.*, 2017, **29**, 1700622.
285 I. Sultana, M. M. Rahman, Y. Chen and A. M. Glushenkov, *Adv. Funct. Mater.*, 2018, **28**, 1703857.
286 K. Yang, X. Zhang, K. Song, J. Zhang, C. Liu, L. Mi, Y. Wang and W. Chen, *Electrochim. Acta*, 2020, **337**, 135783.
287 J. Zhang, K. Song, L. Mi, C. Liu, X. Feng, J. Zhang, W. Chen and C. Shen, *J. Phys. Chem. Lett.*, 2020, **11**, 1435–1442.
288 S. Zhou, J. Lan, K. Song, Z. Zhang, J. Shi and W. Chen, *FlatChem*, 2021, **28**, 100259.
289 K. Song, J. Liu, H. Dai, Y. Zhao, S. Sun, J. Zhang, C. Qin, P. Yan, F. Guo and C. Wang, *Chem*, 2021, **7**, 2684–2694.
290 C.-M. Park, J.-H. Kim, H. Kim and H.-J. Sohn, *Chem. Soc. Rev.*, 2010, **39**, 3115.
291 N. Yabuuchi, K. Kubota, M. Dahbi and S. Komaba, *Chem. Rev.*, 2014, **114**, 11636–11682.
292 S. Komaba, Y. Matsuura, T. Ishikawa, N. Yabuuchi, W. Murata and S. Kuze, *Electrochem. Commun.*, 2012, **21**, 65–68.
293 M. Dahbi, N. Yabuuchi, K. Kubota, K. Tokiwa and S. Komaba, *Phys. Chem. Chem. Phys.*, 2014, **16**, 15007–15028.
294 K. Kubota and S. Komaba, *J. Electrochem. Soc.*, 2015, **162**, A2538–A2550.
295 I. Abe, T. Horiba, Y. Abe, K. Hida, T. Matsuyama, S. Yasuno and S. Komaba, *J. Electrochem. Soc.*, 2020, **167**, 110513.
296 M. Dahbi, N. Yabuuchi, M. Fukunishi, K. Kubota, K. Chihara, K. Tokiwa, X.-F. Yu, H. Ushiyama, K. Yamashita, J.-Y. Son, Y.-T. Cui, H. Oji and S. Komaba, *Chem. Mater.*, 2016, **28**, 1625–1635.
297 M. Obrovac, L. Christensen, D. B. Le and J. R. Dahn, *J. Electrochem. Soc.*, 2007, **154**, A849.
298 T. T. Tran and M. N. Obrovac, *J. Electrochem. Soc.*, 2011, **158**, A1411.
299 Y. Lee, H. Lim, S.-O. Kim, H.-S. Kim, K. J. Kim, K.-Y. Lee and W. Choi, *J. Mater. Chem. A*, 2018, **6**, 20383–20392.
300 I. Sultana, T. Ramireddy, M. M. Rahman, Y. Chen and A. M. Glushenkov, *Chem. Commun.*, 2016, **52**, 9279–9282.
301 I. Sultana, M. M. Rahman, T. Ramireddy, Y. Chen and A. M. Glushenkov, *J. Mater. Chem. A*, 2017, **5**, 23506–23512.
302 J. Ruan, F. Mo, Z. Long, Y. Song, F. Fang, D. Sun and S. Zheng, *ACS Nano*, 2020, **14**, 12222–12233.
303 T. T. Tran and M. Obrovac, *J. Electrochem. Soc.*, 2011, **158**, A1411.
304 L. Zhou, Z. Cao, W. Wahyudi, J. Zhang, J.-Y. Hwang, Y. Cheng, L. Wang, L. Cavallo, T. Anthopoulos, Y.-K. Sun, H. N. Alshareef and J. Ming, *ACS Energy Lett.*, 2020, **5**, 766–776.
305 A. K. Chan, R. Tatara, S. Feng, P. Karayaylali, J. Lopez, I. E. L. Stephens and Y. Shao-Horn, *J. Electrochem. Soc.*, 2019, **166**, A1867–A1874.
306 S. Sim, P. Oh, S. Park and J. Cho, *Adv. Mater.*, 2013, **25**, 4498–4503.
307 X.-Y. Zhou, J.-J. Tang, J. Yang, J. Xie and L.-L. Ma, *Electrochim. Acta*, 2013, **87**, 663–668.
308 Y. S. Jung, K. T. Lee and S. M. Oh, *Electrochim. Acta*, 2007, **52**, 7061–7067.
309 M. Saito, K. Nakai, T. Yamada, T. Takenaka, M. Hirota, A. Kamei, A. Tasaka and M. Inaba, *J. Power Sources*, 2011, **196**, 6637–6643.
310 I. Kovalenko, B. Zdyrko, A. Magasinski, B. Hertzberg, Z. Milicev, R. Burtovyy, I. Luzinov and G. Yushin, *Science*, 2011, **334**, 75–79.
311 J. Song, M. Zhou, R. Yi, T. Xu, M. L. Gordin, D. Tang, Z. Yu, M. Regula and D. Wang, *Adv. Funct. Mater.*, 2014, **24**, 5904–5910.
312 B. Koo, H. Kim, Y. Cho, K. T. Lee, N.-S. Choi and J. Cho, *Angew. Chem.*, 2012, **124**, 8892–8897.
313 M.-H. Ryou, J. Kim, I. Lee, S. Kim, Y. K. Jeong, S. Hong, J. H. Ryu, T.-S. Kim, J.-K. Park, H. Lee and J. W. Choi, *Adv. Mater.*, 2013, **25**, 1571–1576.

314 N. S. Hochgatterer, M. R. Schweiger, S. Koller, P. R. Raimann, T. WöHrle, C. Wurm and M. Winter, *Electrochem. Solid-State Lett.*, 2008, **11**, A76.
315 T. Mochizuki, S. Aoki, T. Horiba, M. Schulz-Dobrick, Z.-J. Han, S. Fukuyama, H. Oji, S. Yasuno and S. Komaba, *ACS Sustainable Chem. Eng.*, 2017, **5**, 6343–6355.
316 H. Li, *Electrochem. Solid-State Lett.*, 1999, **2**, 547.
317 W.-R. Liu, Z.-Z. Guo, W.-S. Young, D.-T. Shieh, H.-C. Wu, M.-H. Yang and N.-L. Wu, *J. Power Sources*, 2005, **140**, 139–144.
318 J. R. Szczech and S. Jin, *Energy Environ. Sci.*, 2011, **4**, 56–72.
319 M. Murase, N. Yabuuchi, Z.-J. Han, J.-Y. Son, Y.-T. Cui, H. Oji and S. Komaba, *ChemSusChem*, 2012, **5**, 2307–2311.
320 S. Komaba, N. Yabuuchi, T. Ozeki, Z.-J. Han, K. Shimomura, H. Yui, Y. Katayama and T. Miura, *J. Phys. Chem. C*, 2012, **116**, 1380–1389.
321 M. Fukunishi, N. Yabuuchi, M. Dahbi, J.-Y. Son, Y. Cui, H. Oji and S. Komaba, *J. Phys. Chem. C*, 2016, **120**, 15017–15026.
322 P. Parikh, M. Sina, A. Banerjee, X. Wang, M. S. D'Souza, J.-M. Doux, E. A. Wu, O. Y. Trieu, Y. Gong, Q. Zhou, K. Snyder and Y. S. Meng, *Chem. Mater.*, 2019, **31**, 2535–2544.
323 A. Miranda, K. Sarang, B. Gendensuren, E.-S. Oh, J. Lutkenhaus and R. Verduzco, *Mol. Syst. Des. Eng.*, 2020, **5**, 709–724.
324 T. R. Martin, R. T. Pekarek, J. E. Coyle, M. C. Schulze and N. R. Neale, *J. Mater. Chem. A*, 2021, **9**, 21929–21938.
325 L. Chen, K. Wang, X. Xie and J. Xie, *J. Power Sources*, 2007, **174**, 538–543.
326 C. Xu, F. Lindgren, B. Philippe, M. Gorgoi, F. Björefors, K. Edström and T. Gustafsson, *Chem. Mater.*, 2015, **27**, 2591–2599.
327 S. Dalavi, P. Guduru and B. L. Lucht, *J. Electrochem. Soc.*, 2012, **159**, A642–A646.
328 V. Etacheri, O. Haik, Y. Goffer, G. A. Roberts, I. C. Stefan, R. Fasching and D. Aurbach, *Langmuir*, 2012, **28**, 965–976.
329 Y. Jin, N.-J. H. Kneusels, P. C. M. M. Magusin, G. Kim, E. Castillo-Martínez, L. E. Marbella, R. N. Kerber, D. J. Howe, S. Paul, T. Liu and C. P. Grey, *J. Am. Chem. Soc.*, 2017, **139**, 14992–15004.
330 R. Scipioni, D. Isheim and S. A. Barnett, *Appl. Mater. Today*, 2020, **20**, 100748.
331 W. Li, A. Dolocan, P. Oh, H. Celio, S. Park, J. Cho and A. Manthiram, *Nat. Commun.*, 2017, **8**, 1–10.
332 E. Peled and S. Menkin, *J. Electrochem. Soc.*, 2017, **164**, A1703.
333 P. Verma, P. Maire and P. Novák, *Electrochim. Acta*, 2010, **55**, 6332–6341.
334 E. Peled, *J. Electrochem. Soc.*, 1979, **126**, 2047.
335 E. Markevich, G. Salitra and D. Aurbach, *ACS Energy Lett.*, 2017, **2**, 1337–1345.
336 H. Kim, K. Lim, G. Yoon, J. H. Park, K. Ku, H. D. Lim, Y. E. Sung and K. Kang, *Adv. Energy Mater.*, 2017, **7**, 1700418.
337 J. Song, B. Xiao, Y. Lin, K. Xu and X. Li, *Adv. Energy Mater.*, 2018, **8**, 1703082.
338 H. Wang, D. Zhai and F. Kang, *Energy Environ. Sci.*, 2020, **13**, 4583–4608.
339 H. Bülter, F. Peters, J. Schwenzel and G. Wittstock, *Angew. Chem., Int. Ed.*, 2014, **53**, 10531–10535.
340 T. Hosaka, T. Matsuyama, K. Kubota, S. Yasuno and S. Komaba, *ACS Appl. Mater. Interfaces*, 2020, **12**, 34873–34881.
341 Y. Lei, D. Han, J. Dong, L. Qin, X. Li, D. Zhai, B. Li, Y. Wu and F. Kang, *Energy Storage Materials*, 2020, **24**, 319–328.
342 A. M. Tripathi, W.-N. Su and B. J. Hwang, *Chem. Soc. Rev.*, 2018, **47**, 736–851.
343 J. Hui, Z. T. Gossage, D. Sarbapalli, K. Hernandez-Burgos and J. Rodríguez-López, *Anal. Chem.*, 2018, **91**, 60–83.
344 J. Z. Olson, P. K. Johansson, D. G. Castner and C. W. Schlenker, *Chem. Mater.*, 2018, **30**, 1239–1248.
345 F. Shi, P. N. Ross, G. A. Somorjai and K. Komvopoulos, *J. Phys. Chem. C*, 2017, **121**, 14476–14483.
346 A. v. Cresce, S. M. Russell, D. R. Baker, K. J. Gaskell and K. Xu, *Nano Lett.*, 2014, **14**, 1405–1412.
347 M. Steinhauer, M. Stich, M. Kurniawan, B.-K. Seidlhofer, M. Trapp, A. Bund, N. Wagner and K. A. Friedrich, *ACS Appl. Mater. Interfaces*, 2017, **9**, 35794–35801.
348 J. L. L. Lopez and P. J. Grandinetti, *J. Mater. Chem. A*, 2018, **6**, 231–243.
349 Z. T. Gossage, J. Hui, Y. Zeng, H. Flores-Zuleta and J. Rodríguez-López, *Chem. Sci.*, 2019, **10**, 10749–10754.
350 Z. J. Barton, J. Hui, N. B. Schorr and J. Rodríguez-López, *Electrochim. Acta*, 2017, **241**, 98–105.
351 D. Aurbach, B. Markovsky, I. Weissman, E. Levi and Y. Ein-Eli, *Electrochim. Acta*, 1999, **45**, 67–86.
352 G. G. Eshetu, S. Grugeon, H. Kim, S. Jeong, L. Wu, G. Gachot, S. Laruelle, M. Armand and S. Passerini, *ChemSusChem*, 2016, **9**, 462–471.
353 S. J. An, J. Li, C. Daniel, D. Mohanty, S. Nagpure and D. L. Wood III, *Carbon*, 2016, **105**, 52–76.
354 L. Suo, O. Borodin, T. Gao, M. Olguin, J. Ho, X. Fan, C. Luo, C. Wang and K. Xu, *Science*, 2015, **350**, 938–943.
355 B. Ravikumar, M. Mynam and B. Rai, *J. Phys. Chem. C*, 2018, **122**, 8173–8181.
356 X. Chen, H. R. Li, X. Shen and Q. Zhang, *Angew. Chem., Int. Ed.*, 2018, **57**, 16643–16647.
357 K. Yoshida, M. Nakamura, Y. Kazue, N. Tachikawa, S. Tsuzuki, S. Seki, K. Dokko and M. Watanabe, *J. Am. Chem. Soc.*, 2011, **133**, 13121–13129.
358 J. Wang, Y. Yamada, K. Sodeyama, E. Watanabe, K. Takada, Y. Tateyama and A. Yamada, *Nat. Energy*, 2018, **3**, 22–29.
359 K. Takada, Y. Yamada, E. Watanabe, J. Wang, K. Sodeyama, Y. Tateyama, K. Hirata, T. Kawase and A. Yamada, *ACS Appl. Mater. Interfaces*, 2017, **9**, 33802–33809.
360 X. Bie, K. Kubota, T. Hosaka, K. Chihara and S. Komaba, *J. Mater. Chem. A*, 2017, **5**, 4325–4330.
361 J. Patra, H.-T. Huang, W. Xue, C. Wang, A. S. Helal, J. Li and J.-K. Chang, *Energy Storage Materials*, 2019, **16**, 146–154.
362 B. Liu, J.-G. Zhang and W. Xu, *Joule*, 2018, **2**, 833–845.
363 B. Lee, E. Paek, D. Mitlin and S. W. Lee, *Chem. Rev.*, 2019, **119**, 5416–5460.

364 H. Wang, D. Yu, X. Wang, Z. Niu, M. Chen, L. Cheng, W. Zhou and L. Guo, *Angew. Chem.*, 2019, **131**, 16603–16607.
365 H. Zhang, G. G. Eshetu, X. Judez, C. Li, L. M. Rodriguez-Martínez and M. Armand, *Angew. Chem., Int. Ed.*, 2018, **57**, 15002–15027.
366 R. Mogensen, D. Brandell and R. Younesi, *ACS Energy Lett.*, 2016, **1**, 1173–1178.
367 M. Moshkovich, Y. Gofer and D. Aurbach, *J. Electrochem. Soc.*, 2001, **148**, E155.
368 J. Hui, N. B. Schorr, S. Pakhira, Z. Qu, J. L. Mendoza-Cortes and J. Rodríguez-López, *J. Am. Chem. Soc.*, 2018, **140**, 13599–13603.
369 J. Tan, J. Matz, P. Dong, J. Shen and M. Ye, *Adv. Energy Mater.*, 2021, **11**, 2100046.
370 M. Hess, *Electrochim. Acta*, 2017, **244**, 69–76.
371 Y. Zeng, Z. T. Gossage, D. Sarbapalli, J. Hui and J. Rodríguez-López, *ChemElectroChem*, 2022, **9**, e202101445.
372 H. Yildirim, A. Kinaci, M. K. Chan and J. P. Greeley, *ACS Appl. Mater. Interfaces*, 2015, **7**, 18985–18996.
373 R. A. Adams, A. Varma and V. G. Pol, *J. Power Sources*, 2019, **410**, 124–131.
374 M. Li, J. Lu, X. Ji, Y. Li, Y. Shao, Z. Chen, C. Zhong and K. Amine, *Nat. Rev. Mater.*, 2020, **5**, 276–294.
375 A. L. Michan, B. S. Parimalam, M. Leskes, R. N. Kerber, T. Yoon, C. P. Grey and B. L. Lucht, *Chem. Mater.*, 2016, **28**, 8149–8159.
376 S. S. Zhang, *J. Power Sources*, 2006, **162**, 1379–1394.
377 J. Liao, Q. Hu, Y. Yu, H. Wang, Z. Tang, Z. Wen and C. Chen, *J. Mater. Chem. A*, 2017, **5**, 19017–19024.
378 S. U. Yoon, H. Kim, H.-J. Jin and Y. S. Yun, *Appl. Surf. Sci.*, 2021, **547**, 149193.
379 U. Purushotham, N. Takenaka and M. Nagaoka, *RSC Adv.*, 2016, **6**, 65232–65242.
380 T. Hosaka, T. Fukabori, T. Matsuyama, R. Tatara, K. Kubota and S. Komaba, *ACS Energy Lett.*, 2021, **6**, 3643–3649.
381 R. Xu, X.-B. Cheng, C. Yan, X.-Q. Zhang, Y. Xiao, C.-Z. Zhao, J.-Q. Huang and Q. Zhang, *Matter*, 2019, **1**, 317–344.
382 W. Liu, P. Liu and D. Mitlin, *Adv. Energy Mater.*, 2020, **10**, 2002297.
383 Y. Wan, K. Song, W. Chen, C. Qin, X. Zhang, J. Zhang, H. Dai, Z. Hu, P. Yan and C. Liu, *Angew. Chem., Int. Ed.*, 2021, **60**, 11481–11486.
384 X. Wang, L. Fu, R. Zhan, L. Wang, G. Li, M. Wan, X.-L. Wu, Z. W. Seh, L. Wang and Y. Sun, *ACS Appl. Mater. Interfaces*, 2021, **13**, 13354–13361.
385 H. Wang, J. Hu, J. Dong, K. C. Lau, L. Qin, Y. Lei, B. Li, D. Zhai, Y. Wu and F. Kang, *Adv. Energy Mater.*, 2019, **9**, 1902697.
386 N. Xiao, J. Zheng, G. Gourdin, L. Schkeryantz and Y. Wu, *ACS Appl. Mater. Interfaces*, 2019, **11**, 16571–16577.
387 K. Edstroem, T. Gustafsson and J. O. Thomas, *Electrochim. Acta*, 2004, **50**, 397–403.
388 K. Nie, Y. Hong, J. Qiu, Q. Li, X. Yu, H. Li and L. Chen, *Front. Chem.*, 2018, **6**, 616.
389 D. Takamatsu, Y. Koyama, Y. Orikasa, S. Mori, T. Nakatsutsumi, T. Hirano, H. Tanida, H. Arai, Y. Uchimoto and Z. Ogumi, *Angew. Chem., Int. Ed.*, 2012, **51**, 11597–11601.
390 L. Mu, X. Feng, R. Kou, Y. Zhang, H. Guo, C. Tian, C. J. Sun, X. W. Du, D. Nordlund and H. L. Xin, *Adv. Energy Mater.*, 2018, **8**, 1801975.
391 X. Zhang, Y. Yang, X. Qu, Z. Wei, G. Sun, K. Zheng, H. Yu and F. Du, *Adv. Funct. Mater.*, 2019, **29**, 1905679.
392 K. Momma and F. Izumi, *J. Appl. Crystallogr.*, 2011, **44**, 1272–1276.